

**Effects of Co-flow on Jet Diffusion Flames:
Flow Field and Emissions**

by

Milad Zamani

A thesis submitted in partial fulfillment of the requirements for the degree of

Doctor of Philosophy

Department of Mechanical Engineering
University of Alberta

© Milad Zamani, 2023

ABSTRACT

Industrial flaring is a notable global contributor to carbon dioxide emissions and other key pollutants, such as black carbon, oxides of nitrogen, and unburnt hydrocarbons. Introducing a separate assisting fluid near the base of these flames affects their hydrodynamics, thermodynamics, and chemistry, which in turn affects their overall efficiency and emissions. The extent of these three effects can differ depending on the injection geometry, the composition of assisting fluid (inert gases, air, steam, or atomized liquid water), and the quantity of the assisting fluid added. This study comprises three connected experimental investigations to address the effects on efficiency, emissions, and stability of lab-scale co-flow jet diffusion flames in either a co-annular burner or a slot burner.

In Investigation I, a burner was constructed of two concentric tubes allowed for various generic burner geometries, where different fuels (methane or propane) and co-flow assisting fluids (air, steam, or inert gases) flowed through the annular space and the center tube, respectively. The effects of the composition and flow rate of the fuel and assisting fluid, as well as the burner head geometry, were investigated in terms of carbon conversion efficiency (CCE) and emission indices of black carbon and oxides of nitrogen. Adding low flow rates of the assisting fluid co-flow significantly reduced the black carbon emission, which was not related to the CCE collapse with the main flame blow-off occurring at higher flow rates of assisting fluid. Moreover, any changes that resulted in a higher/lower characteristic flame temperature increased/decreased the emission of oxides of nitrogen. These results showed that, irrespective of the fuel or assisting fluid composition (other than the oxygen-enriched case), there was a range of assisting fluid flow rates, where the CCE was approximately 100%, while the emissions of black carbon and nitrogen oxides were highly suppressed.

To focus on the effects of low flow rates of water as the assisting fluid on emissions,

in Investigation II, a burner was constructed of a contoured nozzle with an inner tube at the center. Different fuels (methane, propane, or methane-propane mixture) and co-flow assisting fluids with the same chemical composition (steam or atomized deionized water) flowed through the annular space and the center tube, respectively. The results revealed that water addition suppressed the emission of black carbon and nitrogen oxides more significantly compared to the same mass of steam addition, which is due to the stronger thermal effect of water as the assisting fluid.

In order to explore the hydrodynamic effects of assisting fluid on the stability of the diffusion flames, in Investigation III, a multi-slot burner was designed and tested. This burner allowed for stabilizing normal and inverse diffusion flames, as well as the coexistence of both in various configurations with 2D optical access. To finalize the design dimensions and specifications, numerical simulations and non-reacting flow particle image velocimetry (PIV) tests were performed on single slots to get the exit velocity profile along their short and long side. After constructing the multi-slot burner, the coexistence of the normal and inverse diffusion flames was investigated by performing reacting flow PIV tests and overall emission measurements. The notable finding is that the inner air flow rate must be high enough to lift off the inner flame and enable fuel and air premixing to lower the total BC emissions.

Keywords

Co-flow jet diffusion flame; Assisted flare; Carbon conversion efficiency; Emission index; Flow field; Blow-off.

PREFACE

This thesis is an original intellectual work by Milad Zamani. The research leading to this thesis was part of my collaboration with Prof. Larry Kostiuk and Prof. Jason Olfert, the research supervisors at the University of Alberta. The following chapters of this thesis have been previously published or presented in the course of my Ph.D. program.

Chapter 2 is based on these published papers:

- Zamani, M., Abbasi-Atibeh, E., Mobaseri, S., Ahsan, H., Ahsan, A., Olfert, J. S., and Kostiuk, L. W. (2021). An experimental study on the carbon conversion efficiency and emission indices of air and steam co-flow diffusion jet flames. *Fuel*, 287:119534.
- Miguel, R. B., Talebi-Moghaddam, S., Zamani, M., Turcotte, C., and Daun, K. J. (2021). Assessing flare combustion efficiency using imaging Fourier transform spectroscopy. *Journal of Quantitative Spectroscopy and Radiative Transfer*, 273, 107835.

Chapter 3 is based on this published paper:

- Bello, O. W., Zamani, M., Abbasi-Atibeh, E., Kostiuk, L. W., and Olfert, J. S. (2021). Comparison of emissions from steam-and water-assisted lab-scale flames. *Fuel*, 302, 121107.

Chapter 4 is based on this published and presented poster:

- Zamani, M., Abbasi-Atibeh, E., Olfert, J. S., and Kostiuk, L. W. (July 2022). Design and characterization of a multi-slot burner, 39th *International Symposium on Combustion*, Vancouver, Canada.

Chapter 5 is based on this published paper:

- Zamani, M., Abbasi-Atibeh, E., Olfert, J. S., and Kostiuk, L. W. (2022). Co-flow jet diffusion flames in a multi-slot burner: Flow field and emissions. *Process Safety and Environmental Protection*, 167, 686-694.

To...

*My beloved parents, Frazaneh and Mehrdad,
and
my only brother
for their unconditional love and support.*

To...

*Those who grow and inspire others to make the world a better place,
socially and environmentally!*

Also, to...

The 176 victims on flight PS752, including the students who didn't get the chance to graduate and the professors who missed their students' graduations. Had they lived, they could have made contributions in their areas of expertise beyond my imagination. They will always be remembered.

ACKNOWLEDGEMENTS

I would like to sincerely acknowledge my supervisor, Professor Larry Kostiuik, who has actively supported and patiently guided me throughout my Ph.D. program at the University of Alberta. I was always inspired by not only his scientific knowledge in the field of combustion but also his charming personality. I appreciate everything you have done for me.

I would also like to thank the technical and scientific support of my co-supervisor, Professor Jason Olfert, from whom I have learned a lot thanks to his broad knowledge of aerosol science. I also appreciate him for generously offering me the opportunity to use his lab space and aerosol measurement devices for my experiment.

I also thank Professor Morris Flynn, the other member of my supervisory committee, for his insightful comments over the course of this study. I also appreciate Dr. Ehsan Abbasi-Atibeh, a postdoctoral fellow in our research group, for his invaluable support and training on the PIV system.

I am also thankful to Professor Kyle Daun at the University of Waterloo for providing a collaborative opportunity by bringing a hyperspectral camera to our lab. I enjoyed working with him and his research group during the experimental campaign.

Thanks to Kerry Chen, Abbas Ahsan, Hamze Ahsan, Sina Mobaseri, and other colleagues in the lab. Having their company throughout this academic adventure was delightful.

Last but not least, I would like to thank the Natural Sciences and Engineering Research Council of Canada (NSERC) FlareNet Strategic Network, which provided the research funding and the opportunity to attend several conferences while pursuing my Ph.D. I am also grateful to the funding agencies at the University of Alberta that generously supported my research through these scholarships, the Sadler Graduate Scholarship and the Doctoral Recruitment Scholarship.

TABLE OF CONTENTS

Abstract	ii
Preface	iv
Dedication	v
Acknowledgements	vi
Table of Contents	vi
List of Tables	x
List of Figures	xi
List of Symbols	xiii
Abbreviations	xvi
1 Introduction and Background	1
1.1 Motivation: Flaring and Assisted Flares	1
1.2 Flare Emission Studies	6
1.3 Relevant Jet Diffusion Flame Studies	9
1.4 Objectives and Problem Statement	12
1.5 Thesis Outline	13
2 Investigation I: Jet Diffusion Flame in a Co-annular Burner at Full Range of Co-flow	15
2.1 Introduction	15
2.2 Experimental Setup and Methodology	22
2.3 Results and Discussion	27
2.3.1 Visual Observations	27
2.3.2 Geometry A: Carbon Conversion Efficiency and Emission Indices	30
2.3.3 Geometry B: Carbon Conversion Efficiency and Emission Indices	39
2.4 Concluding Remarks	42

3	Investigation II: Jet Diffusion Flame in a Co-annular Burner at Low Range of Co-flow	44
3.1	Introduction	44
3.2	Experimental Setup & Methodology	49
3.3	Results and Discussion	52
3.3.1	Hydrodynamic and Thermal Characterization	52
3.3.2	Emissions Comparison	53
3.4	Concluding Remarks	56
4	Multi-slot Burner Design	58
4.1	Introduction	58
4.2	Single Slot Design	60
4.2.1	Flow Simulation	61
4.2.2	PIV Experiments	65
4.3	Final Design	68
4.3.1	Sample Reacting flow PIV	73
4.4	Concluding Remarks	74
5	Investigation III: Co-flow Jet Diffusion Flame in a Multi-slot Burner	75
5.1	Introduction	75
5.2	Experimental setup and methodology	79
5.2.1	Multi-slot Burner Design	79
5.2.2	Near-exit Velocity Field Measurements and Flame Visualization	82
5.2.3	Emission Measurements	84
5.2.4	Data Analysis and Presentation	84
5.3	Results and discussion	85
5.4	Concluding Remarks	95
6	Conclusion and Future Work	98
6.1	Concluding Remarks	98
6.2	Future Work	101
	References	103
A	Uncertainty Calculation	120
A.1	Definition	120
A.1.1	Precision Uncertainty (P_x)	121
A.1.2	Bias Uncertainty (B_x)	122
A.1.3	Uncertainty Propagation	122
A.2	Uncertainty Analysis (Emission Index)	124
B	Steam Supply System	126
B.1	Steam Generator	126
B.2	High Flow Rates to Burner	127

B.3 Low Flow Rates to Burner	128
C Particle Image Velocimetry in Combustion Systems	130
D Multi-slot Burner Drawings	133

LIST OF TABLES

2.1	Experimental matrix of Investigation I	25
2.2	Uncertainty analysis of CCE, EI_{NO_x} , and EI_{BC} for Geometry A	31
3.1	Experimental matrix of Investigation II	51
4.1	Flow simulation cases for flow uniformity of wide single slot	63
4.2	PIV test matrix for flow uniformity of the single slots	66
4.3	Flow configuration of each slot for different diffusion flames in the multi-slot burner	70
5.1	Area-averaged velocities and measured characteristics at different \bar{V}_r .	86

LIST OF FIGURES

1.1	Flare stack with smoking flame in a mild crosswind.	2
1.2	Global gas flaring and oil production 1996 to 2021 (flaring only at upstream oil & gas and LNG plants).	3
1.3	Schematic of external or internal nozzles in an assisted flare.	6
2.1	Schematic of the experimental setup in Investigation I.	22
2.2	Flame images for selected air- and steam-assisted cases.	28
2.3	CCE (first row), EI_{BC} (second row), and EI_{NO_x} (third row) for Geometry A	34
2.4	CCE (left column) and EI_{NO_x} (right column) for Geometry B	40
3.1	Schematic of the experimental setup in Investigation II.	50
3.2	Adiabatic flame temperature vs. Assist/Fuel MFR	52
3.3	EI_{NO_x} (left column) and EI_{BC} (right column) for Investigation II	54
3.4	Particle size distribution for steam-assisted (left column) and water-assisted (right column) flames	56
4.1	Schematic of the preliminary design of multi-slot burner	59
4.2	Schematic of the initial design of a single slot made of plexiglass	60
4.3	Simulated exit velocity profiles of the wide slot at two different porosities	63
4.4	Exit velocity contour of the wide slot ($\epsilon = 0.39$)	64
4.5	Simulated exit velocity profiles of wide slot at three different H_b ($\epsilon = 0.39$)	64
4.6	Experimental setup for cold flow and reacting flow PIV	65
4.7	Exit velocity profiles at the mid planes of Wide Single Slot	67
4.8	Exit velocity profiles at the mid planes of Narrow Single Slot	68
4.9	Schematic of the final design of multi-slot burner and its dimensions	69
4.10	SLR images of different methane diffusion flames stabilized in the designed multi-slot burner.	71
4.11	Raw PIV image of an interacting IDF in a NFD case.	73
5.1	Schematic of the experimental setup.	80
5.2	Multi-slot burner and its sectional view.	81
5.3	Upward exit velocity profiles at $z = 2$ mm and $x =$ mid plane of each slot.	83
5.4	Upward exit velocity profiles at $z = 2$ mm and $y = 0$ mm.	83

5.5	Far-field and near-field flame images by SLR and PIV cameras. Left side: whole flame images at four test conditions. The blue lines are 2D projection of the flame surface. Right side: PIV and corresponding SLR images.	87
5.6	Instantaneous velocity field and streamlines at selected velocity ratios (note the description of bold streamlines in the text); the black blocks at $z = 0$ represent burner walls.	90
5.7	Average velocity magnitude of the streamlines indicated in Fig. 4 as a function of height above the burner with 95% confidence bands . . .	92
5.8	Emission indices at different velocity ratios annotated by the defined flame categories (i) to (iv).	94
B.1	Electric steam generator and its components	126
B.2	P&ID of the system supplying high flow rates of steam	128
B.3	P&ID of the system supplying low flow rates of steam	128
D.1	Assembled multi-slot burner with detailed dimensions (in inches). . .	134
D.2	End plates (dimensions in inches).	135
D.3	Outer part of the 1.5-in spacer (dimensions in inches).	136
D.4	Middle part of the 1.5-in spacer (dimensions in inches).	137
D.5	Inner part of the 1.5-in spacer (dimensions in inches).	138
D.6	divider (dimensions in inches).	139
D.7	0.375-in spacer (dimensions in inches).	140
D.8	0.375-in middle spacer (dimensions in inches).	141

LIST OF SYMBOLS

Greek and Latin

γ	flow uniformity index
Δ	difference/drop
ϵ	porosity
ρ	density
A	area
c_p	specific heat capacity at constant pressure
d	inner diameter
D	outer diameter or diameter
D	dilution
g	gravitational acceleration
H	height
I_W	interrogation window size
L	length
M	molecular mass
\dot{m}	mass flow rate [kg/s]
\dot{n}	molar flow rate
N	number concentration
o	origin

O	offset
p	pressure
Re	Reynolds number
Ri	Richardson number
R_u	universal gas constant [8.314 J/mol K]
S	cross-section area
t	time
T	temperature
v	velocity [m/s]
V	characteristic volume
\bar{V}_r	average velocity ratio
w or W	width [mm]
X	mole fraction
Y	mass fraction

Subscripts

0	characteristic value
A	air
ab	above bead
b	bead
e	exit
F	fuel
I	inner
j	species index

o	outer
pl	plenum
r	ratio
s	slot
z	upward (in z -direction)

Superscripts

^o	calculated based on MFC readings
-	area-averaged

ABBREVIATIONS

2C	Two-component
2D	Two-dimensional
AER	Alberta Energy Regulator
API	American Petroleum Institute
BC	Black Carbon
bcm	billion cubic meters
CCE	Carbon Conversion Efficiency
CE	Combustion Efficiency
CPC	Condensation Particle Counter
CO ₂	Carbon Dioxide
DMA	Differential Mobility Analyzer
EI	Emission Index
EPA	Environmental Protection Agency
EqvAir	Equivalent Air-assisted
EqvSteam	Equivalent Steam-assisted
GGFR	Global Gas Flaring Reduction
GWP	Global Warming Potential
HC	Hydrocarbons
HFR	Higher Flow Rate

HHV	Higher Heating Value
IDF	Inverse jet Diffusion Flame
IEA	International Energy Agency
IR	Infrared
LHV	Lower Heating Value
LII	Laser Induced Incandescence
MFC	Mass Flow Controller
MFR	Mass Flow Ratio
mln bbl/d	million barrels per day
NDF	Normal jet Diffusion Flame
Nd:YAG	Neodymium-doped Yttrium Aluminum Garnet
Nd:YLF	Neodymium-doped Yttrium Lithium Fluoride
NO _x	Oxides of Nitrogen
PAH	Polycyclic Aromatic Hydrocarbon
PAX	Photoacoustic extincniometer
PI	Particle Image
P&ID	Piping and Instrumentation Diagram
PIV	Particle Image Velocimetry
p/mm	pixel-to-millimeter ratio
PSD	Particle Size Distribution
PTFE	Polytetrafluoroethylene
RTD	Resistance Temperature Detector
Sky-LOSA	line-of-sight attenuation of skylight
SLPM	Standard Liters Per Minute
SLR	Single-Lens Reflex
SMPS	Scanning Mobility Particle Sizer
VI	Virtual Instrument

CHAPTER 1

Introduction and Background

An overview of the primary motivation of this study, about gas flaring and assisted flares in both industrial and laboratory scales, the relevant jet diffusion studies in various geometries, the problem statement and objectives, and finally, the outline of this thesis are covered in this chapter.

1.1 Motivation: Flaring and Assisted Flares

Over the past few decades, global concerns have escalated regarding the increasing trend in measured and anticipated temperature of Earth's atmosphere (Solomon et al., 2009). This increasing trend is strongly linked to the global and local changes in the atmospheric composition, not only in the gaseous phase but also in the particulate phase, with the most notable contributors being carbon dioxide (CO_2), methane (CH_4), and black carbon (BC) (Solomon et al., 2009; Lelieveld et al., 1993; Moosmüller et al., 2009). Despite the fact that methane is a frequently used fuel, the other two are products of either the efficient or inefficient oxidation process of carbon- or hydrocarbon-based compounds in diverse applications across the world. The principal

anthropogenic contributor to our changing atmosphere across the world is admittedly fossil fuel combustion. On a more local scale, different means of combustion can also lead to an increase in the concentrations of other harmful compounds, such as carbon monoxide (CO), oxides of nitrogen (NO_x), volatile organic compounds, and polycyclic aromatic hydrocarbons (Fawole et al., 2016; Shi et al., 2015).

The research presented here is motivated by the industrial practice of *flaring*, which is the disposal of unwanted flammable gases or vapours by burning them in open atmospheric flames. As demonstrated in Fig. 1.1, flares are large-scale turbulent diffusion flames in an open atmosphere. Flaring is a challenging phenomenon to investigate because there are many parameters, such as fuel composition, crosswind, and exit geometry, to name but a few, which affect the produced noise level, radiation



Figure 1.1: Flare stack with smoking flame in a mild crosswind, source of the image (GGFRP, 2022).

field, emissions of gaseous and particulate pollutants, and the completeness of combustion (Brzustowski, 1976). In 2015, for instance, the global flared gas volume was estimated to be about 140 billion cubic meters (bcm) per year, with CH₄ being the primary fuel component being flared (Elvidge et al., 2018). Based on the trend presented in Fig. 1.2, despite the importance of reducing greenhouse gas emissions and transitioning to cleaner energy sources over the last decade, global gas flaring volumes have remained essentially constant, plateauing at around 144 bcm (GGFRP, 2022). In addition, during the same time period, global oil production increased slightly before the slight decrease in 2020 as a result of the COVID-19 pandemic, averaging around 80 million barrels of oil per day (mln bbl/d). It is also reported that, on an absolute volume basis, the top ten flaring countries in 2021 are responsible for 75 % of all gas flaring worldwide, while those countries only contribute to 50 % of the global oil production (GGFRP, 2022). Taking this into account, flaring, whose emission production is often underestimated (Stohl et al., 2013), will likely continue to significantly contribute to the global and local environmental issues mentioned above for the foreseeable future (Cloy et al., 2017). To assess the relative importance of these harmful emissions, one can use the global warming potential (GWP), which is defined

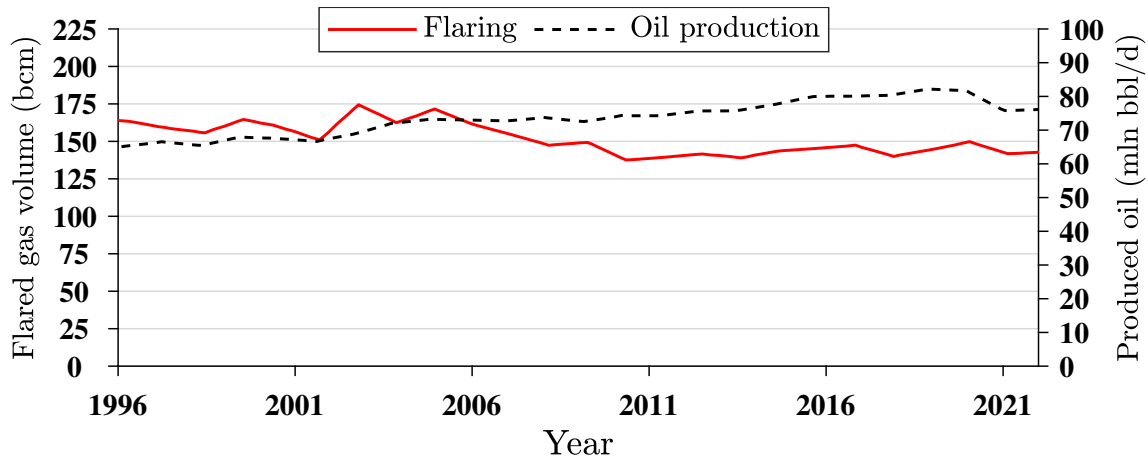


Figure 1.2: Global gas flaring and oil production 1996 to 2021 (flaring only at upstream oil & gas and LNG plants), data adopted from (GGFRP, 2022).

as the cumulative radiative forcing per unit mass of emissions of a particular species relative to the cumulative radiative forcing per unit mass of CO₂. Due to a high 100-year GWP of CH₄ and BC, 28–36 (Elvidge et al., 2018) and 840–1280 (Jacobson, 2007), respectively, it is highly preferred to maintain as efficient combustion as possible rather than venting unburnt combustible gases or having an inefficient flame (such as a sooting flame, fuel stripping (Johnson et al., 2001), or flame blow-off). In order to accomplish this, for instance, the US Environmental Protection Agency (EPA) set a 96.5% combustion efficiency threshold and mandated that visible flare emissions (*i.e.*, smoking) be limited to no more than five minutes every two hours (US Government Publishing Office, 2018).

According to their application and location, flares can be classified into three categories: upstream flares (near oil and gas recovery sites), downstream flares (at refineries and gas processing facilities), and industrial flares associated with the manufacturing sector and, respectively, they account for 90.6%, 8.4%, and 1% of the total volume of gas flared globally (Elvidge et al., 2018). In order to make the flares *smokeless* and highly efficient, in the 1950s, the American Petroleum Institute (API, 2014) proposed the notion of injecting an additional fluid into the flared gas close to the stack exit. This type of flare, later referred to as an *assisted flare*, was intended to increase the flared gas exit velocity, which enhanced the turbulence to better mix the fuel and air. Additionally, this efficient mixing lowers the overall sooting propensity, luminosity, and thermal radiation of the flare (Duck, 2011). Alternatively, assisting fluid injection can raise the manufacturing, operating, and maintenance costs (Stone et al., 1992b) as well as produce higher noise levels, which can be eliminated by using modified exit geometry (*e.g.* multiple small jets or acoustical shrouding) (Stone et al., 1992a).

The advantages of the assisting fluid injection are not monotonic with increasing

the flow rate, as over-aeration or over-steaming eventually reduces the conversion of the carbon in the hydrocarbon fuels to CO_2 (*i.e.*, carbon conversion efficiency (CCE)) and leads to significant emissions of volatile organic compounds and unburned fuels (Castiñeira and Edgar, 2006). From a broader perspective, the effects of adding a separate assisting fluid close to the base of these flames on emissions can be categorized into three mechanisms, namely hydrodynamics and mixing (*i.e.*, enhancing atmospheric air entrainment to the combustion zone) (Johnson et al., 2001; Castiñeira and Edgar, 2006; Devesh Singh et al., 2014), chemistry and combustion kinetics (*i.e.*, inhibiting solid carbon production, reacting with intermediate combustion products, and preventing the formation of long-chained compounds) (Castiñeira and Edgar, 2006; Devesh Singh et al., 2014; Dryer, 1977; Roberts et al., 2005), as well as thermodynamics (*i.e.*, acting like a thermal energy sink and lowering the characteristic temperature of the flame) (Duck, 2011; Castiñeira and Edgar, 2006; Dryer, 1977).

The study presented here attempts to contribute to a better general and generic understanding of assisted flares. In industrial assisted flares, there are many different geometries for how the flared gas and the assisting fluid are brought together (ANSI/API, 2008). These geometries are invariably designed such that the flared gas emerges vertically, either with or without generated swirl, mainly from a circular tube. The introduction of the assisting stream can take on many forms, but one standard categorization is whether the assisting fluid exits its tube or nozzles externally or internally to the flared gas stream (EPA, 2012), schematically depicted in Fig. 1.3. When it comes to the internal case, the assisting fluid is fully embedded in the flared gas stream, typically close to the exit plane of the flare. In contrast, in the case of steam-assisted flare, it can be introduced inside the flared gas stream before the exit plane to allow for some premixing (this premixing is not done with air-assisted flares to avoid flashback). Additionally, these internal assisting flows can be co-axial to the

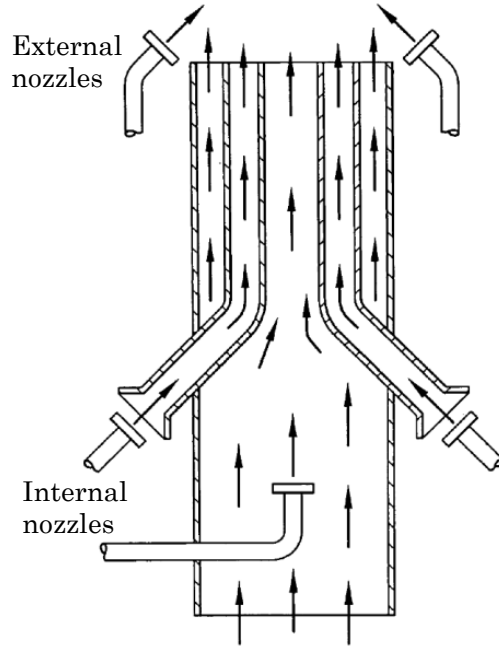


Figure 1.3: Schematic of external or internal nozzles in an assisted flare, figure retrieved from (Hong et al., 2006) and modified.

flare stream or arranged to create a swirl. On the other hand, in the external case, the assisting fluid can either be injected into the flared gas stream externally (usually by multiple opposed nozzles placed at angles oblique to the flare stream) or a single assisting flow that is co-axial to the flared gas stream.

1.2 Flare Emission Studies

Generally speaking, the relevant flare studies can be classified into two categories, namely laboratory-scale and industrial field-scale (including pilot-scale) investigations. The emission indices (EI) of various exhaust products are commonly characterized as the mass of a particular species emitted in the plume per unit mass of gas flared (Corbin and Johnson, 2014),

$$\text{EI}_j = \frac{\dot{m}_{j, \text{produced}}}{\dot{m}_F} \quad (1.1)$$

where \dot{m}_j and \dot{m}_F represent the mass flow rate of particular species and the fuel or flared gas, respectively. Emissions from field-scale flares has been measured using a variety of methods, including collecting the entire plume by a hood (Pohl et al., 1986) or a portion of the plume (Torres et al., 2012), sampling through stationary probes in the plume (Stroscher, 2000), and sampling through a single-point probe moving across the plume supported by a crane (McDaniel and Tichenor, 1983) or carried by aircraft (Weyant et al., 2016; Gvakharia et al., 2017). In all cases except the one collecting the entire plume, there is a concern that the sampled emissions are not a proper representative of the whole. Furthermore, non-intrusive imaging techniques have also been employed, such as visible infrared (IR) imaging radiometer (Elvidge et al., 2016), hyper-spectral imaging (Miguel et al., 2021) or multi-spectral IR imaging (Zeng et al., 2016), and line-of-sight attenuation of the skylight (Sky-LOSA) (Johnson et al., 2011), but they all face the challenge of converting light intensity data into concentration-based data, which is then turned into mass flows to calculate emission factors (indices).

Air-assisted flares have become more common in the US lately (Cheremisinoff, 2013), although steam is used in the majority of industrial assisted flares (Castiñeira and Edgar, 2006) due its to higher smoke suppression capacity. Assisting air typically supplies only 15–50% of the stoichiometric air needed for complete combustion (Baukal Jr, 2001), while the remainder comes from ambient air. For example, in the study conducted by Torres et al. (2012), full-scale industrial flares were tested using low lower heating value (LHV) fuels (fuels diluted by nitrogen) at low flow conditions (0.1% to 0.65% of the flare’s design full capacity). Both an internally air-assisted flare and an externally steam-assisted flare were included in their experiments. Their findings revealed that the destruction efficiency (*i.e.*, the fraction of the flared gas that reacted) of steam-assisted flares dramatically decreases when the heating value in the combustion zone becomes less than 9.3 MJ/m³. Moreover, the

destruction efficiency of the air-assisted flares decreases linearly with the air flow rate. Torres et al. (2012) also explored the effect of crosswind on the performance of steam- and air-assisted flares. For both flares, the wind speed was in the range of 0 – 7.2 m/s, and the deviation in the destruction efficiency compared to no crosswind case was less than 2.5 %. Although these studies did not report emission indices of emitted species, they focused on the destruction efficiency trend.

In another field-scale study, McDaniel and Tichenor (1983) determined the overall hydrocarbon destruction efficiency and combustion efficiency (CE) for both air- and steam-assisted smokeless flares, despite the fact that the flared gas was “crude propylene” ($\approx 80\%$ propylene + 20% propane), which has a relatively high soot propensity. Furthermore, only soot mass concentration was reported for the unassisted smoking case, but its emission indices were not included because the dilution ratio of the samples was unknown. In a more recent study, in order to enable continuous real-time monitoring of CE in full-scale industrial assisted flares (steam-assisted, air-assisted, and pressure-assisted flares), a relatively new method based on hyper-spectral or multi-spectral IR imaging was developed (Zeng et al., 2016), and the results were validated with an extractive sampling method. In their study, CO and soot emissions were ignored in the CE calculation, even though they can be relatively large for an inefficient flare, specifically CO (Ismail and Umukoro, 2016). To clarify this, Pohl et al. (1986) explained that the formation of CO can be from two alternative partial oxidation pathways, namely, starting from the soot or from the hydrocarbon fuel itself, with the latter one being the dominant pathway in the chemical mechanism.

In addition to the assisted flare studies that were discussed previously, a few field-scale studies have been published on unassisted flares. Johnson et al. (2011) conducted some field measurements to quantify the soot emissions from an unassisted flare at a petrochemical plant using Sky-LOSA and image correlation velocimetry

of the unconfined atmospheric plume. However, neither the efficiency measure nor the composition of the flared gas was documented. Strosher (2000) investigated the completeness of the flaring process and characterized the emissions from a field-scale flare at an oil-field site in Alberta, Canada. It was demonstrated that the CE of the unassisted diffusion flares was inversely proportional to the amount of liquid fuel mixed with the flared gas, and crosswinds, in general, resulted in more unburned fuel and pyrolytically-formed hydrocarbons that were emitted from the flare. The quantification of the NO_x and soot emission indices was not, however, a part of their extensive field measurements.

1.3 Relevant Jet Diffusion Flame Studies

In a lab-scale flare study, the CCE of diffusion flames in a crosswind was experimentally investigated in a closed-loop wind tunnel (Johnson and Kostiuk, 2000). A tube burner was used to model an unassisted flare, burning propane, natural gas, or propane/ CO_2 as the fuel. An increase in crosswind speed resulted in a reduction in the CCE, whereas an increase in jet exit velocity mitigated the adverse effects of crosswind. Also, the leading source of inefficiencies was fuel stripping, which is the process by which unburned fuels escape from the flame zone as a result of local extinctions. Another recent lab-scale investigation observed an unexpected pattern of increasing BC emissions at low assisting air flow rates that abruptly reversed itself at slightly higher assisting air flow rates, and the cause of the observed trends in BC emissions was not pinpointed (Zamani et al., 2021). Therefore, further investigation is warranted on the BC emissions with increasing assisting air flow rates by zooming into the regions of air flow rates where these unexpected trends occur to examine the universality of such findings, which is a part of the focus of this study. This transition in BC emissions was once again attempted to be resolved in an axisymmetric

co-annular configuration in two scaled geometries (Mobaseri, 2021). Still, that study was unable to decouple the effects of the air-to-fuel mass flow ratio and the inner tube wall thickness on the outcomes.

Because there aren't many lab-scale studies on assisted flares in the literature where the assisting fluid is internal to the fuel flow, it is advantageous to take into account some comparable configurations in the combustion research community, such as inverse jet diffusion flames (IDF). Numerous investigations on different types of diffusion flames and their underlying physics have been published in the literature on combustion science (Zhen et al., 2021). IDFs are a category of diffusion flames that differ from normal jet diffusion flames (NDF) in that the oxidizer and fuel positions are swapped. IDFs are composed of an annular jet of fuel, or a number of circular jets of fuel surrounding an inner jet of air (Blevins et al., 2002; Oh et al., 2005; Sobiesiak and Wenzell, 2005; Ying and Liu, 2018; Sidebotham and Glassman, 1992; Zhang et al., 2012; Elbaz and Roberts, 2014, 2016; Sze et al., 2006; Zhen et al., 2011; Kapusta et al., 2020). These air and fuel flows may be either surrounded by an inert gas shield to isolate the flame from disturbances of the surrounding air (Blevins et al., 2002; Oh et al., 2005; Sobiesiak and Wenzell, 2005; Ying and Liu, 2018), bounded within rigid boundaries to prevent interactions with ambient air currents (Sidebotham and Glassman, 1992; Zhang et al., 2012; Elbaz and Roberts, 2014, 2016), unconfined in a quiescent atmosphere to allow ambient air entrainment (Sze et al., 2006; Zhen et al., 2011; Kapusta et al., 2020), or confined in a controlled air flow (Lim et al., 2017).

Regarding the internally air-assisted flares that were previously addressed, their configuration is similar to that of the unconfined IDF in a quiescent atmosphere, but they are different in practice. In this configuration, an outer NDF is created in the outer mixing layer established with the quiescent air, which places an IDF and an

NDF adjacent to each other. IDFs have the advantageous properties of both premixed and diffusion flames in terms of application, namely, emitting less pollutants and preventing flashback, respectively (Dong et al., 2007). The majority of the relevant studies on this topic concentrated on the morphology or formation process of soot particles (Blevins et al., 2002; Oh et al., 2005; Ying and Liu, 2018; Sidebotham and Glassman, 1992), the overall flame structure and its distinct local zones, and degrees of partial premixing in IDFs (Sobiesiak and Wenzell, 2005; Zhang et al., 2012; Elbaz and Roberts, 2014, 2016; Zhen et al., 2011; Kapusta et al., 2020). With the exception of Sze et al. (2006), who investigated the emission index of NO_x for a range of overall equivalence ratios in addition to the IDF structure. Also, it is important to point out a study by Lim et al. (2017), which was primarily concerned with determining the optical characteristics of soot particles with different organic carbon contents in a triple co-flow burner with constant inner air flow and increasing outer air flow to control the degree of carbonization of the emitted soot particles. Their finding is significant because it shows that the presence of a small IDF inside the main flame increases the temperature close to the nozzle exit and the degree of fuel pyrolysis, both of which stimulate soot formation. One of the goals of the current study is to address this knowledge gap because neither of these works examined the CCE trend nor simultaneously quantified NO_x and BC emissions.

Even though co-annular burner configurations have been the primary focus of IDF research, it has been demonstrated that the dynamics, stability, flame structure, and emissions are all impacted by the jet radius and curvature (Mansour, 2000). Besides, the area ratio of the streams in co-annular burners can also be altered by changing the inner or outer tube diameter. Slot burners, on the other hand, allow for independent adjustment of the width and length of each slot (Kapusta et al., 2020). Therefore, it is valuable to take into account the burner configurations similar to the

Wolfhard-Parker slot burner, the idea of which was first proposed in 1949 (Wolfhard and Parker, 1949). This burner created a 2D diffusion flame with a thicker reaction zone that had rectangular slots for the fuel and the oxidizer that were parallel to each other along their long side and were surrounded by a flow of inert gas. For the purpose of measuring in-flame emissions from an NDF in slot configuration, a modified Wolfhard-Parker slot burner was constructed that produced two symmetric flame sheets by sandwiching the fuel slot between two air slots (Kent et al., 1981; Smyth et al., 1985). This allowed for the analysis of the soot formation and particle generation rates inside a 2D diffusion flame. Recently, this type of burner was modified such that two N_2 purge slots were added at the ends of the fuel slot to eliminate the impact of end flames on the overall stability of the flame sheets (Wagner et al., 2009).

1.4 Objectives and Problem Statement

The main objective of this research is to explore a gap in the literature associated with the quantification of key emission metrics and the efficiency of internally-assisted jet diffusion flames as a surrogate for internally-assisted non-swirl flames. These have the common physical processes that occur in the shear-mixing layers between fluid streams of different compositions and velocities, chemical reactions within the layers that involved fuels and oxidizers, and the impacts of buoyancy. The following chapters focus on the published results of three connected investigations on co-flow jet diffusion flames in two co-annular burners and one multi-slot burner, respectively. In two co-annular burners, the key emission metrics considered are the overall CCE and the emission indices for BC and NO_x , and link these values to the hydrodynamics of the flow and existing models for the importance of peak temperatures in pollutant formation. In the slot burner investigation, changes in key emission metrics (*i.e.*, only BC and NO_x) are related to the flow field of an unconfined IDF inside an NDF by

studying the physical processes occurring in various 2D shear-mixing layers.

1.5 Thesis Outline

This thesis consists of six chapters, which are the results of three connected investigations on co-flow jet diffusion flames. A summary of the content of each of the following chapters is as follows:

Chapter 2 (Investigation I) demonstrates a simplified lab-scale internally assisted flare configuration to quantify CCE and EI of black carbon and oxides of nitrogen. The effects of the composition and flow rate of the fuel (methane or propane) and assisting fluid (air, steam, or inert gases), as well as the burner head geometry, were investigated in a burner constructed of two concentric tubes allowed for various generic burner geometries. The results showed that there was a range of assisting fluid flow rates, where the CCE was approximately 100 %, while the emission of black carbon and nitrogen oxides were highly suppressed.

Chapter 3 (Investigation II) discusses another simplified lab-scale internally assisted flare configuration focusing on low flow rates of assisting fluid (steam or atomized water) to compare their effectiveness in suppressing soot formation and NO_x emissions during flaring. The three fuels at constant flow rates used in this study were pure propane, pure methane, and a mixture of 90 % methane and 10 % propane, the latter approximating the typical volumetric higher heating value of Alberta flare gas. The results show that both liquid water and steam reduce NO_x and BC mass emissions; however, liquid water reduces NO_x and BC emissions more than steam due to a stronger thermodynamic effect.

Chapter 4 provides the details of the design of a multi-slot burner that is used in Chapter 5. The detailed steps of designing the single slot are explained using flow simulation and particle image velocimetry (PIV) experiments. Some of the possible

diffusion flames that can be stabilized on this burner are also discussed.

Chapter 5 (Investigation III) was motivated by the application of internally air-assisted flames and recent anomalous data that BC emissions changes are not monotonic with the amount of air added inside the fuel stream, a burner was designed (Chapter 4) to study the flow, emissions, and stability aspects of the existence of both normal and inverse jet diffusion flames in close proximity. Since the radius of curvature of a burner affects all aspects of combustion, such as dynamics, stability, flame structure, and emissions, a slot burner configuration was adopted. This multi-slot burner consists of five parallel rectangular slots, producing flame sheets at each fuel-air mixing layer with open optical access to all the flows. The experimental test conditions involved constant flows of outer air and propane and variable inner air flow. Only when the inner flame finally lifted off due to the inner air flow, did the BC emissions collapse to near zero. Phenomenological models associated with the importance of partial premixing were proposed to explain this collapse, thereby generalizing this finding to other combustion systems when attempting to reduce BC emissions through secondary internal air addition.

Chapter 6 presents a summary of findings and conclusions as well as proposals for future studies.

CHAPTER 2

Investigation I: Jet Diffusion Flame in a Co-annular Burner at Full Range of Co-flow^{1, 2}

2.1 Introduction

Concerns have escalated over the past few decades regarding the measured and predicted trends in the increase in the temperature of the earth's atmosphere (Solomon et al., 2009). This increase is associated with compositional changes in the atmosphere of both gaseous and particulate phases, with the most notable components being carbon dioxide (CO₂), methane (CH₄), and black carbon (BC) (Solomon et al., 2009; Lelieveld et al., 1993; Moosmüller et al., 2009). With one of these components being

¹Based on a published paper: **Zamani, M.**, Abbasi-Atibeh, E., Mobaseri, S., Ahsan, H., Ahsan, A., Olfert, J. S., and Kostjuk, L. W. (2021). An experimental study on the carbon conversion efficiency and emission indices of air and steam co-flow diffusion jet flames. *Fuel*, 287:119534.

²Based on a published paper: Miguel, R. B., Talebi-Moghaddam, S., **Zamani, M.**, Turcotte, C., and Daun, K. J. (2021). Assessing flare combustion efficiency using imaging Fourier transform spectroscopy. *Journal of Quantitative Spectroscopy and Radiative Transfer*, 273, 107835.

a ubiquitous fuel, and the others being products of either effective or ineffective oxidation processes, combustion unsurprisingly is at the center of direct anthropogenic contributions to our changing global atmosphere. On a more local level, combustion is also associated with elevating the concentrations of other undesirable compounds, such as carbon monoxide (CO), oxides of nitrogen (NO_x), volatile organic compounds, and polycyclic aromatic hydrocarbons (Fawole et al., 2016; Shi et al., 2015).

The motivation for the research presented here is the industrial practice of *flaring*, which is the disposal of unwanted flammable gases or vapors by burning them in open atmospheric flames. Flares are turbulent diffusion flames; hence, flaring is a complicated phenomenon, in which parameters, such as fuel composition, crosswind, and exit geometry, affect the produced noise level, radiation field, emissions of soot and gaseous pollutants, and the completeness of combustion (Brzustowski, 1976). With the most dominant fuel component being CH₄, the quantity of globally flared gas was estimated to be 140 billion cubic meters annually in 2015 (Elvidge et al., 2018), and flaring is, therefore, a notable contributor to the global and local issues mentioned above (Cloy et al., 2017). A way to quantify the relative importance of these emissions is by global warming potential (GWP) defined as the cumulative radiative forcing per unit mass of emissions of a particular species relative to the cumulative radiative forcing per unit mass of CO₂. Since CH₄ and BC have a 100-year GWP of 28–36 (Elvidge et al., 2018) and 840–1280 (Jacobson, 2007) respectively; maintaining efficient combustion is highly desirable compared to venting or having an inefficient flame (*e.g.*, a sooting flame, fuel stripping (Johnson et al., 2001), or flame blow-off). To this end, the United States Environmental Protection Agency (EPA) set a threshold for the combustion efficiency at 96.5%, and restricted visible flare emissions (*i.e.*, smoking) to be less than five minutes in two consecutive hours (US Government Publishing Office, 2018).

Flares can be categorized into three groups in terms of their application; upstream flares (near oil and gas recovery sites), downstream flares (at refinery and gas processing facilities), and industrial flares associated with the manufacturing sector, and they respectively contribute 90.6 %, 8.4 %, and 1 % to global volume of gas flared (Elvidge et al., 2018). In the 1950s, the concept of injecting an additional fluid into the flared gas near the stack exit was recommended by the American Petroleum Institute (API, 2014) to create *smokeless* and high-efficiency flares. The stated intent of this type of flare was to increase the flared gas exit velocity, which enhanced the turbulence for mixing the fuel with air and became known as an *assisted flare*. Furthermore, this mixing reduces the sooting propensity, luminosity, and thermal radiation of the flame (Duck, 2011). The positive impacts of the assisting fluid are not monotonic with their increasing flow as over-aeration or over-steaming eventually reduces the conversion of the carbon in the hydrocarbon fuels to CO₂ (*i.e.*, carbon conversion efficiency (CCE)) and results in a significant emission of volatile organic compounds and unburned fuels (Castiñeira and Edgar, 2006).

The research presented here is to contribute to a better general and generic understanding of assisted flares. Industrial assisted flares exist with a multitude of geometries for how the flared gas and the assisting fluid are brought together (ANSI/API, 2008). These geometries invariably involve the flared gas emerging vertically, either with or without induced swirl, from an overall circular conduit. The introduction of the assisting stream can take on many forms, but one common categorization is whether the assisting fluid exits its conduit or nozzles externally or internally to the flared gas stream (EPA, 2012). For the external case, the assisting fluid can either be directed into the flared gas stream (usually by multiple opposed nozzles arranged at angles oblique to the flare stream) or a single assisting flow that is co-axial to the flared gas stream. Alternately, for the internal case, the assisting fluid is fully

embedded in the flared gas stream, typically near the exit plane of the flare, while in the case of steam-assist it can be introduced in the flared gas before the exit plane to allow for some premixing (this premixing is not done with air-assist to preclude flashback). These internal assisting flows can also be co-axial to the flare stream or arranged to create a swirl.

The relevant literature can be divided into two parts, namely, industrial field-scale (including pilot-scale) and laboratory-scale studies. The emission indices (EI) of various exhaust products are defined as the mass of a specific compound emitted in the plume per unit mass of gas flared (Corbin and Johnson, 2014), $EI_j = (\dot{m}_{j, \text{produced}} / \dot{m}_F)$, where j represents a specific species and F represents the flared gas. Quantifying the emissions of field-scale flares has been done by collecting the entire plume by a hood (Pohl et al., 1986) or a part of the plume (Torres et al., 2012), sampling through stationary probes in the plume (Stroscher, 2000), sampling through a single-point probe moving across the plume held by a crane (McDaniel and Tichenor, 1983) or carried by an aircraft (Weyant et al., 2016; Gvakharia et al., 2017). In all cases other than collecting the whole plume, there is a concern that the sampled emissions are not representative of the whole. Non-intrusive imaging techniques, such as visible infrared imaging radiometer (Elvidge et al., 2016), hyper-spectral or multi-spectral infrared imaging (Zeng et al., 2016), and line-of-sight attenuation of skylight (Sky-LOSA) (Johnson et al., 2011), have also been used but come with the challenge of turning light intensity data into concentration-based data and then into mass flows to create emission factors.

The majority of industrial assisted flares use steam due to their higher smoke suppression capacity (Castiñeira and Edgar, 2006); however, air-assisted flaring has recently increased in the US (Cheremisnoff, 2013). This assisting air usually provides only 15–50 % of the stoichiometric air required (Baukal Jr, 2001), and the rest comes

from the ambient. Torres et al. (2012) conducted full-scale industrial flare tests at low flow (0.1 % to 0.65 % of the flare’s design full capacity) and low lower heating value (LHV) fuels (fuels diluted by nitrogen). In their experiments, both an internally air-assisted flare and an externally steam-assisted flare were tested. The results showed that the destruction efficiency (*i.e.*, the fraction of the flared gas that reacted) for steam-assisted flares drops noticeably when the heating value in the combustion zone falls below 9.3 MJ/m³. In addition, the destruction efficiency drops linearly with air flow rate in air-assisted flares. Torres et al. (2012) also investigated the effect of ambient conditions (*i.e.*, crosswind) on steam- and air-assisted flare performance. For both flares, operated with wind speeds of 0–7.2 m/s, the deviation in the efficiency from no crosswind was less than 2.5 %. In these studies, the focus was on the destruction efficiency trend, but the emission indices were not reported.

Among these field-scale studies, McDaniel and Tichenor (1983) calculated the total hydrocarbon destruction efficiency and combustion efficiency (CE) for both air- and steam-assisted smokeless flares, although the flared gas was “crude propylene” (\approx 80 % propylene + 20 % propane), having a high soot propensity. In addition, soot mass concentration was only reported for the unassisted smoking case, but its emission indices were not included because of the unknown dilution ratio of the samples. A relatively new method based on a hyper-spectral or multi-spectral infrared (IR) imaging was developed for a real-time continuous monitoring of CE in full-scale industrial assisted flares (steam-assisted, air-assisted, and pressure-assisted flares) (Zeng et al., 2016), which was validated with an extractive sampling method. In their study, CO and soot emissions were ignored in the CE calculation, even though they can be relatively large for an inefficient flare, specially CO (Ismail and Umukoro, 2016). This was explained by Pohl et al. (1986) that the production of CO can be from two different pathways, namely, soot oxidation and direct derivation from hydrocarbons, with the

second one being the major pathway.

There are a few field studies published on unassisted flares. Johnson et al. (2011) conducted field measurements to quantify the soot emissions of an unassisted flare at a petrochemical plant using Sky-LOSA and image correlation velocimetry of the unconfined atmospheric plume. They did not report the composition of the flared gas or measures of efficiency. Stroscher (2000) investigated the completeness of the flaring process and characterized the emissions from a field-scale flare at an oil-field site in Alberta, Canada. It was shown that the CE of the unassisted diffusion flares was inversely proportional to the amount of liquid fuel directed to flared gas, and crosswinds caused more unburned fuel and pyrolytically-produced hydrocarbons to emit from the flare, but the emission indices of NO_x and soot were not considered in their field measurements. In a lab-scale setting, the CCE of diffusion flames in a crosswind was experimentally explored in a closed-loop wind tunnel (Johnson and Kostiuik, 2000). A tube burner used propane, natural gas, or propane/ CO_2 as the fuel to model an unassisted flare. Results revealed that the increase in crosswind speed caused a decrease in the CCE, while the increase in jet exit velocity diminished the negative impact of crosswind. Additionally, fuel stripping (*i.e.*, unburned fuels escaping from the flame zone due to the local extinctions) was the main cause of inefficiencies.

As there are limited lab-scale studies on assisted flares, where the assisting fluid is internal to the fuel flow, it is beneficial to consider some analogous configurations, such as inverse jet diffusion flames (IDF). Being a category of diffusion flames in which oxidizer and fuel positions are switched compared to normal diffusion flames, IDFs consist of an inner jet of air surrounded by an annular jet or multiple circular jets of fuel. These flows may be either surrounded by an inert gas shield to isolate the flame from the surrounding air (Blevins et al., 2002; Oh et al., 2005; Sobiesiak and

Wenzell, 2005; Ying and Liu, 2018), confined in a rigid shield to avoid interactions with ambient air currents (Sidebotham and Glassman, 1992; Zhang et al., 2012; Elbaz and Roberts, 2014, 2016), or unconfined in a quiescent atmosphere to allow ambient air entrainment (Sze et al., 2006; Zhen et al., 2011; Kapusta et al., 2020). The air-assisted cases in this paper are geometrically analogous to the latter one, but analytically distinct. Except Sze et al. (2006) that studied not only the emission index of NO_x for a range of overall equivalence ratio, but also the IDF flame structure, the other studies were concentrated on the morphology or formation process of soot particles (Blevins et al., 2002; Oh et al., 2005; Ying and Liu, 2018; Sidebotham and Glassman, 1992) or the overall flame structure and its local distinct zones as well as degrees of partial premixing in IDFs (Sobiesiak and Wenzell, 2005; Zhang et al., 2012; Elbaz and Roberts, 2014, 2016; Zhen et al., 2011; Kapusta et al., 2020). However, these works neither evaluated the CCE trend nor simultaneously quantified NO_x and soot emissions.

The main objective of this research is to explore a gap in the literature associated with the quantification of key emission metrics and efficiency of internally-assisted jet diffusion flames as a surrogate for internally-assisted non-swirl flames. These have the common physical processes that occur in the shear-mixing layers between fluid streams of different compositions and velocities, chemical reactions within the layers that involved fuels and oxidizers, and the impacts of buoyancy. The key emission metrics considered are the overall CCE, and the emission indices for BC and NO_x , and link these values to the hydrodynamics of the flow and existing models for the importance of peak temperatures in pollutant formation.

2.2 Experimental Setup and Methodology

Jet diffusion flames, produced in co-axial burners constructed of two concentric tubes, were burned in a quiescent environment. These experiments explored the effects of fuel and assisting fluid composition and their flow rates, as well as the changes in exit geometry, on CCE and emissions. In these experiments, methane (CH_4), propane (C_3H_8), and inert-diluted C_3H_8 were used as fuels, while steam, air, and gas mixtures having the same density as air or steam were used as co-flow assisting streams in various co-flow geometries. These experiments explored a wide range of parameters to identify their importance on CCE and EIs of various products.

The experimental setup, as depicted in Fig. 2.1, was comprised of two concentric

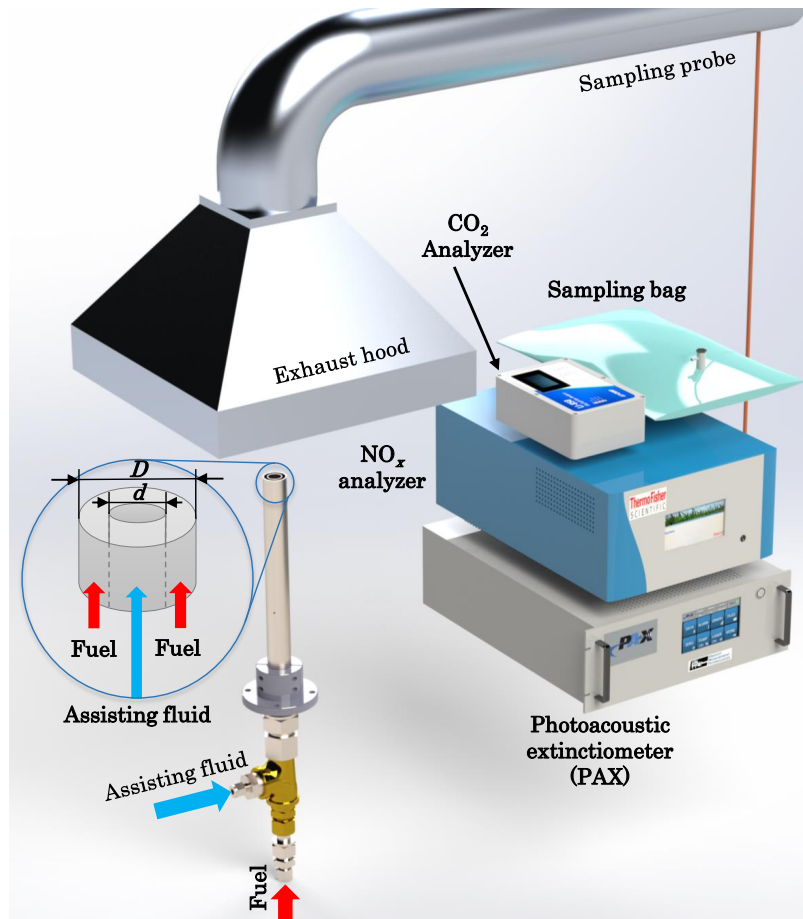


Figure 2.1: Schematic of the experimental setup in Investigation I.

co-axial stainless-steel tubes. The fuel and assisting fluid flowed through the annular space and the center tube, respectively. All combustion products were fully collected using a square exhaust hood. To verify that all combustion products were fully collected using a square exhaust hood, four resistance temperature detector probes were placed around the exhaust hood to monitor the temperature, and detect any overflowing of hot product gases outside the exhaust hood. The temperature readings were always close to the room temperature, which ensured that all the combustion products were collected. The exhaust hood was connected to a circular duct with a diameter of 0.3 m, where its flow rate was controlled by a Venturi valve to maintain a turbulent flow of products. Samples of exhaust gases were extracted through a sampling probe for species measurement. In order to get a well-mixed sample of the combustion products, the probe was installed in the duct 6 m downstream of the exhaust hood. Vertical mesh screens surrounding the burner provided an undisturbed environment while allowing for the air entrainment necessary for combustion. Further details of the setup can be found elsewhere (Ahsan et al., 2019).

Different burner geometries were created by varying the inner tube diameter and changing the vertical offset of the assisting fluid and fuel exit planes. The details of the experiments are presented in Table 2.1. The inner and outer diameter of the outer tube were fixed at $D_i = 22.9$ mm and $D_o = 25.4$ mm, while the inner and outer diameter of the inner tube were either $d_i = 11.3$ mm and $d_o = 12.7$ mm or $d_i = 5.54$ mm and $d_o = 6.35$ mm, referred to as Geometry A and B, respectively.

In Geometry A, CH_4 with assisting streams of air (CH_4 -Air) and steam (CH_4 -Steam) were used as base cases at a fixed fuel mass flow rate (\dot{m}_f) equivalent to 20 L/min at standard conditions of 25 °C and 101.325 kPa (denoted elsewhere as SLPM). The effects of changing the fuel type and its flow rate were tested by using C_3H_8 as the fuel, or by increasing the CH_4 flow rate to 40 SLPM. To explore the

relative effects of chemistry versus hydrodynamics of the assisting fluid, various gas compositions were used. The volume fractions of different gases in the mixture were selected such that the density, or the molecular mass (M), was similar to either air or steam, which are referred to as equivalent air-assisted (EqvAir) or equivalent steam-assisted (EqvSteam) cases, respectively. The EqvAir flows were based on changing the oxygen concentration to 0%, 10.5%, and 42% to contrast normal air with 21% O_2 . The EqvSteam flows were based on reducing the steam content to 50% and 0%, with the net effect being that the 0% O_2 and the 0% steam flows are both effectively inert, but of different densities and hence different momentum fluxes. It should be noted that the assisting co-flow mixtures had different specific heat capacities at constant pressure (c_{pas}); hence, replacing air or steam assisting co-flows with these mixtures did affect the characteristic adiabatic flame temperature (T_{ad}).

In Geometry B, the experiments focused on the effects of changing the LHV of the fuel, and offset the height of the assisting fluid with respect to the fuel exit plane. To decrease the volumetric LHV of the fuel (down to as much as 20% of pure C_3H_8), C_3H_8 was diluted by nitrogen (N_2), while keeping the total volumetric flow rate constant. In steam-assisted cases, the burner inner tube was moved ± 10 mm and ± 20 mm vertically to produce offset heights. To facilitate the discussion of results, the experiments are named in Table 2.1.

In addition, the fuel exit Reynolds numbers (Re_f) are presented in Table 2.1 to help characterize the experimental conditions. The assisting fluid Reynolds numbers (Re_{as}) at the tube exit ranged from zero (*i.e.*, unassisted) to values when the flame was blown off. Table 2.1 lists the Re_{as} values at the onset of blow-off and rapid decline in the CCE, referred to as the CCE collapse point. The Re_{as} for the CCE collapse ranged from 2,380 to 24,450 for air-assisted, and from 5,770 to 10,600 for steam-assisted cases.

Table 2.1: Experimental matrix of Investigation I; base cases (the first entry for each geometry with air/steam co-flow) are shaded. **Bold entries** highlight a change from base cases.

Exp. ID	Fuel composition (% Vol.)	\dot{m}_f (SLPM)	Re_f	Re_{as} (CCE collapse)	Assisting co-flow composition	c_{pas} (J/kg-K)	MFR at CCE \approx 96.5 %
Geometry A							
CH ₄ -Air	CH ₄	20	590	21470	air	1003	15.0
Different fuel							
C ₃ H ₈ -Air	C₃H₈	20	2280	21460	air	1003	5.3
Higher flow rate							
CH ₄ -Air-HFR	CH ₄	40	1250	24450	air	1003	8.5
Equivalent air assist							
CH ₄ -EqvAir-1	CH ₄	20	590	11110	92 % N₂ + 8 % Ar	981	7.7
CH ₄ -EqvAir-2	CH ₄	20	590	16390	85 % N₂ + 10.5 % O₂ + 4.5 % Ar	992	11.4
CH ₄ -EqvAir-3	CH ₄	20	590	26490	55 % N₂ + 42 % O₂ + 3 % He	1000	18.9
CH ₄ -Steam	CH ₄	20	580	5770	steam	1907	3.1
Different fuel							
C ₃ H ₈ -Steam	C₃H₈	20	2280	10600	steam	1907	2.2
Higher flow rate							
CH ₄ -Steam-HFR	CH ₄	40	1260	10190	steam	1908	2.8
Equivalent steam assist							
CH ₄ -EqvSteam-1	CH ₄	20	580	4900	58 % N₂ + 42 % He	1428	4.1
CH ₄ -EqvSteam-2	CH ₄	20	580	4130	50 % steam + 29 % N₂ + 21 % He	1672	2.8
Geometry B							
C ₃ H ₈ -Air	C ₃ H ₈	20	2700	12400	air	1003	1.40
Different fuel							
CH ₄ -Air	CH₄	20	690	13220	air	1003	4.33
Fuel dilution							
C ₃ H ₈ -Air-D60	60 % C₃H₈ + 40 % N₂	20	1820	11900	air	1003	1.47
C ₃ H ₈ -Air-D40	40 % C₃H₈ + 60 % N₂	20	1540	11070	air	1003	1.53
C ₃ H ₈ -Air-D20	20 % C₃H₈ + 80 % N₂	20	1370	2380	air	1003	NA
C ₃ H ₈ -Steam	C ₃ H ₈	20	2680	8950	steam	1907	0.74
Different fuel							
CH ₄ -Steam	CH₄	20	700	8260	steam	1907	2.03
Offset (mm)							
C ₃ H ₈ -Steam-O(+20)	C ₃ H ₈	20	2700	8950	steam	1907	0.83
C ₃ H ₈ -Steam-O(+10)	C ₃ H ₈	20	2620	9300	steam	1907	0.83
C ₃ H ₈ -Steam-O(-10)	C ₃ H ₈	20	2610	6830	steam	1907	0.62
C ₃ H ₈ -Steam-O(-20)	C ₃ H ₈	20	2690	6690	steam	1907	0.60

In these experiments, the overall hydrodynamics associated with momentum and buoyancy were non-dimensionalized by defining the overall Richardson number of the co-flow and annular jet (Ri) calculated as:

$$Ri = \frac{\text{buoyancy forces}}{\text{inertial forces}} = \frac{g(\rho_p - \rho_\infty)V}{\rho_f u_f^2 (D^2 - d^2) + \rho_{as} u_{as}^2 d^2} \quad (2.1)$$

where subscripts p, ∞ , f, and as denote products, ambient, fuel, and assisting fluid, respectively, u is velocity, g is gravitational field intensity (9.81 N/kg), V is a characteristic volume of product gases, and ρ is density. To calculate Ri , V is defined as

D^2L , where L is the characteristic flame height, which is calculated from processing the flame images. The Ri values for unassisted flames were an order of magnitude greater than 1, where $Ri > 1$ means that the flows are buoyancy-driven (Pohl et al., 1986). However, by increasing the assisting fluid flow rate, Ri became very much less than unity ($Ri \ll 1$) near blow-off, and the flow became momentum-dominated.

The steam was supplied by a steam generator and its flow measured by a calibrated cone flow meter (Ahsan et al., 2019) with an average absolute uncertainty of less than 2 g/min. The superheated steam was delivered using heated hoses with a set point temperature of 155 °C.

Fuels, air, and inert gases were delivered using mass flow controllers with an uncertainty of $\pm 1.8\%$ at 20 SLPM. In EqvSteam cases, the temperature of inert gases was set to 100 °C to match the steam temperature. The temperature of the fuel and assisting fluids were monitored at the burner exit plane.

The concentrations of CO_2 , CO , and unburned hydrocarbons (HC) in the combustion products, such as CH_4 , C_2H_6 , and C_3H_8 , were collected in sampling bags and later measured using a gas chromatograph. The extracted products were also fed into an NO_x analyzer and a photoacoustic extinctionsmeter (PAX) for BC mass concentrations. The NO_x ($\text{NO} + \text{NO}_2$) concentration was measured with an uncertainty of 1% of the reading value. The PAX used a laser with 870 nm wavelength; thus, a black carbon mass absorption cross-section of $4.74 \text{ m}^2/\text{g}$ was used (Bond and Bergstrom, 2006) to convert the absorption measurement to the equivalent black carbon mass concentration.

A carbon mass balance analysis was employed to calculate CCE for each test case (Corbin and Johnson, 2014). The CCE was defined as the ratio of the mass of carbon in the form of CO_2 produced in the course of combustion to the mass of carbon within the fuel stream:

$$\text{CCE} = \frac{\dot{m}_{\text{C,P}}}{\dot{m}_{\text{C,F}}} \quad (2.2)$$

the details of this calculation can be found in (Corbin and Johnson, 2014; Ahsan et al., 2019). In each experiment, the assisting fluid flow rate was increased from zero to a point where flame blow-off was triggered. The assisting fluid-to-fuel mass flow ratio (MFR) where the CCE collapsed ($\text{CCE} \approx 96.5\%$) was estimated by a polynomial fit to the data in that region and reported in Table 2.1.

The uncertainty associated with CCE and species EIs was calculated by propagating the bias and precision uncertainties originating from the instruments assuming independent measured quantities (Corbin and Johnson, 2014). These calculations resulted in average uncertainties of $\pm 21 \times 10^{-3} \text{ g}/(\text{kg-fuel})$ and $\pm 13 \times 10^{-3} \text{ g}/(\text{kg-fuel})$ in EI_{NO_x} , and $\pm 0.7 \times 10^{-3} \text{ g}/(\text{kg-fuel})$ and $\pm 0.5 \times 10^{-3} \text{ g}/(\text{kg-fuel})$ in EI_{BC} for air- and steam-assisted cases, respectively, at the collapse MFR.

The discussion of the results presented will be based on the physicochemical and qualitative radiation effects on characteristic peak temperatures, the extent of the high-temperature region (*i.e.*, flame zone), turbulence characteristics and residence time, scalar dissipation rate (SDR), and their effects on BC and NO_x emissions. It is worth mentioning that the light-absorbing fraction of soot is measured, referred to as "black carbon (BC)".

2.3 Results and Discussion

2.3.1 Visual Observations

Figure 2.2 shows three flame images for selected air- and steam-assisted cases, *i.e.*, zero MFR, an intermediate MFR value, as well as an MFR close to the CCE collapse point. At zero co-flow, the flames had their highest luminosity. By increasing the as-

sisting fluid flow rate, there was an overall reduction in luminosity, where air-assisted flames transitioned to be bluer, and the steam-assisted flames shifted to be redder. The former originates from increased visibility of the chemiluminescence emission of chemically excited CH radicals due to the reduced soot formation and radiation.

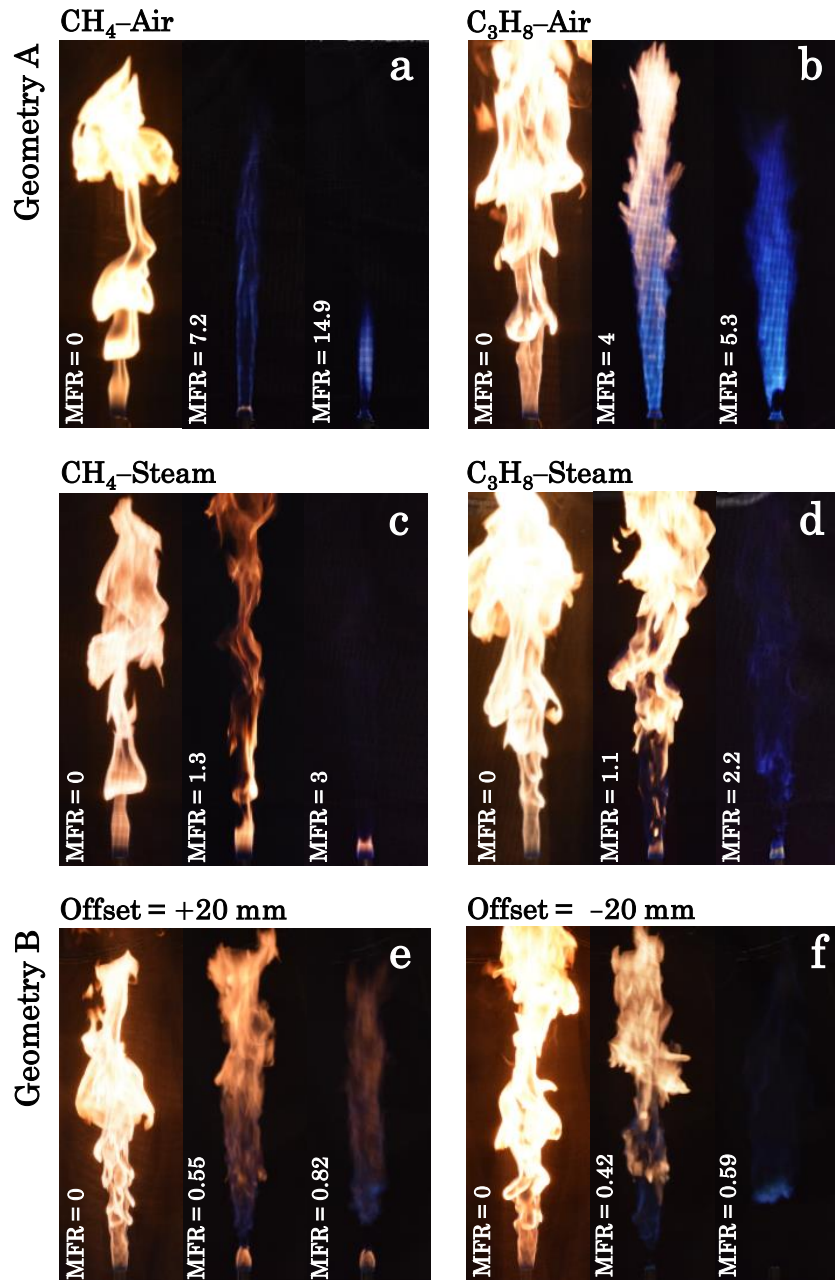


Figure 2.2: Flame images for selected air- and steam-assisted cases.

This chemiluminescence emission peaks at around 431 nm, and is responsible for the blue color of these flames (Walsh et al., 1998; Karnani and Dunn-Rankin, 2013). While soot emission is broadband and interferes with CH chemiluminescence observations, it was shown that the application of filtering methods is effective for visualization of a residual luminosity in subtracted flame images (Karnani and Dunn-Rankin, 2013). In contrast, the latter resulted from a reduction in soot formation and temperature by steam addition. It should be noted that the luminosity relates to the temperature and surface area of the soot particles, which is not necessarily associated with the measured values due to high-temperature soot oxidation immediately downstream of the flame.

In air-assisted flames (Figs. 2.2a and 2.2b), the flame height decreased by increasing the air flow rate due to an increased fuel-air mixing leading to a stoichiometric air-to-fuel ratio in a shorter time. On the other hand, in steam-assisted flames (Figs. 2.2c–f), there was no significant change in flame height by increasing the steam flow rate before the CCE collapse point. Furthermore, in air-assisted flames, two diffusion flame layers formed around the annular fuel stream; one outer diffusion flame between the fuel stream and the ambient air, and one inner diffusion flame between the fuel stream and the co-flow air stream (these two flames are easily identifiable at low flow rates of assisting air, but with increasing air flow, the inner diffusion flame becomes indistinguishable from the outer flame). In other words, in air-assisted cases, the outer flame surface area was generally smaller compared to steam-assisted cases and compared to the unassisted flames. The extent of the high-temperature zone is important in the interpretation of NO_x formation as well as soot formation and consumption.

Irrespective of assisting fluid, at some critical MFR, the main flame lifted off. Further increases in MFR blew off the upper flame, usually leaving a small rim-

stabilized flame in the shear-mixing layer located between the annular fuel stream and the ambient air. In the case where the exit plane of steam co-flow was recessed inside the outer tube (Fig. 2.2f), and steam premixed with the fuel, the rim flame also blew off.

The flame’s stability appeared to rest on maintaining a flame in the shear-mixing layer near the burner exit. Without assisting fluid, the strength of this shear-mixing layer in terms of the scalar dissipation rate and mean upward velocity field was a result of the momentum of the fuel stream (*i.e.*, its exit velocity and density), while the flame’s ability to remain at that location depended on its composition as characterized by a laminar flame speed. These processes occurring in the shear-mixing layer near the burner exit were altered (either augmented or impaired) by the momentum and composition of the co-flow and its proximity to the initial outer shear layer (*i.e.*, the burner flow geometry). For example, fuel flow rates with a higher exit momentum (either created by a higher exit velocity or density) required less momentum from the assisting fluid to blow off, especially if the assisting flow was introduced nearer to the outer shear-mixing layer or allowed to premix its momentum with the fuel stream before the exit plane.

2.3.2 Geometry A: Carbon Conversion Efficiency and Emission Indices

Figure 2.3 shows the CCE (first row), EIs for BC (second row) and NO_x (third row) for Geometry A. The first column explores the effect of fuel type, fuel flow rate, and either air or steam as the assisting fluid, as well as two data sets from Geometry B to provide a comparison with those experiments. The second and third columns investigate the effects of changing the concentration of O_2 and steam in the EqvAir and EqvSteam mixtures, respectively. The CCE and NO_x data all have the same independent axis (MFR from 0 to 20), while this axis for the BC was expanded

Table 2.2: Uncertainty analysis of CCE, EI_{NO_x} , and EI_{BC} for Geometry A. The uncertainty range is given over the MFR values. Base cases are shaded.

Exp. ID	CCE - uncertainty range (%)	EI_{NO_x} - uncertainty range (%)	EI_{BC} - uncertainty range (%)
Geometry A			
CH ₄ -Air	3.4 – 5.9	2.9 – 14.7	7.6 – 9.9
Different fuel			
C ₃ H ₈ -Air	1.1 – 1.2	1.6 – 2.1	2.7 – 3.4
Higher flow rate			
CH ₄ -Air-HFR	1.5 – 2.7	1.4 – 3.8	4.9 – 10.7
Equivalent air assist			
CH ₄ -EqvAir-1	3.3 – 6	2.9 – 13.9	7.6 – 9.3
CH ₄ -EqvAir-2	3.4 – 6.1	2.9 – 14.3	8 – 10
CH ₄ -EqvAir-3	3.8 – 5.7	2.8 – 3.5	7.5 – 8.9
CH ₄ -Steam	3.3 – 5.5	2.9 – 13.1	9.7 – 13.4
Different fuel			
C ₃ H ₈ -Steam	0.9 – 1.8	1.6 – 7.3	2.8 – 6.4
Higher flow rate			
CH ₄ -Steam-HFR	1.6 – 2.7	1.4 – 13.6	4.2 – 10.6
Equivalent steam assist			
CH ₄ -EqvSteam-1	3.2 – 5.4	2.8 – 10.6	9.1 – 14.9
CH ₄ -EqvSteam-2	3.1 – 5.4	2.9 – 14	10.4 – 11.7

(MFR from 0 to 6) to provide greater resolution since the PAX readings at higher MFR were indistinguishable from background particulate concentrations. Since the changes in EI_{BC} occurred over a different range of MFRs than the changes in NO_x and CCE, there is an inferred separation in the physical processes associated with these changes.

The details of the uncertainty analysis for CCE, EI_{NO_x} , and EI_{BC} for Geometry A are presented in Table 2.2, where the ranges of uncertainty values are given. The lower uncertainties are attributed to unassisted flames or assisted flames at lower MFR values, while the higher uncertainties are calculated at the highest MFR values, where EI_{NO_x} and EI_{BC} are very low. Similar uncertainty values were calculated for Geometry B, which is not shown in Table 2.2 for brevity. Please refer to Table 2.1 for the details of each experiment.

In considering the CCE data, the first goal is to identify patterns in the experimental CCE collapse data before discussing the details of emissions of BC and NO_x .

As illustrated in Figs. 2.3a, 2.3d, and 2.3g, at zero co-flow, the CCE was essentially 100 % and remained at that value by increasing assisting fluid flow rate until a critical amount when the CCE collapsed. In CH₄ flames, the drop in CCE was highly correlated with the increase in CH₄ emission, with 100 % of the HC emissions being methane, while in C₃H₈ flames, more than 99 % of the HC emissions were propane, and the rest were ethane and methane. Collectively, this showed that fuel stripping without combustion was the main contributor to inefficiency.

Irrespective of fuel type, the CCE collapse occurred at a significantly lower MFR for steam, *i.e.*, the CCE collapse required more air than steam. For the case of air, the collapse point MFR was 5 and 2.5 times greater compared to steam cases for 20 SLPM of CH₄ and C₃H₈ flames, respectively. From a combustion perspective, the apparent difference between air and steam is that air is composed of 21 % O₂ (having the potential to support high-temperature robust combustion) and N₂ (reducing the characteristic flame temperature), while steam is primarily a diluent.

Evidence of the role these different assisting fluids play is seen most clearly in Fig. 2.3c where the EI_{NO_x} can be used through a thermal NO_x model as an indicator of maximum characteristic flame temperature and a surrogate for the robustness of combustion (with respect to blow-off) for interpreting the CCE collapse point. For all air-assisted flames, the EI_{NO_x} remained constant as more air was added, which suggests that the assisting air was participating in combustion and that the maximum characteristic flame temperature was almost constant. The EI_{NO_x} only dropped when the CCE started to drop, and less fuel was burned. Figure 2.3f, which presents the results for EqvAir flames, solidifies this point of characteristic flame temperature and the role of the co-flow in combustion, and how the added or reduced O₂ affects the EI_{NO_x} and CCE. As shown in the figure, the addition or reduction of O₂ in the co-flow also enhanced or impaired the robustness of combustion, respectively, with respect to

blow-off. As illustrated in Fig. 2.3d, the MFR at the CCE collapse point was almost linearly proportional to the O₂ concentration in the co-flow.

The EI_{NO_x} for steam-assisted flames dropped an order of magnitude while the CCE remained near 100 %. It is essential to recognize that steam may not be strictly inert and could play a chemical role in the emission of NO_x and soot. To examine the relative magnitudes of these chemical and thermal effects, Fig. 2.3i presents the results for the EqvSteam flames. There was mainly no difference between a co-flow of steam and 50 % steam, while the 0 % steam case required more co-flow to both reduce the EI_{NO_x} and bring about the CCE collapse. While suggesting that this difference may be chemical, it is worth pointing out the changing c_{pas} (see Table 2.1), which would suggest that steam suppressed the maximum characteristic flame temperature more than the 0 % EqvSteam. An interesting comparison can be made between the 0 % O₂ EqvAir and 0 % steam EqvSteam, which had the MFR of the CCE collapse at 7.7 and 4.1, respectively. While their characteristic maximum flame temperatures due to dilution were consistent with the CCE collapse point, their different densities and momentum fluxes opened up the possibility of hydrodynamic effects in determining the flame blow-off.

Hence, as shown in Eq. 2.1, this CCE collapse observation could potentially be related to the hydrodynamics of the fuel and/or co-flow, and/or the buoyancy of the products of combustion. Focusing on the fuels' molecular weights, densities, and momentum fluxes (*i.e.*, the first term in the denominator of Eq. 2.1), equal volumetric flow rates result in C₃H₈ having a momentum flux 175 % higher than CH₄. If the CCE collapse were related to the total momentum flux (*i.e.*, the denominator of Eq. 2.1), which is synonymous with a total upward force, then as observed, the assisting flow for C₃H₈ would not be required to provide as much momentum flux for the CCE collapse as for CH₄.

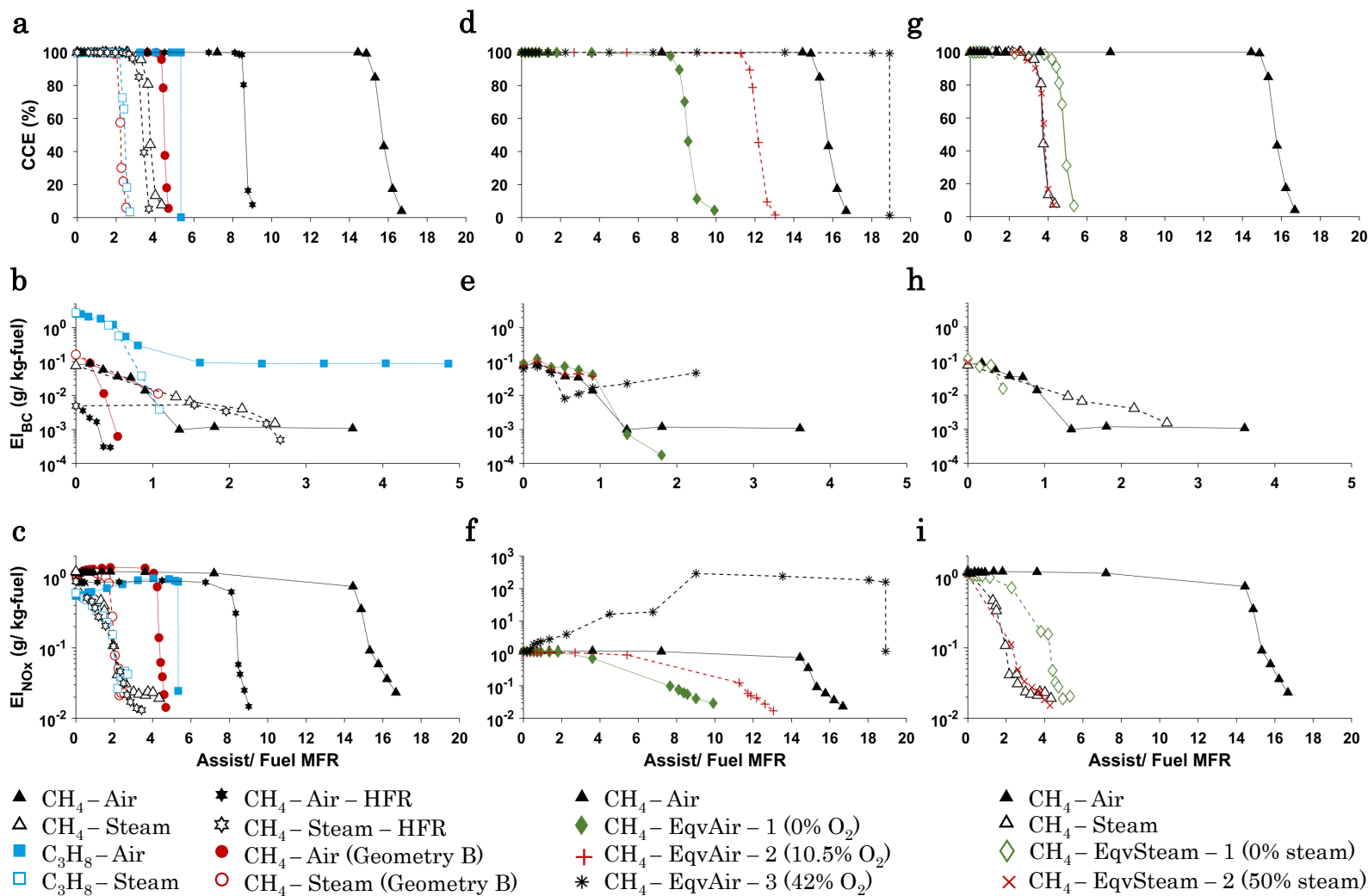


Figure 2.3: CCE (first row), EI_{BC} (second row), and EI_{NO_x} (third row) for Geometry A (lines drawn only to help visually connect data sets). The x-axes show Assist/Fuel MFR.

An alternative hydrodynamic perspective for this same observation could be related to the upward buoyancy force of the products (*i.e.*, the numerator of Eq. 2.1) of an equal volume of C_3H_8 fuel compared to CH_4 . Since more air is needed for C_3H_8 combustion, it produces 125 % more volume of products (and upward buoyant force) as similar temperature CH_4 flames. As a result, again C_3H_8 would require less upward assisting momentum to create the same effect. It is, therefore, worth considering the CCE collapse for other conditions, such as higher fuel flow rate or different geometry, to see if any inconsistencies emerge. For the higher flow rate CH_4 flames, the upward momentum flux of the CH_4 is quadrupled, while the upward buoyant force is doubled. The upward momentum flux of the assisting air at the CCE collapse for the higher flow rate was 0.57 of the base case, while that for the assisting steam was 0.9, which remains consistent with either hydrodynamic perspectives described above.

Keeping the upward buoyant force constant, while changing the momentum fluxes, results from Geometry B were added to Fig. 2.3a. By making the inner tube smaller (Geometry B), the momentum flux of CH_4 in the annular flow was reduced to 0.9 of Geometry A. For the case of air-assisted flames, the momentum flux of Geometry B at the CCE collapse point was approximately 50 % of the Geometry A, while for steam that value was approximately 300 %, thereby highlighting the differences between an oxidizing and a diluting assisting co-flow. While still unresolved, these results indicate that a possible mechanism of CCE collapse (or blow-off) is related to the events occurring at the outer shear layer. It is important to recognize that these layers can be formed under the influence of turbulence in the fuel flow, and the SDR is also affected by the bulk velocity gradient. It is, therefore, hard to understand the underlying cause of blow-off, and this point is revisited in the discussion about Geometry B.

Figure 2.3b shows the variations of EI_{BC} versus MFR for Geometry A, where, at

zero MFR, the flames had their highest EI_{BC} equal to 0.08 and 2.6 g/kg-fuel for CH_4 and C_3H_8 , respectively. In general, BC emissions were greatly reduced with a small amount of air or steam co-flow (notably smaller than the MFR at the CCE collapse point). As illustrated in Fig. 2.3b, introducing only a small amount of steam co-flow in C_3H_8 flame significantly decreased the BC emission (note the log-scale) indicating that steam had a notably higher BC suppression capacity compared to air in C_3H_8 flames; whereas, air and steam had almost the same BC suppression capacity in CH_4 flames. To interpret these results, chemical effects, temperature effects caused by dilution with the co-flow, and the radiation heat loss of flames, as well as the extent of the high-temperature region, *i.e.*, the existence of one or two diffusion flame layers formed around the annular fuel stream (one inner diffusion flame between the fuel stream and the co-flow air stream, and one outer diffusion flame between the fuel stream and the ambient air), need to be considered.

Steam addition affects soot formation through temperature and chemical effects. In C_3H_8 flames with steam co-flow, the temperature effect was less pronounced due to counterbalancing processes. The steam co-flow, concurrently, lowered the product characteristic temperature due to dilution while reducing the radiation (see Fig. 2.2d) leading to less energy loss by the flame, *i.e.*, an increase in net temperature. Meanwhile, the added source of H and OH radicals by steam addition reduced BC formation through the reaction of OH radicals with carbon particles and CO (water-gas shift reaction) (Castiñeira and Edgar, 2006) leading to a significant decrease in BC emissions (as illustrated in Fig. 2.3b). However, in C_3H_8 flames with air co-flow, the characteristic flame temperature was closer to T_{ad} due to a lower radiation heat loss; hence, the oxidation of carbon particles was enhanced, which reduced BC emissions.

In CH_4 flames with steam co-flow, the characteristic flame temperature was reduced due to dilution without radiation losses being strongly affected, as in general,

the radiation losses are much smaller in CH_4 flames. Therefore, the competing temperature and chemical effects explain the significant change in EI_{BC} reduction slope in C_3H_8 compared to CH_4 with steam co-flow. In CH_4 flames with air co-flow, the trends of EI_{BC} reduction was similar to that of C_3H_8 flames with air co-flow.

The EI_{BC} for higher fuel flow rate cases was an order of magnitude lower (0.005 g/kg-fuel) compared to the base case (0.08 g/kg-fuel). The higher fuel flow rate likely affected soot formation in complex ways; both the upward buoyancy and momentum forces will be higher, which strengthened the outer turbulent shear-mixing layer, increased fuel Re , and decreased the characteristic length scales (and time scales) of the flame for soot formation to occur before entraining more O_2 . Higher fuel-air mixing at the smaller length scales enhanced the ambient air entrainment and decreased the characteristic post-flame temperature, having counteracting effects on soot formation. While the former tended to decrease soot emissions through better fuel-air mixing, the latter had the potential for more agglomerated carbon particles as soot. However, the results show that the former dominated, leading to lower overall soot emissions.

At higher fuel flow rate CH_4 flames (Fig. 2.3b), a slight increase in MFR both for air and steam decreased the EI_{BC} , with a higher BC suppression capacity of air compared to steam. As illustrated in Fig. 2.3b, by adding assisting co-flow in CH_4 flames, the higher characteristic flame temperature due to a lower radiation heat loss in air-assisted flames were more effective in reducing BC emissions compared to the steam-assisted flames, where the lower characteristic flame temperature due to dilution and chemistry had competing effects on BC emissions. These results also showed that the effectiveness of air or steam assisting co-flow in reducing BC emissions in CH_4 flames is likely to be dependent on fuel flow rate, geometry, and overall hydrodynamics of fuel and the assisting co-flow.

In CH_4 and C_3H_8 flames with no assisting fluid, the EI_{NO_x} (Fig. 2.3c) equaled 1.15 and 0.54 g/kg-fuel, respectively, was consistent with the lower characteristic product gas temperatures of C_3H_8 flames due to a higher radiation heat loss. The NO_x emissions (assumed to be thermal NO_x) is mainly controlled by the flame temperature and the extent of the high-temperature region, *i.e.*, flame zone. In both CH_4 and C_3H_8 flames, by adding more air, NO_x emissions increased slightly due to a reduction in flame luminosity, which reduced the radiation heat loss, and led to a higher characteristic temperature compared to the unassisted cases. The increase in NO_x emissions was more considerable in C_3H_8 compared to CH_4 flames due to the suppression of a larger amount of BC in C_3H_8 flames by adding the air co-flow as in Fig. 2.3b; hence, leading to a more significant increase in characteristic flame temperature. However, this increase continued to a point, close to the CCE collapse, at which EI_{NO_x} eventually decreased due to less fuel being burned.

In steam co-flow cases, EI_{NO_x} decreased continuously with increasing co-flow, due to steam acting as a thermal energy sink, and the NO_x emissions reached values close to zero prior to the CCE collapse. The steam Re at the exit of the inner tube was significantly larger compared to air, due to a lower viscosity, while having higher c_p . Therefore, in steam co-flow cases, higher turbulence at the exit of the tube promoted mixing of the fuel with the co-flow, which at the same time had higher c_p , resulting in lower temperatures and a high NO_x suppression capacity. While in C_3H_8 flames, steam addition had a counterbalancing effect on characteristic flame temperature, *i.e.*, reducing the temperature due to dilution while increasing it due to lower radiation heat loss, Fig. 2.3c illustrated that the characteristic flame temperature was, indeed, reduced by steam addition leading to lower NO_x emissions, and the dilution effect was more pronounced than radiation effects. Note that the NO_x suppression capacity of the steam co-flow was similar for CH_4 and C_3H_8 flames, unlike the air co-flow cases.

The results in Figs. 2.3b and 2.3c also illustrated that, in CH_4 and C_3H_8 flames with steam co-flow, chemical effects played a significant role in reducing BC formation while the characteristic flame temperature decreased compared to unassisted flames.

For all cases, except the O_2 -enriched case, the EI_{NO_x} (Fig. 2.3f) remained almost constant with increasing the co-flow and decreased prior to the CCE collapse in correlation with the reduction of the characteristic flame temperature by increasing the assisting co-flow flow rate. However, EI_{NO_x} increased with increasing the assisting co-flow in the O_2 -enriched case and reached the value of 289 g/kg-fuel at an MFR equal to 9, due to less diluting inert gases leading to a higher characteristic flame temperature. Note that c_p is almost constant in these assisting co-flows.

2.3.3 Geometry B: Carbon Conversion Efficiency and Emission Indices

In Geometry B, the diameter of the inner tube was reduced by half, which, for the same flow rates, lowered the momentum flux and Re of the fuel and increased the momentum flux and Re of the co-flow. In each experiment, similar to Geometry A, MFR was increased, keeping the fuel flow rate constant (20 SLPM). Black carbon emissions were not measured in these cases. The first row of Fig. 2.4 focuses on exploring the effect of fuel and assisting fluid type in Geometry B. The second and third rows Investigate the effects of fuel dilution and various offset heights of the assisting fluid with respect to the fuel exit plane, respectively.

Comparing plots in Figs. 2.3 and 2.4 shows that the CCE collapse was significantly earlier for both air- and steam-assisted CH_4 and C_3H_8 flames in Geometry B. For air co-flow, the MFR for the CH_4 collapse point equaled 15 and 4.3, for Geometry A and B, respectively, while for C_3H_8 these numbers are 5.3 and 1.4. Similarly, for steam co-flow, the MFR for the CH_4 collapse point equaled 3.2 and 2, for Geometry A and B, respectively, while for C_3H_8 these numbers are 2.2 and 0.74. The reasons

for these dramatic changes involves revisiting the different perspectives for CCE collapse (*i.e.*, blow-off) discussed in Geometry A, which was the bulk hydrodynamics (*i.e.*, the different streams contributing to upward momentum and buoyancy, Eq. 2.1). By keeping \dot{m}_f the same, the buoyancy was unchanged while the fuels' characteristic velocities and momentums were reduced by 25 %, while for the same MFR the characteristic momentum of the assisting fluid were 450 % higher. From a bulk momentum perspective, it was not unexpected that the CCE collapse occurred at lower MFRs. This higher-momentum assisting flow simultaneously affects the strength of the inner mixing layer. The location of Geometry B's inner mixing layer was initially 3.2 mm further away from the outer mixing layer, where the onset of blow-off was observed. Without detailed fluid velocity measurements in this region, it remains speculative

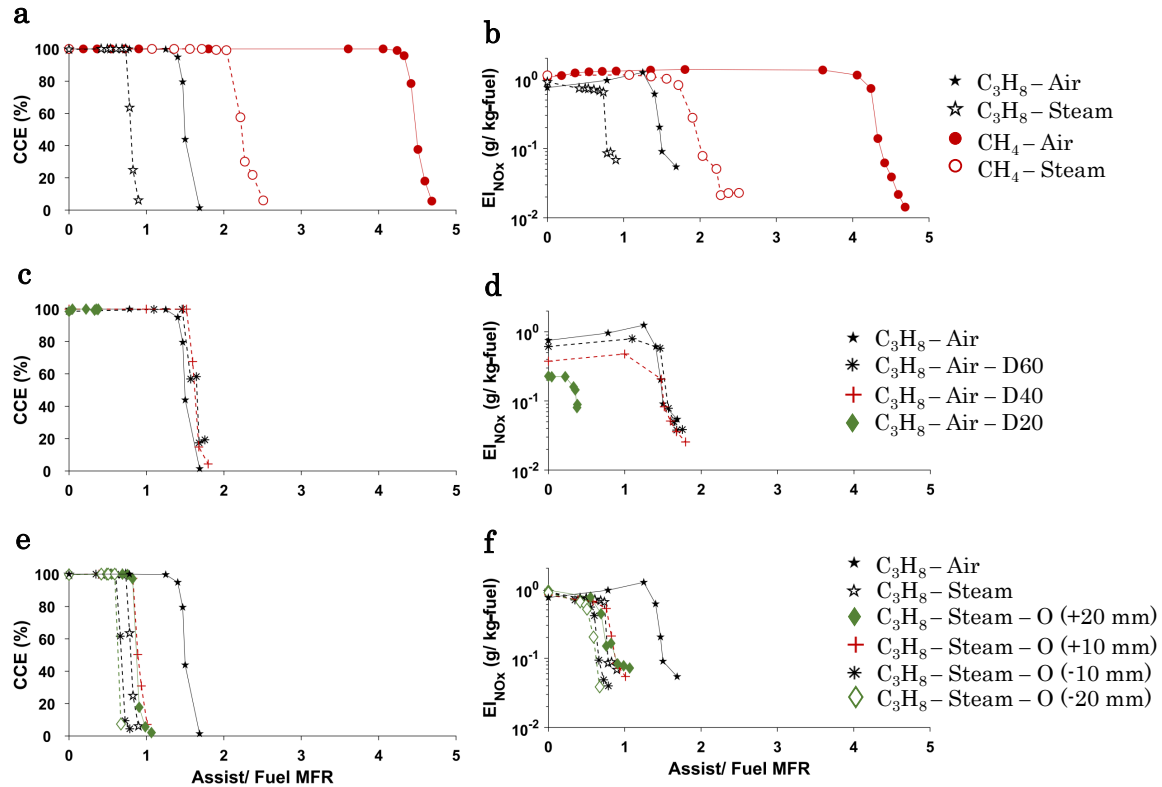


Figure 2.4: CCE (left column) and EI_{NO_x} (right column) for Geometry B (lines drawn only to help visually connect data sets). The x -axes show Assist/Fuel MFR.

as to the underlying cause and hence the correlating quantity associated with CCE collapse, which will be addressed in Investigation III.

While NO_x emissions were slightly higher in CH_4 compared to C_3H_8 flames (Fig. 2.4b) due to a higher radiation heat loss in C_3H_8 flames, all flames emitted an order of magnitude lower NO_x prior to the CCE collapse. In air co-flow flames, similar to Geometry A, EI_{NO_x} increased slightly by adding more air; while in steam cases, it decreased continuously with increasing the co-flow, which was more pronounced in the C_3H_8 flame with steam co-flow. However, unlike in Geometry A, the NO_x suppression capacity of steam was significantly higher in the C_3H_8 flame compared to the CH_4 flame in Geometry B, and EI_{NO_x} was considerably smaller in the C_3H_8 flame as the co-flow was increased. In other words, the mass flow rate of steam required to reduce the NO_x formation in C_3H_8 flame in Geometry B was smaller compared to Geometry A while in CH_4 flames almost the same flow rate of steam was required to suppress NO_x .

In Geometry B, flames with air co-flow were also tested using C_3H_8 diluted by N_2 to get volumetric LHVs (MJ/m^3) equal to 60 %, 40 %, and 20 % of pure C_3H_8 . The CCE results in Fig. 2.4c show that the flames collapsed at approximately the same MFR while N_2 dilution slightly retarded the CCE collapse, due to the reduced momentum and density of the fuel stream leading to lower fuel Re . In the highly diluted case (80 % N_2 by volume), the flame blew off abruptly without any transition in its CCE.

As illustrated in Fig. 2.4d, EI_{NO_x} increased with increasing the LHV of the fuel mixture, due to a higher flame temperature and at zero co-flow, EI_{NO_x} equaled 0.75, 0.61, 0.38, and 0.23 g/kg-fuel for the volumetric LHVs equal to 100 %, 60 %, 40 %, and 20 % of C_3H_8 , respectively. For all cases, EI_{NO_x} increased slightly by adding more air, reached its maximum, and dropped an order of magnitude before the CCE collapse.

The CCE and EI_{NO_x} results for various offset heights of ± 20 mm and ± 10 mm are shown in Figs. 2.4e and 2.4f. In these experiments, steam-assisted C_3H_8 flames were used. The CCE collapse occurred at lower MFR for negative offset cases compared to zero offset and positive offset cases. This is presumably due to the premixing of the fuel and the co-flow streams and the enhanced cooling of the flame nearer to the burner exit when the co-flow was increased. The MFR at the collapse point equaled to 0.60, 0.62, 0.74, 0.83, and 0.83 for the offsets equal to -20 mm, -10 mm, 0 mm, $+10$ mm, and $+20$ mm, respectively, and the effects of changing the offset diminished in either the positive or negative direction.

The zero steam flow rate corresponded to the highest NO_x emission with EI_{NO_x} in the range of 0.82 to 0.97g/kg-fuel, which was suppressed by adding a small amount of steam, as shown in Fig. 2.4f. Furthermore, Fig. 2.4f illustrates that negative offsets decreased the NO_x emission at lower MFRs due to premixing before the combustion zone, and lower characteristic flame temperature.

2.4 Concluding Remarks

Motivated by air- and steam-assisted flares, the CCE, EI_{BC} , and EI_{NO_x} were studied experimentally on lab-scale co-flow burners to understand the effects of burner geometry, composition and flow rates of the flared gas and assisting fluids. In total, 22 cases were considered where the assisting flow was initially zero and subsequently incrementally increased until the flame blew off. It is noteworthy that geometry and scale play important roles in BC and NO_x emissions, so care should be taken in extending the results of this study to full-scale industrial applications.

In this study, all the CCE and EI results were presented in terms of the assisting fluid-to-fuel MFR. This choice of an independent variable did not provide a general and consistent correlation for any subset of the 22 cases. It is worth noting that other

dimensionless quantities associated with the overall hydrodynamics calculated based on the average quantities at the exit plane of each stream, such as ratios of momentum, velocity, and momentum-to-buoyancy, did not reveal any reliable correlation.

For all cases, other than a very low LHV case (*i.e.*, fuel stream of 20 % C₃H₈ and 80 % N₂), there was a large MFR disconnect between the early onset of BC suppression and the collapse of CCE associated with flame blow off. As a result, there was a broad range of assisting fluid flow rates, where the CCE was almost 100 %, while the flame luminosity and BC emissions were monotonically and eventually highly suppressed with increasing assisting fluid flow rates. The diminished flame luminosity was associated with the flames becoming bluer for air-assisted flames and redder for steam-assisted flames, while the EI_{BC} was reduced by at least an order of magnitude with an MFR of 1.5.

All settings of manipulable variables that were expected to result in a higher characteristic flame temperature, namely, introducing more oxygen in the assisting fluid, adding less steam or other diluents with lower specific heat capacities, and having less radiation heat loss, increased the NO_x production. Therefore, it was concluded that a thermal mechanism consistently explained the EI_{NO_x} results.

In all comparable cases, the CCE collapse required considerably more mass of air compared to that of steam for it to occur. This observation was associated with the notion that the mixing of oxygen, as opposed to diluents, into the fuel stream increased the robustness of combustion. A qualitative pattern was identified as being associated with the outer shear-mixing layer that existed between the co-annular fuel stream and the ambient air.

CHAPTER 3

Investigation II: Jet Diffusion Flame in a Co-annular Burner at Low Range of Co-flow¹

3.1 Introduction

The combustion of waste hydrocarbons or unwanted gases from refineries, oil wells, and petrochemical industries in an open flame is known as flaring. (Schnelle Jr et al., 2015). This process can emit a variety of pollutants, including unburned hydrocarbons, carbon monoxide (CO), oxides of nitrogen (NO_x), and soot, that is mainly made up of black carbon (Baukal Jr, 2013). These pollutants (or even the products of their atmospheric reactions) are known to have an adverse effect on human health and climate (Landrigan et al., 2018). Black carbon (BC) is of particular rele-

¹Based on a published paper: Bello, O. W., **Zamani, M.**, Abbasi-Atibeh, E., Kostiuk, L. W., and Olfert, J. S. (2021). Comparison of emissions from steam-and water-assisted lab-scale flames. *Fuel*, 302, 121107.

vance since it is thought to have a significant impact on climate change (second only to carbon dioxide), particularly in the Arctic (Bond et al., 2013; Ramanathan and Carmichael, 2008). Due to its direct absorption of sunlight, BC produced by gas flaring that is deposited on snow and ice surfaces decreases surface albedo (Stohl et al., 2013). According to the United States Environmental Protection Agency, NO_x emissions are part of a class of dangerous and highly reactive chemicals that contribute to ground-level ozone production, which can harm ecosystems, living creatures, and plants (Ahsan et al., 2019; Baukal, 2005). Additionally, flaring produces a significant quantity of unsteady radiative heat and noise that is harmful to people who reside close to flaring facilities (Leary et al., 2002).

Concerns regarding environmental protection have been increasing in recent years, necessitating lower emissions from gas flaring. Flaring is strictly regulate in the majority of oil-producing and developed countries (GGFRI, 2004; AER, 2016; Aye and Wingate, 2019). Many US State regulations, in particular, require *smokeless* combustion (defined as a plume opacity of less than 20%) for the majority of the time a flare is used in pressure-relief applications at refineries and petrochemical facilities (API, 2014). As a result, the oil and gas and petrochemical industries have made efforts to reduce soot emissions, which is now one of the primary factors considered in flare design for refineries and petrochemical sites (Schnelle Jr et al., 2015; Baukal Jr, 2013). Soot emissions are typically reduced by using *assisted flares*, in which air (discussed in Chapter 2), steam, or liquid water are added into the combustion zone of the flare (API, 2014; McDaniel and Tichenor, 1983; Castiñeira and Edgar, 2006). For steam-assisted flares, steam is introduced into the flare through a manifold placed around the edge of the flare tip, a single pipe nozzle positioned in the middle of the flare, or a series of steam injectors (API, 2014). Water-assisted flares inject an atomized water spray into the flare’s combustion zone using several nozzles

attached to the flare tip (Leary et al., 2002; Hinvest, 1964). This type of assisting fluid is rarely used and is most likely to be used on horizontal flare applications and in situations where excess wastewater or brine must be eliminated (API, 2014). Although assisted flares typically reduce emissions, studies have shown that oversteaming (McDaniel and Tichenor, 1983) or over-watering (Hinvest, 1964) the flare can reduce flare combustion efficiency or extinguish the flare, resulting in high unburnt hydrocarbon or aldehyde emissions and poor destruction efficiencies (Ahsan et al., 2019; Leary et al., 2002; API, 2014; Hinvest, 1964).

The effects of steam- or water-assist on the production of NO_x and soot emissions in flames have been categorized into three mechanisms: chemical (Castiñeira and Edgar, 2006; Dryer, 1977; Zhao et al., 2002; Zamani et al., 2021), hydrodynamic (Castiñeira and Edgar, 2006; Dryer, 1977), and thermodynamic (Leary et al., 2002; Castiñeira and Edgar, 2006; Zamani et al., 2021; Glaude et al., 2010; Müller and Wittig, 1994). Through chemical mechanism, radicals play a significant role in flame chemistry, and the introduction of an assisting fluid can change the concentration of radicals in the flame, which can change soot formation pathways. Atomic hydrogen (H), atomic oxygen (O), hydroxyl radical (OH), methylene radical (CH), and methyl radical (CH_3) are the major radicals found in hydrocarbon flames. According to the available data, increasing water addition raises the concentration of hydroxyl radicals (Dryer, 1977; Roberts et al., 2005), while decreasing the concentration of nitrogen radicals (Zhao et al., 2002). The former reduces soot formation, whereas the latter prevents the production of NO_x (Dryer, 1977; Serrano et al., 2019; Anufriev and Kopyev, 2019). The changes to flame chemistry that occur when water is introduced have, however, been explained in two different ways. First, when water vapour reacts with carbon molecules, the excess radicals trigger reactions that produce CO, CO_2 , and H_2 (API, 2014; Castiñeira and Edgar, 2006). Second, when water molecules are

present, polymerization and the creation of long-chained oxygenated compounds that burn at a slower rate are inhibited (Castiñeira and Edgar, 2006).

Through the hydrodynamic mechanism, assisting fluid suppresses soot emissions by enhancing flare gas mixing with oxygen and increasing the turbulence in the flame (Devesh Singh et al., 2014).

Through the thermodynamic mechanism, the presence of water vapour in the flare lowers the peak temperature, resulting in a reduction of polymerization, thermal cracking, and NO_x formation (Castiñeira and Edgar, 2006; Dryer, 1977).

There have been few research on assisted flares, despite the fact that soot reduction caused by the injection of water or steam has been extensively studied in other combustion systems (internal combustion engines (Dryer, 1977; Anufriev and Kopyev, 2019; Kohketsu et al., 1996), gas turbines (Zhao et al., 2002), and furnaces (Escudero et al., 2020)). In order to investigate the significance of flare performance characteristics, Devesh Singh et al. (2014) parametrically studied the effect of assisting steam and air on ethylene flares. They found that better mixing of fuel with steam and air resulted in more complete combustion and significantly decreased the formation of soot. In an experimental study, McDaniel and Tichenor (1983) continuously monitored flare emissions from steam- and air-assisted flares using a sample probe placed over the flare. They investigated nitrogen-diluted propylene fuels and came to the conclusion that when acceptable industrial operating procedures were followed, steam- and air-assisted flares had high combustion efficiency ($> 98\%$). When steam and air co-flows were added to natural gas flames, Ahsan et al. (2019) found that the emission indices for NO_x and BC have become much lower compared to those for unassisted flares. Additionally, they observed that there is a wide range of assisting fluid flow rates (steam or air), which leads to high combustion efficiency and low pollutant emissions. Zamani et al. (2021) examined the effects of multiple assisting

fluids, including air, steam, and inert mixtures with the same molecular mass as air or steam, and came to the conclusion that the production of NO_x was increased by any changes that resulted in a higher characteristic flame temperature, such as the addition of more oxygen, the reduction of steam or other diluents with lower specific heat capacities, or the reduction of radiation heat losses. Thus, the results of their NO_x emission indices were explained by the thermal mechanism. Additionally, they claimed that temperature and chemical factors have a role in how steam addition influences soot production. While adding steam to propane flames reduced radiation and lowered the characteristic product temperature due to dilution, the increase in NO_x emissions was used to infer a net temperature increase. Meanwhile, the addition of H and OH radicals decreased BC formation by inhibiting the reaction of OH radicals with carbon particles and CO through water-gas shift reaction (Castañeira and Edgar, 2006), leading to a considerable reduction in BC emissions. Furthermore, water injection into the flare was reported to lower noise and radiation levels by Bussman and Knott (2000) and Leary et al. (2002).

The authors are not aware of any studies published in the literature that looked into how to reduce NO_x and soot emissions from flares using liquid, unheated water. Thus, this study was motivated to fill this gap. As a result, this experimental study aims to identify and compare the impact on NO_x and soot emissions of adding unheated liquid water droplets and steam to a turbulent diffusion flame with fuels of methane, propane, and a mixture of methane and propane. Since both steam and evaporated liquid water would have the same chemical impact on the flame, the significance of thermodynamic and hydrodynamic mechanisms would be the main topic of discussion when analyzing the obtained data. Additionally, according to the state of each assisting fluid, there is a substantial difference in the enthalpy of the flames. It is crucial to compare the two assisting fluids (steam or liquid water), as water-

assisted flares could potentially produce fewer greenhouse gases with lower operating expenses because steam cannot be produced from liquid water without energy.

3.2 Experimental Setup & Methodology

An overview of the steam-/ water-assisted flames experimental setup is schematically shown in Fig. 3.1 along with the measurement devices used. These experiments explored the effects of fuel composition and low flow rates of assisting fluid on BC and NO_x emissions. Two stainless-steel burners used in this study had an exit diameter of $D_i = 50.8$ mm, and had the same outer geometry as the burner costume-designed by Jefferson (Jefferson, 2017). The burner allowing for atomized water injection had a nebulizer placed inside a tube ($d_o = 25.4$ mm) with an offset of 25.4 mm below the exit plane of the burner, preventing the flame from damaging the vibrating membrane of the nebulizer. A geometrically similar burner was built to allow for steam injection through the 25.4-mm tube with the same downward offset.

The test matrix of the sets of experiments conducted is presented in Table 3.1, three types of fuels flowing through the annular space were used, namely, 100 % CH_4 , 90 % CH_4 and 10 % C_3H_8 , and 100 % C_3H_8 with the volumetric higher heating values (HHV_v) of 36.2, 41.6, and 90.2 MJ/m^3 , respectively, with the second one mimicking the average HHV_v of Alberta flared gas (Trivanovic et al., 2020). The fuel flow rate was fixed at 20 SLPM for all cases.

To atomize water, two nebulizers controlled by pulse width modulation were used, one generating 12 ± 3 μm droplets with a flow rate of 2 – 6 g/min and the other one generating 40 ± 3 μm droplets with a flow rate of 7 – 25 g/min. The water flow rate was steady within the whole range, except the low range of 40- μm nebulizer (7 – 10 g/min) which was unsteady with respect to time (*i.e.*, pulsating). The atomized water flow rate was measured by placing water-dispensing bottle, connected

to the nebulizer, on an electronic balance with data logging frequency of 2 Hz and a stopwatch. A drain line returned the extra water in the nebulizer back to the bottle. The atomized water flow rate uncertainty was less than 0.2% of the reading.

Steam was supplied by the same electric steam generator used in Investigation I, but, to supply low flow rates of steam, the steam line was divided into two lines by a tee. One line had a plug valve and a precision valve to control the low flow rates of steam to the burner through a 6 m heated line with a temperature set point of 150 °C. The other line carried the excess steam through an identical heated hose with a temperature set point of 115 °C and was directed to a heat exchanger to condense the steam; where that water flow rate was measured with the electronic balance and a stopwatch. The steam flow rate to the burner was determined to be the difference between the total flow rate out of the electric steam generator (measured by the cone

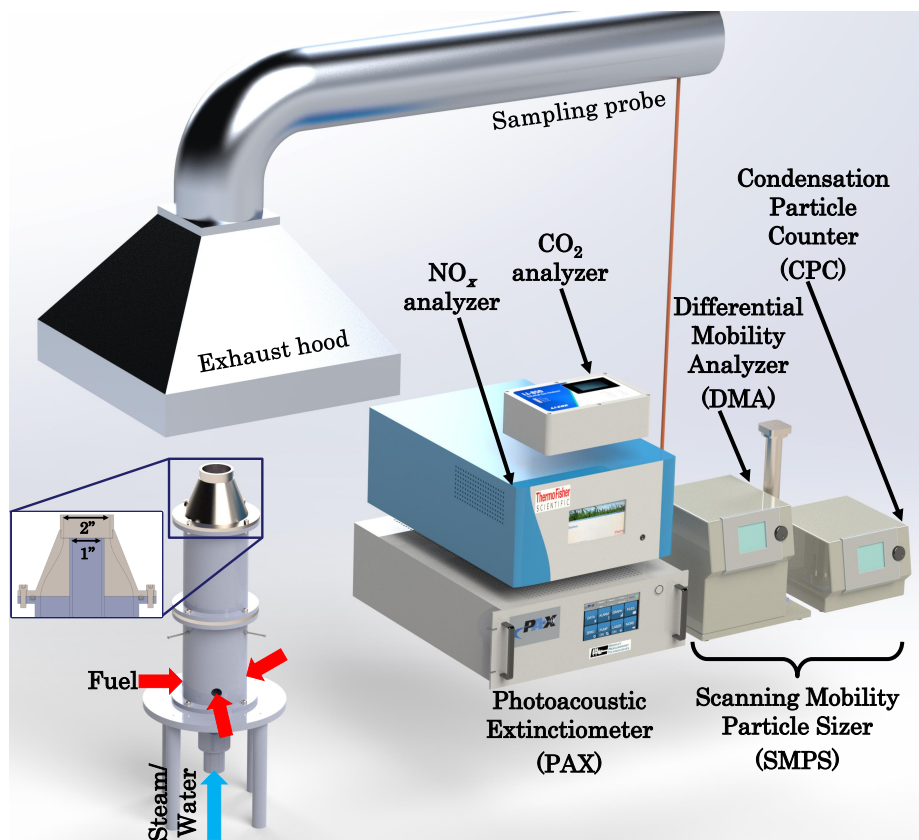


Figure 3.1: Schematic of the experimental setup in Investigation II.

Table 3.1: Experimental matrix of Investigation II; base cases are shaded.

Exp. ID	Fuel composition (% Vol.)	\dot{m}_f (SLPM)	Assisting co-flow composition	c_{pas} (J/kg-K)
Co-annular burner with an inner tube				
CH ₄ -Steam	100 % CH ₄	20	steam	1097
FuelMix-Steam	90 % CH ₄ + 10 % C ₃ H ₈	20	steam	1097
C ₃ H ₈ -Steam	100 % C ₃ H ₈	20	steam	1097
Co-annular burner with nebulizer				
CH ₄ -Water	100 % CH ₄	20	atomized water	4187
FuelMix-Water	90 % CH ₄ + 10 % C ₃ H ₈	20	atomized water	4187
C ₃ H ₈ -Water	100 % C ₃ H ₈	20	atomized water	4187

flowmeter) and the measured flow rates of the excess steam line (measured by the electronic balance). The flow rate of steam used in this study varied from 3.5 to 32 g/min. Due to the limited range of the precision valve, for the flow rates below 20 g/min, the total flow rate was set at 100 g/min, and for the flow rates between 20 to 35 g/min, the total flow rate was set at 200 g/min. The steam supply system was able to bypass the precision valve to calibrate the total flow rate out of the electric steam generator. The steam flow rate uncertainty was less than 10 % of the reading.

To collect gaseous and particulate combustion products completely and feed them to measurement devices, the same methods as explained in Investigation I were used. Similarly, the BC mass concentration, CO₂, and NO_x concentrations were measured by the same devices explained in Investigation I. In addition, a scanning mobility particle sizer (SMPS), which is a differential mobility analyzer (DMA) and a condensation particle counter (CPC) in series, was used to measure the size distribution of the particles. The emission indices (EI) of various exhaust products were calculated based on Eq. 1.1. For each fuel, the assisting fluid (steam or atomized water) flow rate was initially zero (dry flame), then gradually increased, which was limited by maximum flow rate of nebulizer or the detection limit of measurement devices.

3.3 Results and Discussion

3.3.1 Hydrodynamic and Thermal Characterization

To characterize the flame hydrodynamics in this investigation, due to the fact that the assisting fluid flow rates were relatively low, and fuel flow rate was constant, it turned out that all flames were buoyancy-driven. In other words, the overall hydrodynamics are controlled by the buoyancy of the combustion products, which is an increasing function of the characteristic flame temperature.

To specify a characteristic temperature, adiabatic flame temperature (T_{ad}) was calculated by NASA's CEA tool (McBride, 1996). The fuel and air mole fraction was calculated by assuming that the fuel is burnt with the stoichiometric amount of air (initially at 25 °C and 93.8 kPa), and the composition of the major products is only N_2 , CO_2 , H_2O . Based on the assisting fluid-to-fuel mass flow ratio (MFR) for each case, the mole fraction of steam (at 105 °C) and water (at 25 °C) was also calculated. The calculated T_{ad} for three fuels and the assisting fluid used is plotted in Fig. 3.2 as a function of the MFR.

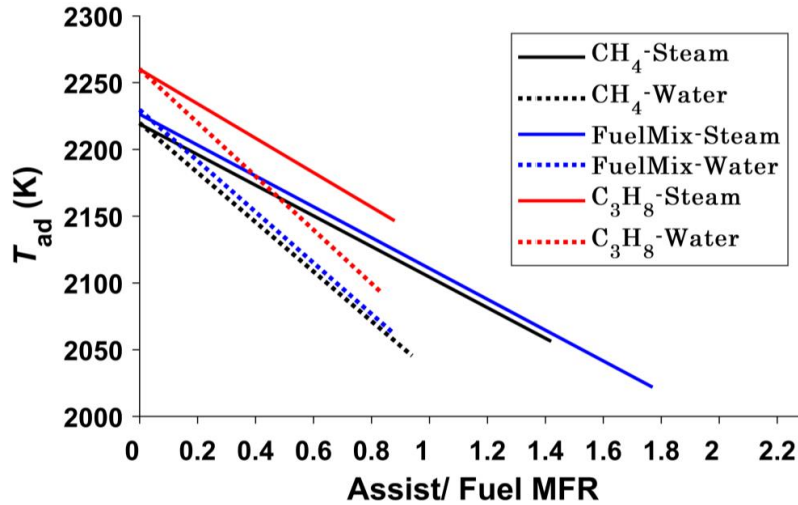


Figure 3.2: Adiabatic flame temperature vs. Assist/Fuel MFR (MFR range differs in each test)

This calculation simplifies the whole turbulent diffusion combustion process as if it occurs in a constant-pressure and constant-enthalpy reactor. Thus, it does not include the overall hydrodynamics and radiation heat losses of the actual flame. However, this calculation provides a reasonable estimate of the characteristic temperature of the actual flames. Although, steam and water have identical chemical composition, as reported in Table 3.1, c_p of water is about 4 times higher than that of steam, and water has a lower initial temperature. This justifies that, regardless of fuel composition, water addition causes a lower actual peak temperature compared to steam addition, which is consistent with the plots in Fig. 3.2. Based on this simplified model, to get steam- and water-assisted flames which have the same T_{ad} , the MFR for steam is on average 61 % more than the MFR for water for these fuels, which means 61 % more steam consumption in case of constant fuel flow rate. Based on the visual observations, all flames experienced a reduction in radiation heat losses (*i.e.*, flame luminosity) due to water and steam addition. However, this reduction in flame luminosity was more pronounced in the cases where fuel was C_3H_8 and/or the assisting fluid was water, which can make the described characteristic temperature difference between the actual steam- and water-assisted flames smaller to some extent, specifically in C_3H_8 flames.

3.3.2 Emissions Comparison

Due to low flow rates of assisting fluid, resulting in low values of MFR, the carbon conversion efficiency (CCE) was 100 % for all cases, far from CCE collapse and flame blow-off, so CCE is not plotted. The NO_x and BC emissions for two assisting fluids in these experiments (steam and atomized water) are depicted in Fig. 3.3 separately for different fuels.

Similar to the results of Investigation I, in dry CH_4 and C_3H_8 flames (MFR=0),

the EI_{NO_x} (Fig. 3.3a and Fig. 3.3e) equaled 4.01 and 3.07 g/kg-fuel, respectively, due to higher radiation heat losses in the C_3H_8 flame. In addition, the finding of Investigation I about the NO_x emissions, being thermal NO_x and sensitive to the flame temperature, can be extended to this study. For all fuel compositions, EI_{NO_x} had a decreasing trend by increasing the MFR. It was observed that water suppressed EI_{NO_x} more significantly compared to steam at the same MFR, which is due to water addition effect on characteristic flame temperature being stronger than steam addition effect on characteristic flame temperature being stronger than steam addition. As explained previously, the characteristic temperature difference between two flames depends proportionally on the c_p of the assisting fluid and inversely on the extent of radiation heat losses. This explains the smaller characteristic temperature difference between steam- and water-assisted C_3H_8 flames, which leads to a smaller difference between their NO_x emissions. In water-assisted flames (black and blue lines

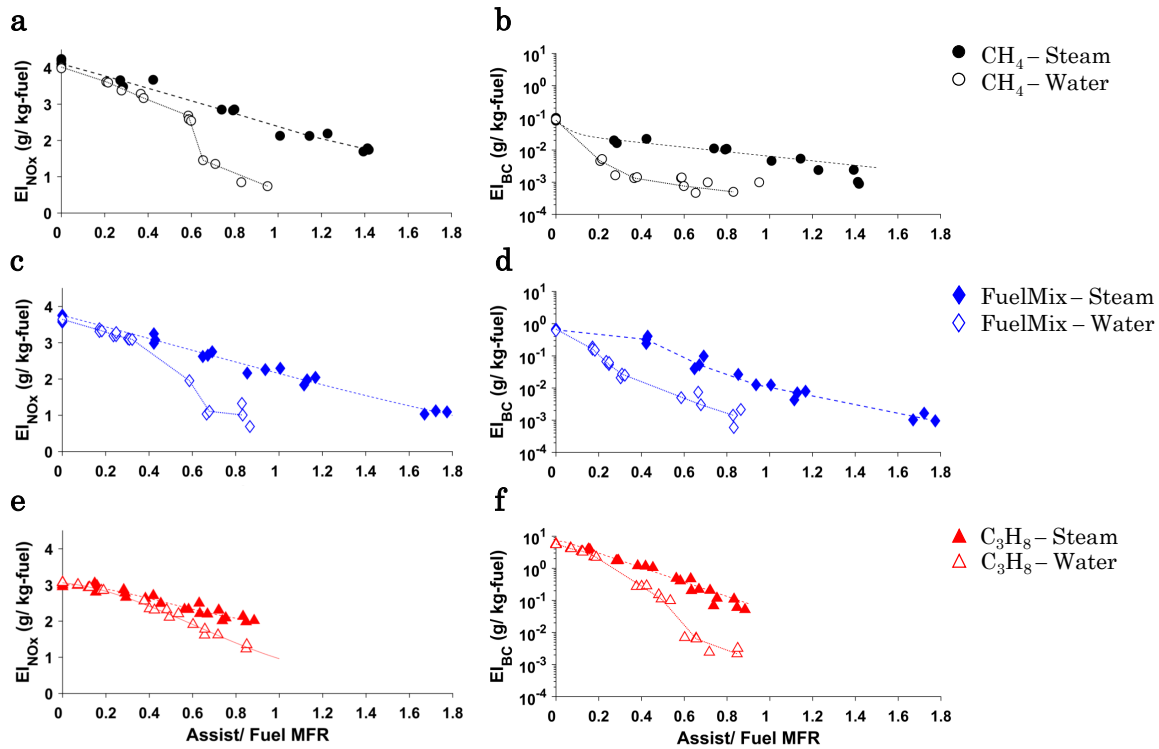


Figure 3.3: EI_{NO_x} (left column) and EI_{BC} (right column) for Investigation II (lines drawn only to help visually connect data sets). The x-axes show Assist/Fuel MFR.

in Fig. 3.3a and Fig. 3.3c, respectively), the different water droplet size generated by the 12- μm and 40- μm nebulizers can be the cause for the discontinuity in the data associated with NO_x emissions.

For all fuel compositions, EI_{BC} decreased orders of magnitude by increasing the MFR. Firstly, the start points of BC emissions (MFR=0) increased by an order of magnitude by changing the fuel composition from CH_4 to FuelMix and from FuelMix to C_3H_8 . It was also observed that the BC emissions reduction in water-assisted cases was an order of magnitude more than steam-assisted ones at the same MFR. Water and steam has the same chemical effects on inhibiting BC production and preventing formation of long-chained compounds. In addition, in the range of these experiments, they seem to have similar overall hydrodynamics, which resulted in buoyancy-driven flames. As a result, the higher BC suppression of water compared to steam is because of the stronger thermal effect of water. In other words, flame temperature reduction in the range of 100 to 200 K reduces the thermally-induced BC and the overall sooting propensity of the flames. In addition, the fuel HHV_v has a considerable influence on the BC emissions at MFR=0 and the rate at which they decreased.

The particle size distribution (PSD) of three different fuels (CH_4 , FuelMix, and C_3H_8) with steam or water addition at selected values of MFR are plotted in Fig. 3.4. For each fuel type, the markers with the same shape and color represent the MFRs, associated with steam and water cases, which are equal or close enough for being compared. The number concentration of the particulate combustion products, mostly being BC, decreased by increasing the MFR, and this decrease was more severe due to water addition compared to steam (*e.g.*, by comparing the PSD with green hexagonal star marker in Fig 3.4e and Fig 3.4f). The particle count median diameter also decreased by increasing the MFR, which is demonstrated as the maximum of PSDs shifting to the left (smaller mobility diameter) by increasing the MFR.

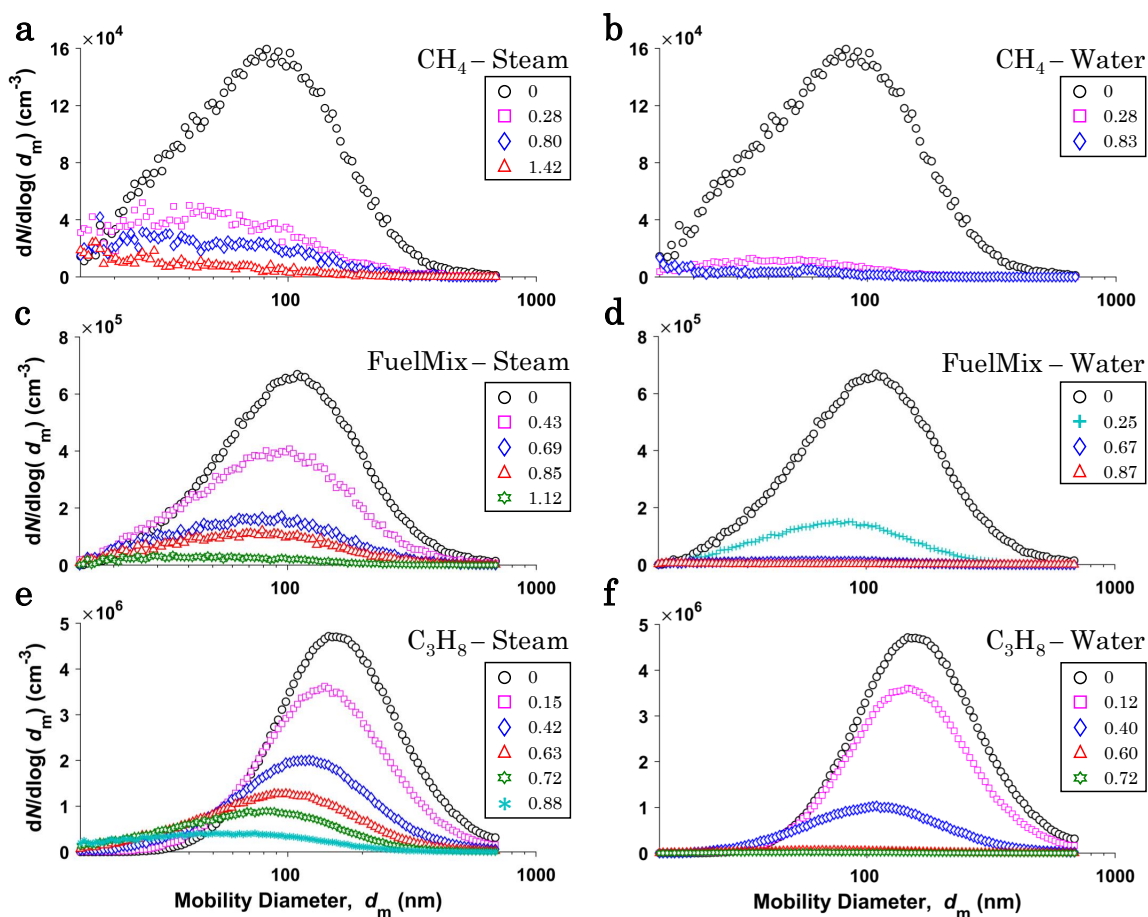


Figure 3.4: Particle size distribution for steam-assisted (left column) and water-assisted (right column) flames (for each fuel, same markers used at approximately the same MFRs).

3.4 Concluding Remarks

At low flow rates of assisting fluid, steam- and water-assisted flames with three flared gas composition were studied experimentally on lab-scale co-flow burners to characterize the overall hydrodynamics as well as peak flame temperature and to compare their EI_{NO_x} and EI_{BC} . In total, 6 cases were considered, each case repeated 3 times. In this study, the emission index (EI) results were presented in terms of the assisting fluid-to-fuel MFR.

This study focuses on hydrodynamics and thermodynamics of assisting fluid ad-

dition, since steam and water have identical chemical effects due to having the same chemical composition. At low flow rates of these two assisting fluid co-flows, it turned out that the overall hydrodynamics of the flame are the same, and they are controlled by the buoyancy of combustion products. The buoyancy depends on flame temperature, and the thermal aspects of the flames are quite different. On one hand, the fuel composition determined the extent of radiation heat losses, which inversely impact the actual peak temperature. On the other hand, water and steam had distinct heat capacities and initial feeding temperatures, which resulted in a lower actual peak temperature at the same MFR as a result of water addition.

For all fuel compositions, EI_{NO_x} had a decreasing trend by increasing the MFR, while water suppressed EI_{NO_x} more significantly compared to steam at the same MFR. This can be explained by thermal NO_x production and lower characteristic temperature due to water addition compared to steam addition.

The fuel composition (*i.e.*, its HHV_v) has a considerable influence on the BC emissions at MFR=0 and the rate at which they decreased due to co-flow addition. For all fuel compositions, EI_{BC} decreased orders of magnitude by increasing the MFR. It was observed that BC emissions reduction in water-assisted cases was an order of magnitude more than steam-assisted ones at the same MFR.

By considering the results of these experiments, the thermal effect of the assisting fluid is evident, but its hydrodynamic effect is to be investigated in more details. This leads to studying assisting fluid injection in a diffusion flame, which is the objective of Investigation III.

CHAPTER 4

Multi-slot Burner Design¹

4.1 Introduction

Documented in the literature, the jet radius and curvature impact various aspects of diffusion flames, including but not limited to dynamics, stability, flame structure, and emissions (Mansour, 2000). Furthermore, in co-annular burner geometries, similar to the ones covered in Chapters 2 and 3, the area ratio of the streams is inevitably changed by altering the diameter of the inner or outer tube. The problem is that the inner flow area cannot be altered without affecting the annulus area, which means that the ratio of either the flow velocities or Reynolds Numbers cannot both remain fixed in changing scale. On the other hand, slot burner geometries allow for independent adjustment of the width and length of each slot (Kapusta et al., 2020). Therefore, inspired by Wolfhard-Parker slot burners (Kent et al., 1981; Smyth et al., 1985; Wagner et al., 2009), a multi-slot burner was designed to overcome these issues, which allows

¹Based on a published and presented poster: **Zamani, M.**, Abbasi-Atibeh, E., Olfert, J. S., and Kostiuk, L. W. (July 2022). Design and characterization of a Multi-slot Burner, *39th International Symposium on Combustion*, Vancouver, Canada.

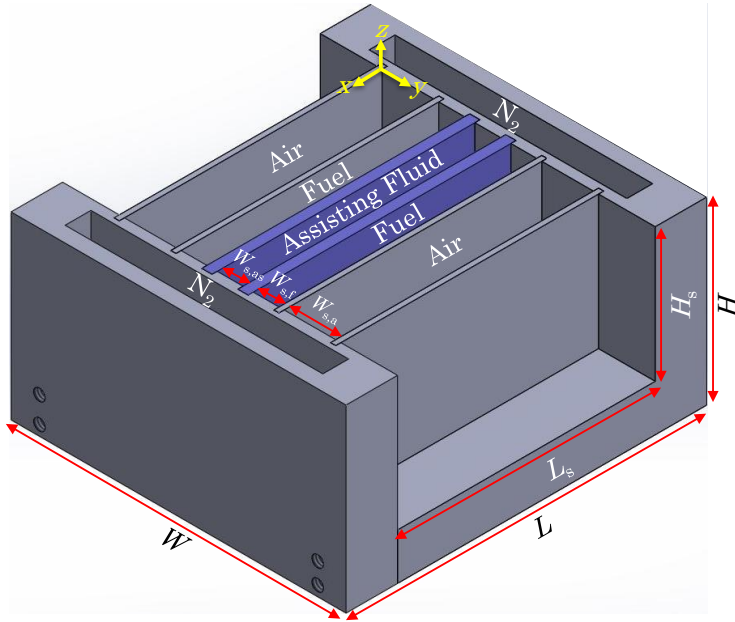


Figure 4.1: Schematic of the preliminary design of multi-slot burner

for assisting fluid injection in a diffusion flame. The multi-slot burner, the preliminary design of which is presented schematically in Fig. 4.1, consists of five parallel rectangular slots along the x -axis (*i.e.*, the central slot for assisting fluid, sandwiched by two fuel slots, and all surrounded by two air slots) as well as two rectangular slots along the y -axis for N_2 purge. The design process and limitations are discussed in this Chapter, leading to the final design of a geometrically flexible multi-slot burner.

This configuration provides excellent optical accessibility to two symmetric diffusion flames, where the effects of co-flow assisting fluid on the stability and emissions of flames can be explored. The idea is to have the assisting fluid flow rate start at zero and increase its flow rate until it interferes with flame stability. Accordingly, the width of the outer air slot needs to be a few times larger than that of fuel to minimize the difference in the exit velocities of air and fuel streams (*i.e.*, shear stresses). In the first version of this burner, the fuel slot's width equals that of the assisting fluid. To constrain the slots' height and length, some prototypes of the single slots, similar to the one shown in Fig. 4.2, were first simulated numerically and then built and

tested in a non-reacting flow condition. Afterwards, the multi-slot burner was designed, manufactured, and tested to produce stable co-flow diffusion flames, followed by some reacting flow PIV tests to characterize the exit flow.

4.2 Single Slot Design

For the single slot, schematically shown in Fig. 4.2, there are specifications and dimensions to be determined based on the relevant literature, numerical simulations, and experiments, namely the number and location of injection ports at the bottom, the slot's inner width (W_s), inner length (L_s), inner height (H_s), height of the plenum (H_{pl}), height of the bead column (H_b), height above the bead column (H_{ab}), wall material, bead material, bead diameter (D_b), and screen opening. For flow straightening, 1-mm beads were chosen.

The goal was to perform simulations and experiments within a test domain characterized by a top-hat velocity profile at the exit plane of the slots to minimize the wall effect on the flow. Therefore, a packed bed of beads was used to straighten the

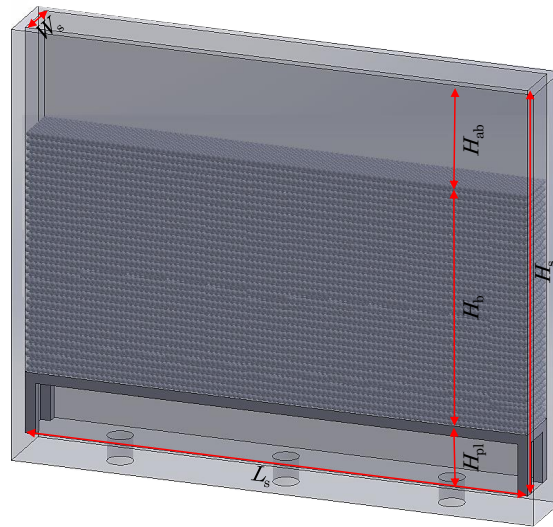


Figure 4.2: Schematic of the initial design of a single slot made of plexiglass

flow. A coarse metal mesh screen was placed underneath the bead column, which was supported by a metal frame. Also, the bead column was covered by a metal mesh screen above it to level the surface and prevent the beads from flying off. The numerical simulation and experimental tests to set the specifications and dimensions of the slots are discussed in the following Subsections.

4.2.1 Flow Simulation

In order to assess the flow uniformity at the slot exit, the uniformity index was defined and calculated. The flow uniformity index is widely employed to understand flow distribution in channel flows in the automobile industry (Guojiang and Song, 2005; Om Ariara Guhan et al., 2016) and is defined at a cross-section of a fully 3D flow as:

$$\gamma = 1 - \frac{\int |v_z - \bar{v}_z| dS}{2\bar{v}_z S_0} \quad (4.1)$$

$$\bar{v}_z = \frac{\int v_z dS}{S_0},$$

and for 2D case, this would be:

$$\gamma = 1 - \frac{\int |v_z - \bar{v}_z| dL}{2\bar{v}_z L_0} \quad (4.2)$$

$$\bar{v}_z = \frac{\int v_z dL}{L_0}.$$

The flow field inside and out of a wide single slot was numerically simulated using the Flow Simulation in SolidWorks. The 3D geometry was drawn, and a fine mesh was created in SolidWorks. The packed bed of uniform-sized spherical beads is modelled as a porous block in favour of computational efficiency. Based on the literature,

the minimum porosity (ϵ) of a packed bed of uniform-sized spheres is 0.36, whereas real packings often have values in the range of $\epsilon = 0.36 - 0.42$ (Zhang et al., 2006). Additionally, in a separate study, the porosity of packed bed of 1.039-mm spheres in a large cylindrical column was found to range from 0.4001 to 0.4206 (Pešić et al., 2015).

Input as a user-defined function, the pressure drop (Δp) across the porous block with the height of H_b was calculated based on an empirical model for a packed bed of uniform-sized spheres known as Ergun Equation (Pešić et al., 2015; Ergun, 1952), which is as follows:

$$-\frac{\Delta p}{H_b} = 150 \frac{(1 - \epsilon)^2}{\epsilon^3} \frac{\mu}{d_b^2} U + 1.75 \frac{(1 - \epsilon)}{\epsilon^3} \frac{\rho}{d_b} U^2 \quad (4.3)$$

in which μ , ρ , U , and d_b are fluid viscosity, density, superficial velocity, and bead diameter, respectively. A hypothetical flow velocity called the superficial velocity (U) is calculated as if the provided fluid were the only one moving through a reduced cross-sectional area due to the presence of the porous medium (void cross-sectional area) (Kleinstreuer, 2018). In Equation 4.3, the first term describes viscous pressure losses, and the second one describes inertial pressure losses. In the simulations, the permeability type was chosen to be isotropic, which means there is no dependence on the direction.

The specifications and dimensions for the cases that were numerically modelled are listed in Table 4.1. The fluid was assigned to be N_2 with its viscosity and density at standard conditions. The flow rate of N_2 was 80 SLPM and constant for this purpose, as this was anticipated to be the highest flow rate in practice, and observing the fact that the flow is going to be uniform for lower flow rates. In the simulations, N_2 was injected through three equally-spaced circular jets at the bottom of the slot. The screen opening placed under the porous block was chosen to be 0.75 mm (small

Table 4.1: Flow simulation cases for flow uniformity of wide single slot

Exp. ID	W_s (mm)	L_s (mm)	$H_s (H_{pl} + H_b + H_{ab})$ (mm)	ϵ	\dot{m}_{N_2} (SLPM)	calculated \bar{v}_e° (m/s)
			140 (30+30+80)	0.36		
Wide Single Slot	30	101.6	140 (30+60+50)	0.39	80	0.4374
			140 (30+90+20)	0.42		

* Base case shaded in gray

compared to D_b). These simulations confirmed the validity of the use of a porous block instead of a column of beads and also tested the effect of the block's height and porosity on the exit velocity.

As mentioned earlier, the porosity depends on the shape and size of the beads and the container. Therefore, in order to study the porosity effect, it was changed between $0.36 \leq \epsilon \leq 0.42$ while keeping everything else constant, including the height of the porous block, for several simulations. As shown in Fig. 4.3, the exit velocity profile along the long side of the wide slot is uniform, and it doesn't deviate much from the area-averaged velocity at different assigned porosities.

Considering these results, the mean porosity of that range (*i.e.* $\epsilon = 0.39$) was chosen for the rest of the simulations. Figure 4.4 illustrates the velocity contour at the exit plane of the wide slot ($H_b = 60$ mm), which also shows acceptable flow uniformity. It is worth noting that adding a porous block (*i.e.* column of beads, in

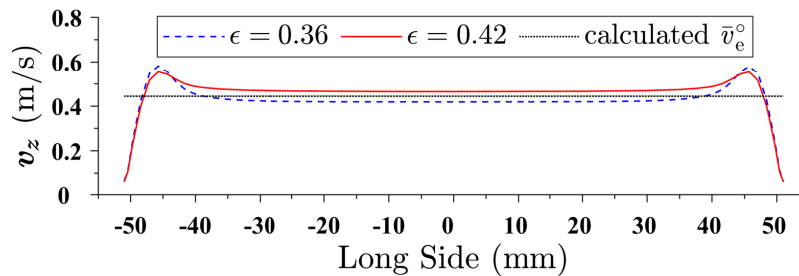


Figure 4.3: Simulated exit velocity profiles of the wide slot at two different porosities

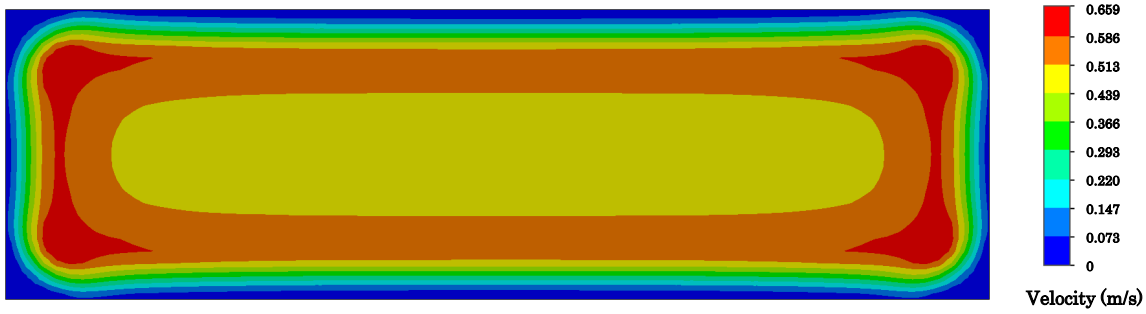


Figure 4.4: Exit velocity contour of the wide slot ($\epsilon = 0.39$)

practice) improves the exit flow uniformity. Quantitatively speaking, the uniformity index reached $\gamma = 0.966$ with a porous block and a mesh screen under that, while it was $\gamma = 0.627$ only with a mesh screen.

In another set of simulations, the height of the porous block was changed while all other parameters were kept constant, including the porosity ($\epsilon = 0.39$), the results of which are shown in Fig. 4.5. Two conclusions were drawn based on this: (1) the bead height of 60 mm is more than sufficient to straighten the flow, and (2) the height above the beads of 20 mm is also adequate. Therefore, these numbers were used for the single slot experiments to construct the geometry. Slots with shorter overall heights are preferable regarding material consumption and assembly of beads and meshes.

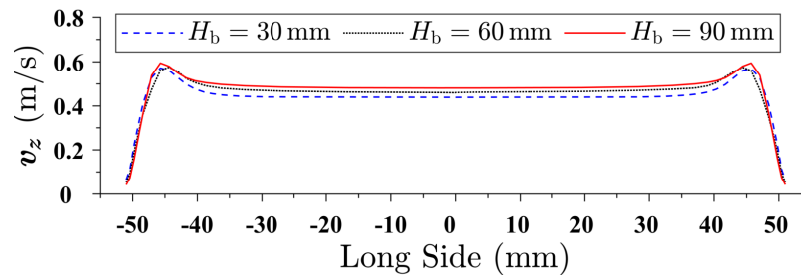


Figure 4.5: Simulated exit velocity profiles of wide slot at three different H_b ($\epsilon = 0.39$)

4.2.2 PIV Experiments

Using the particle image velocimetry (PIV) setup schematically shown in Fig. 4.6, the goal is to perform experiments within a test domain to characterize the velocity profile at the exit plane of the single slots to minimize the wall effect on the flow, especially along the long side of the slots. Therefore, packed beads were used to straighten the flow, covered by a metal screen to prevent the beads from flying. For flow straightening, 1-mm 93% zirconium oxide beads were used due to their availability and favourable material properties such as high density, $\rho_b = 6 \text{ g/cm}^3$. A packed bed of zirconium oxide beads and a layer of course metal mesh screens (mesh size 20×20 and opening size 0.76 mm) sandwiched between several layers of fine metal

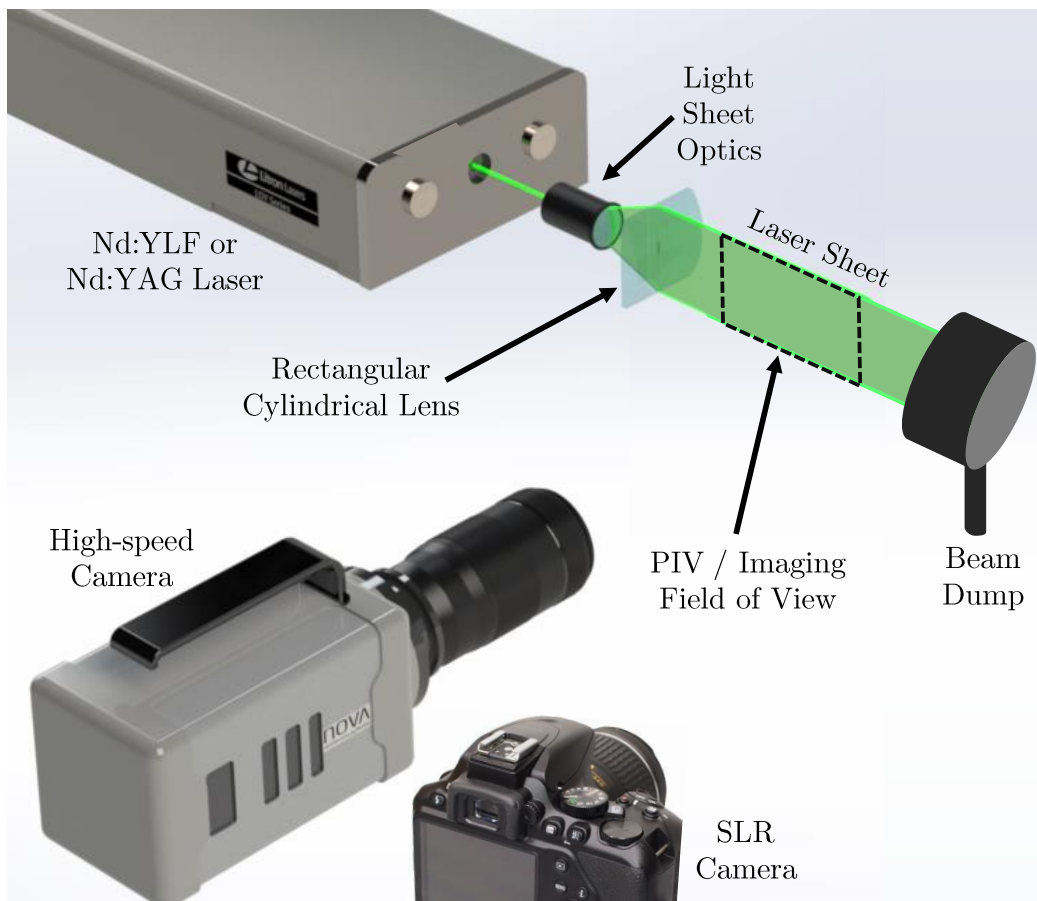


Figure 4.6: Experimental setup for cold flow and reacting flow PIV

mesh screens (mesh size 250×250 , and opening size 0.061 mm) were placed below and above the column of beads inside each slot to straighten the flow, as schematically drawn in Fig. 4.2. Having a gap below the lower mesh screens makes a plenum, which proved to be essential for breaking up the momentum of the inlet jet before entering the column of beads. As all the primary tests for single slots were non-reacting with N_2 as the working fluid, the walls were made of plexiglass due to its lightweight, good chemical resistance, and excellent machinability. Two single slots (narrow and wide) were constructed with one centered or three equally-spaced inlet jets at the bottom.

The exit velocity field of a single slot, both along the length and width, was measured using two-dimensional two-component particle image velocimetry (2D-2C-PIV) within a planar laser sheet. The N_2 stream was seeded by an oil atomizer (PIVpart14 with particle size $\approx 0.9 \mu\text{m}$) using canola oil. The oil droplets were illuminated using a thin sheet of a pulsed neodymium-doped yttrium aluminum garnet (Nd:YAG) laser at 532 nm wavelength. The Mie scattered light from the oil droplets was captured using a Photron FASTCAM NOVA S9 camera at frequencies associated with the time difference (Δt) between the image pair captured, given in Table 4.2, at the resolution of 1024×768 pixels and a pixel-to-mm ratio (p/mm) of 13.71 and 12.23 for short side

Table 4.2: PIV test matrix for flow uniformity of the single slots

Exp. ID	W_s (mm)	L_s (mm)	$H_s (H_{pl} + H_b + H_{ab})$ (mm)	\dot{m}_{N_2} (SLPM)	calculated \bar{v}_e° (m/s)	Δt (μs)
Fuel or assisting fluid slot						
Narrow Single Slot	9.53	76.2	101.6 (20+61.6+20)	2.5	0.057	14249
				10	0.230	3562
				40	0.919	891
Air slot						
Wide Single Slot	38.1	76.2	101.6 (20+61.6+20)	50	0.287	2850

and long side measurements, respectively.

The distance between independent vectors in the PIV velocity field is typically used to define spatial resolution (RES) (Scharnowski and Kähler, 2020). Thus, the spatial resolution of PIV (in mm) is proportional to the interrogation window size (I_W) plus the particle image (PI) diameter (D_{PI}), and the proportionality constant is the inverse of p/mm, which is calculated from images taken from a calibration target.

$$\text{RES} = (I_W + D_{PI}) \frac{1}{\text{p/mm}} \quad (4.4)$$

In order to calculate the average velocity vector field within the field of view, hundreds of image pairs taken were post-processed using DaVis 10.1. The interrogation window size was 16×16 pixels with a window overlapping of 50% resulting in a spatial resolution of 1.31 mm and 1.47 mm, calculated based on Equation 4.4, for short side and long side measurements, respectively.

By considering the PIV setting, the velocity field above the slots was collected and processed using DaVis 10.1, and the velocity profile along the short and long sides was extracted by plotting the upward velocity along a line placed 2 mm above the burner exit. Figure 4.7a and 4.8a show the non-reacting upward velocity profiles 2 mm above the burner exit along the short side at the mid-plane (xz -plane) of the wide and narrow slots, respectively.

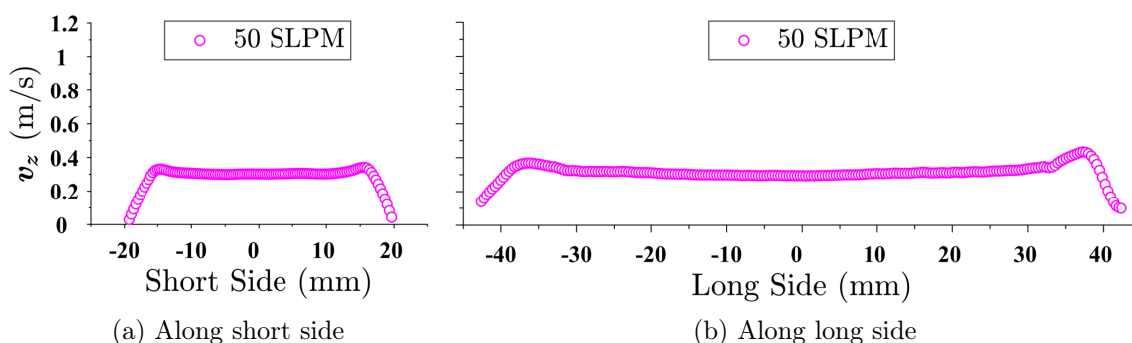


Figure 4.7: Exit velocity profiles at the mid planes of **Wide Single Slot**

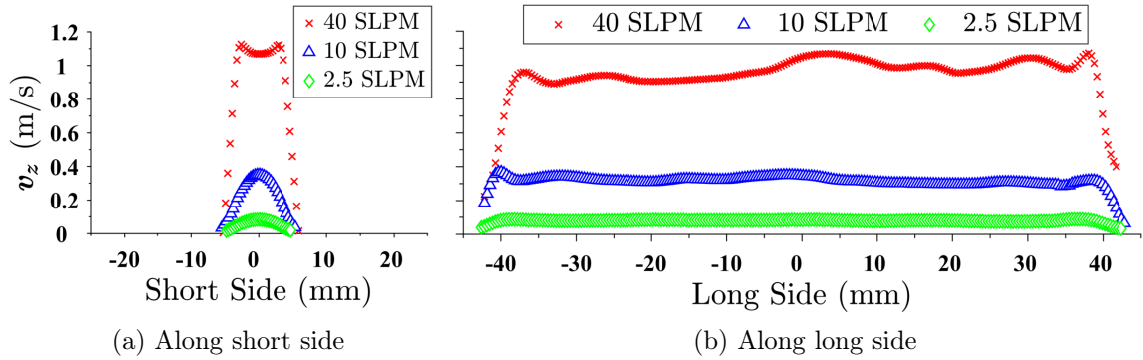


Figure 4.8: Exit velocity profiles at the mid planes of **Narrow Single Slot**

To address the quality of the 2D assumption for the flow produced by this burner design, Fig. 4.7b and 4.8b show the non-reacting v_z 2 mm above the burner exit along the long side (parallel to y -axis) at mid- yz -plane of the wide and narrow slots, respectively. After several attempts, the top-hat velocity profiles illustrated in Fig. 4.7b and 4.8b show the best possible outcome considering the complexity and randomness of the events that can happen inside the slots. That being said, the 2D flow field assumption is sufficiently valid at the center of slots for most of the cases shown. These profiles along the long and short sides also justify the acceptable symmetry of the exit velocity profiles.

4.3 Final Design

After finalizing the multi-slot burner design based on the single slot flow simulations and non-reacting flow PIV tests, the burner was manufactured and tested to produce stable co-flow diffusion flames. The construction of a low-carbon steel burner involved sandwiching together relatively thin wall elements to separate the slots and open-topped spacers to create the slots and enable the introduction of gases from the bottom inlet through extended steel tubes, as depicted in Fig. 4.9 with the final dimensions. Detailed drawings of individual elements, including separating walls and

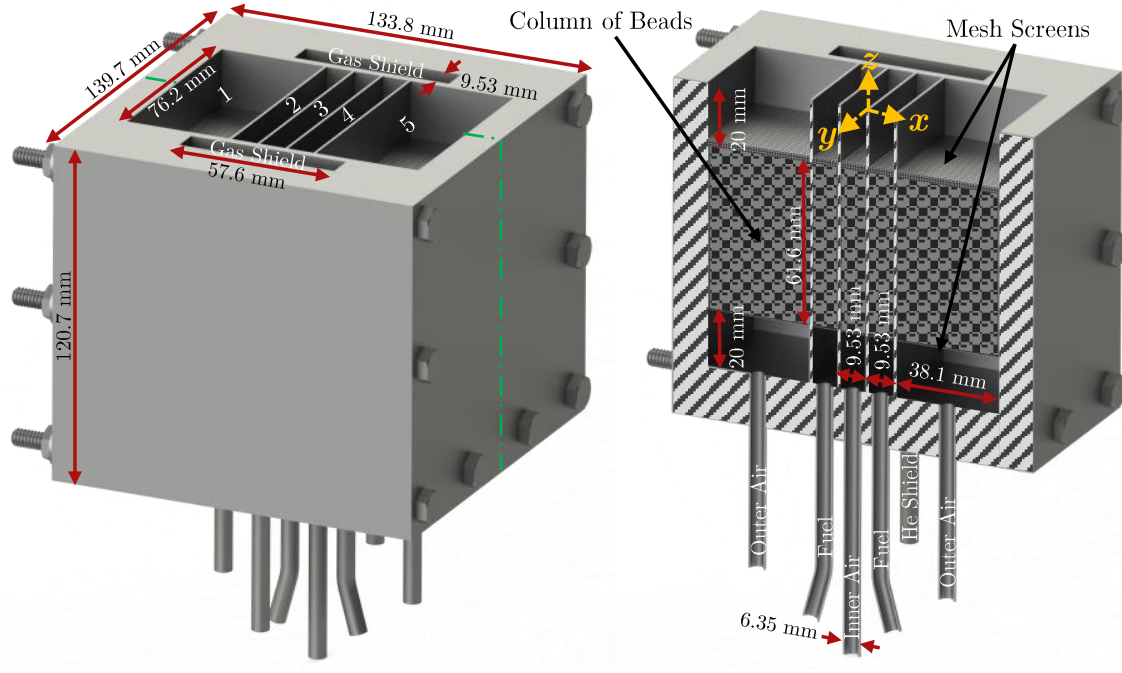


Figure 4.9: Schematic of the final design of multi-slot burner and its dimensions

open-topped spacers, are provided in Appendix D.

This burner readily allows for varying the composition and flow rate of different streams (*i.e.* air, fuel, and assisting fluid). However, it might be challenging to seed the assisting fluid stream when steam is used, similar to Chapter 2 and 3. Depending on the flow configuration introduced into these five parallel slots, various symmetric or asymmetric diffusion, partially-premixed, or premixed flames can be stabilized on this multi-slot burner while providing optical access to the flames. However, in this study, only symmetric normal and inverse diffusion flames were tested and studied, which are characterized by defining the global equivalence ratio (GER). Although the concept of GER was first introduced in fire research (Pitts, 1995), for measuring the level of ventilation, GER has been widely used in diffusion flame research (Tolocka et al., 1999; Ouf et al., 2008; Elbaz and Roberts, 2016), which is basically the normalized fuel-to-air mass flow ratio and is defined as:

$$\text{GER} = \frac{\left(\frac{\dot{m}_F}{\dot{m}_A}\right)_{\text{experiment}}}{\left(\frac{\dot{m}_F}{\dot{m}_A}\right)_{\text{stoichiometry}}} \quad (4.5)$$

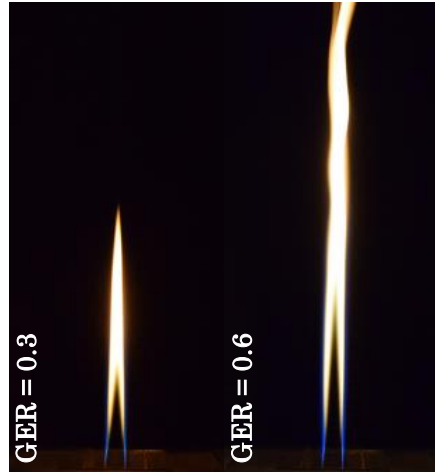
Table. 4.3 shows the experimental matrix for symmetric diffusion flames, namely two cases of a normal diffusion flame (NDF), four cases of an inverse diffusion flame (IDF), and three cases of an IDF in a NDF. The flow configuration (*i.e.* composition and flow rate) out of the five numbered slots in Fig. 4.9 is also given in Table. 4.3, and all flames are shielded from surrounding air by N₂ shields at both ends. The GER in these cases was limited by the onset of flame instability and lift-off.

Taken with the same aperture, ISO speed, and shutter speed, the SLR images of all of these optically accessible 2D flames are shown in Fig. 4.10. For two cases of a NDF that are closed-tip, GER was doubled by doubling the fuel flow rate. The case

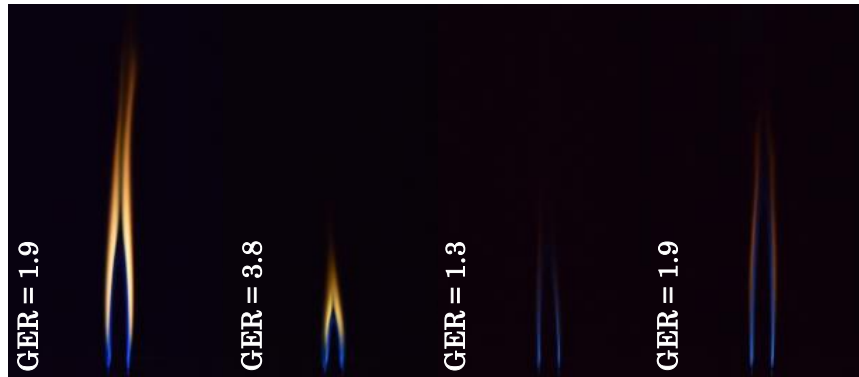
Table 4.3: Flow configuration of each slot for different diffusion flames in the multi-slot burner (the flow rates of separate streams are given in SLPM).

Exp. ID \ Slot #	1	2	3	4	5
Normal Diffusion Flame					
NDF (GER=0.3)	45 N ₂	40 Air	2.5 CH ₄	40 Air	45 N ₂
NDF (GER=0.6)	45 N ₂	40 Air	5 CH ₄	40 Air	45 N ₂
Inverse Diffusion Flame					
IDF (GER=1.9)	45 N ₂	2.5 CH ₄	25 Air	2.5 CH ₄	45 N ₂
IDF (GER=3.8)	45 N ₂	2.5 CH ₄	12.5 Air	2.5 CH ₄	45 N ₂
IDF (GER=1.3)	45 N ₂	1.25 CH ₄ + 1.25 N ₂	18 Air	1.25 CH ₄ + 1.25 N ₂	45 N ₂
IDF (GER=1.9)	45 N ₂	2.5 CH ₄ + 2.5 N ₂	25 Air	2.5 CH ₄ + 2.5 N ₂	45 N ₂
IDF in NDF					
Non-interacting	100 Air	2.5 CH ₄	5 Air	2.5 CH ₄	100 Air
Interacting	100 Air	2.5 CH ₄	20 Air	2.5 CH ₄	100 Air
Merged	100 Air	2.5 CH ₄	35 Air	2.5 CH ₄	100 Air

Normal Diffusion Flames (NDF)



Inverse Diffusion Flames (IDF)



IDF in NDF

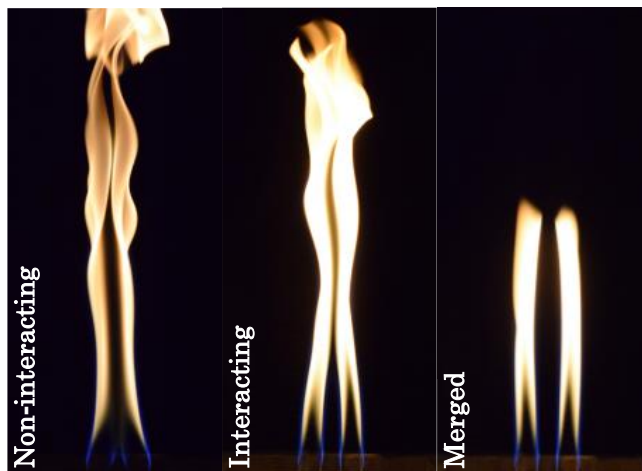


Figure 4.10: SLR images of different methane diffusion flames stabilized in the designed multi-slot burner.

of a NDF (GER=0.3) is a candle-like flame, while a NDF (GER=0.6) was more than two times longer in height. The high luminosity corresponds to the soot formation in the flame zone. For the first two IDF cases, GER was doubled by halving the air flow rate, and the flame height was almost halved correspondingly. IDFs are less luminous and have thinner luminous flame compared to NDFs. For the other two IDF cases, the fuel stream was diluted by N_2 to expand the operating range by increasing its exit velocity. By N_2 dilution, the luminosity of the flames was significantly reduced, and the light orange flames tended to be darker and redder. Lastly, three cases of an IDF in a NDF were stabilized, which resemble the flow configuration of an internally air-assisted flare in 2D, and they are categorized based on the interaction of four formed flame bases. GER calculated based on the inner air or summation of inner and outer air is not a well-defined parameter to categorize these flames. Air available for the fuel's combustion can come from three sources: (1) the quiescent surrounding air, (2) the outer air flows of the burner, and (3) the inner air flow of the burner. Two of these sources (the surrounding air and outer air flows) are always in contact with each other and inseparable as a source of air. The case of an IDF in a NDF is studied more thoroughly in Chapter 5.

Another distinct feature of this multi-slot burner is that the separating wall thickness can be changed without changing the dimensions of the individual slots. If the separating wall is between two slots from which fuel and oxidizer are injected, the flame base will be anchored to the edge of the separating wall. Therefore, the thickness of the separating wall impacts the flame aerodynamics, stability, and onset of liftoff. After stabilizing the flames in the multi-slot burner, a possible future work would be studying the effect of wall thickness on the stability of the flame while keeping all other dimensions of the slots fixed.

4.3.1 Sample Reacting flow PIV

The velocity field upstream of the flames can be measured by using the reacting flow PIV tests, which is schematically illustrated in Fig. 4.6, which is the same as the cold flow PIV. These results would help in understanding the effects of co-flow assisting fluid on hydrodynamics and stability of this type of diffusion flame. For the reacting flow cases, time-resolved PIV was done to determine if small changes in velocity were the result of the natural periodic oscillations or actually present in the flow field. The streams (inner air, fuel, and outer air) were seeded with titanium dioxide (TiO_2) particles (150–250 nm when agglomerated) using three separate solid seeders (Dantec PS10, LaVision Particle Blaster 110, and PIVTEC PivSolid3, respectively). The seeding particles were illuminated by a thin sheet of a dual cavity neodymium-doped yttrium lithium fluoride (Nd:YLF) laser at 527 nm wavelength (Litron LD30-527). The Mie scattered light from the particles was captured using a Photron FASTCAM NOVA S9 camera with a narrow bandpass filter (527/20 nm) mounted on the camera lens. Figure 4.11 illustrates a raw PIV image for the case of an interacting IDF in a NFD. As mentioned earlier, several cases for the coexistence of normal and inverse

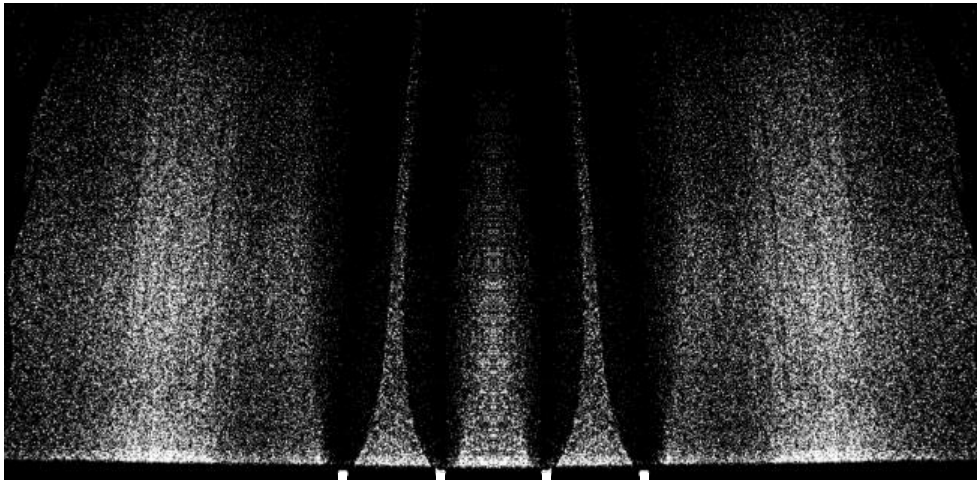


Figure 4.11: Raw PIV image of an interacting IDF in a NFD case.

diffusion flames, including a case similar to Fig. 4.11, will be processed to reveal the mean velocity field in the following Chapter.

4.4 Concluding Remarks

The designed multi-slot burner shows a promising ability to stabilize normal and inverse diffusion flames, as well as the coexistence of both in various configurations. The geometric flexibility allows independently changing any slot width (length scale associated with reacting layers) and wall thickness (length scale associated with initial mixing/shear layers). Reacting flow PIV is to quantify the flow field in fuel-oxidant shear/mixing layers. It is worth noting the seeding density reduction close to the flame due to heat release is challenging.

CHAPTER 5

Investigation III: Co-flow Jet Diffusion Flame in a Multi-slot Burner¹

5.1 Introduction

The rising trend in the Earth's atmospheric temperature is a global concern (Solomon et al., 2009), which is associated with changing atmospheric composition in both gaseous and particulate phases (Solomon et al., 2009; Lelieveld et al., 1993; Moosmüller et al., 2009). Unsurprisingly, fossil fuel combustion emissions are considered a key anthropogenic contributor to these changes. Notwithstanding the increasing contribution of renewables, fossil fuel combustion will continue to provide a significant share of global energy demand over the next decades (IEA, 2019).

Among the different means of gaseous fuel combustion, forced convection-diffusion flames are at the heart of many devices as dissimilar as furnaces, gas turbines, or the

¹Based on a published paper: **Zamani, M.**, Abbasi-Atibeh, E., Olfert, J. S., and Kostiuk, L. W. (2022). Co-flow jet diffusion flames in a multi-slot burner: Flow field and emissions. *Process Safety and Environmental Protection*, 167, 686-694.

deceptively straightforward industrial flares in which unwanted flammable gases or vapours are burned in the open atmosphere. In all these flames, the fuel flow is forced while the oxidant (*i.e.*, air) is either sourced from the quiescent surroundings (*e.g.*, a simple jet flame (Sunderland et al., 1999)), or the air's initial movement is dominated by its own momentum (*e.g.*, when a separate stream of air is forced into the fuel being flared, thereby creating an air-assisted flare (Torres et al., 2012)). The flow field, which establishes the mixing and interactions between the fuel and air streams, as well as the products of combustion, can dramatically affect the quantity of undesired emissions (Duck, 2011). For instance, flares operating as standard jet diffusion flames (Brzustowski, 1976) are often scrutinized for their emissions to assess if the emissions are in an acceptable range (Johnson and Kostiuk, 2000; Strosher, 2000). In an attempt to reduce such emissions, an air-assisted flare could be used (McDaniel and Tichenor, 1983; Torres et al., 2012; Alhameedi et al., 2022). However, in a recent study (Zamani et al., 2021), an unexpected increasing trend in black carbon (BC) emissions was observed at low flow rates of assisting air that suddenly reversed itself at slightly higher flow rates of assisting air. The reason for the observed trends in BC emissions was not identified. Therefore, further investigation is warranted on the BC emissions with increasing assisting air flow rates by zooming into the regions of air flow rates where these unexpected trends occur to examine the universality of such results, which is a part of the focus of this study. Another attempt was made to resolve this transition in BC emissions in axisymmetric configuration (Mobaseri, 2021), in two scaled geometries, but was unable to decouple the effects of air-to-fuel mass flow ratio and the inner tube wall thickness on the results.

Diffusion flames can either be configured as a normal jet diffusion flame (NDF) or an inverse jet diffusion flame (IDF). In NDFs, a fuel jet is surrounded by an oxidizer flow (Wang et al., 2012), while in IDFs, the oxidizer and fuel positions are switched.

IDFs consist of an inner jet of oxidizer surrounded by an annular jet or multiple circular jets of fuel (Blevins et al., 2002; Oh et al., 2005; Sobiesiak and Wenzell, 2005; Ying and Liu, 2018; Sidebotham and Glassman, 1992; Zhang et al., 2012; Elbaz and Roberts, 2014, 2016; Sze et al., 2006; Zhen et al., 2011; Kapusta et al., 2020). These air and fuel flows may be either surrounded by an inert gas shield to isolate the flame from the surrounding air (Blevins et al., 2002; Oh et al., 2005; Sobiesiak and Wenzell, 2005; Ying and Liu, 2018), confined in a rigid shield to avoid interactions with ambient air currents (Sidebotham and Glassman, 1992; Zhang et al., 2012; Elbaz and Roberts, 2014, 2016), unconfined in a quiescent atmosphere to allow ambient air entrainment (Sze et al., 2006; Zhen et al., 2011; Kapusta et al., 2020), or confined in a controlled air flow (Lim et al., 2017). Reflecting upon the air-assisted flares discussed earlier, their structure is most like the unconfined in a quiescent atmosphere where this outer mixing layer establishes an outer NDF, which puts an IDF and an NDF in close proximity to each other. In terms of application, IDFs have the desirable characteristics of both premixed and diffusion flames, namely, emitting less pollutants and avoiding flashback, respectively (Dong et al., 2007). Except for Sze et al. (2006) who studied not only the emission index of oxides of nitrogen (NO_x) for a range of overall equivalence ratio, but also the IDF structure, the other studies were concentrated on the morphology or formation process of soot particles (Blevins et al., 2002; Oh et al., 2005; Ying and Liu, 2018; Sidebotham and Glassman, 1992) or the overall flame structure and its local distinct zones as well as degrees of partial premixing in IDFs (Sobiesiak and Wenzell, 2005; Zhang et al., 2012; Elbaz and Roberts, 2014, 2016; Zhen et al., 2011; Kapusta et al., 2020). It is worth noting that Lim et al. (2017) used a triple co-flow burner with constant inner air flow and increasing outer air flow to control the degree of carbonization of the emitted soot particles, which was mainly focused on measuring the optical properties of soot particles with various

organic carbon contents. Their relevant discovery is that the presence of a small IDF inside the main flame raises the temperature near the nozzle exit and increases the degree of fuel pyrolysis, both of which promote soot formation. However, the works mentioned above neither evaluated the interactions of an IDF inside an NDF by varying the inner air flow nor simultaneously quantified NO_x and BC emissions, and the present study is intended to fill this knowledge gap.

Although IDFs have been mostly established in co-annular burner geometries, it has also been shown that the jet radius and curvature affect the dynamics, stability, flame structure, and emissions (Mansour, 2000). In addition, changing the diameter of the inner or outer tube in co-annular burners varies the area ratio of the streams. In contrast, in slot burners, the width and length of each slot can be changed independently (Kapusta et al., 2020). Therefore, it is beneficial to consider a burner geometry similar to the Wolfhard-Parker slot burner, the idea of which was first introduced in 1949 (Wolfhard and Parker, 1949). The burner produced a two-dimensional (2D) diffusion flame with a thicker reaction zone with one fuel and one oxidizer rectangular slots parallel to each other along the long side and surrounded by a flow of inert gas. To study the soot formation and particle generation rates inside a diffusion flame, a modified Wolfhard-Parker slot burner was redesigned with the fuel slot being sandwiched between two air slots, which produced two symmetric flame sheets (*i.e.* NDF in slot configuration) (Kent et al., 1981; Smyth et al., 1985). Another recent variation to this type of burner was to add two N_2 purge slots at the ends of the fuel slot in order to diminish the end-flame effects (Wagner et al., 2009).

Mimicking the flow configuration of internally air-assisted flares (Torres et al., 2012; Zamani et al., 2021), the data and analysis presented here are principally about the coexistence of IDFs and NDFs in close proximity and their interaction in a multi-slot burner, which was used to create 2D flames with unobstructed line-of-sight access

to the flows adjacent to the flame sheets. In other words, the IDF is unconfined but with a prescribed outer air flow through two outer slots forming a separate outer NDF. A novel feature of this multi-slot burner compared to co-annular burners is that the thickness of the wall separating fuel and air and the width of each slot can be changed while keeping the area ratio (or the velocity ratio) of the streams constant, which resolves the problem described earlier about decoupling the air-to-fuel mass flow ratio and the wall thickness in an axisymmetric geometry (Mobaseri, 2021).

The main objective of this research is to quantify changes in key emission metrics (*i.e.*, BC and NO_x) and relate them to the flow field of an unconfined IDF inside an NDF by investigating the physical processes occurring in various 2D shear-mixing layers created in a relatively novel multi-slot burner.

5.2 Experimental setup and methodology

An overview of the experimental setup of this study is presented in Fig. 5.1, and its elements, namely, the multi-slot burner, velocity field measurement setup, and emission measurement devices are described with more details in the following subsections.

5.2.1 Multi-slot Burner Design

Inspired by Wolfhard-Parker slot burner (Kent et al., 1981; Smyth et al., 1985; Wagner et al., 2009), a multi-slot burner was designed that allows for co-flow injection of fuels and oxidants. This multi-slot burner, which is presented schematically in Fig. 5.2, consists of five parallel rectangular slots (*i.e.*, the central slot for the inner air in between two fuel slots, and two outer air slots) and two rectangular end slots for helium (He) shields to dampen end effects. The burner, made of low-carbon steel, was constructed by sandwiching together open-topped spacers to create the slots and

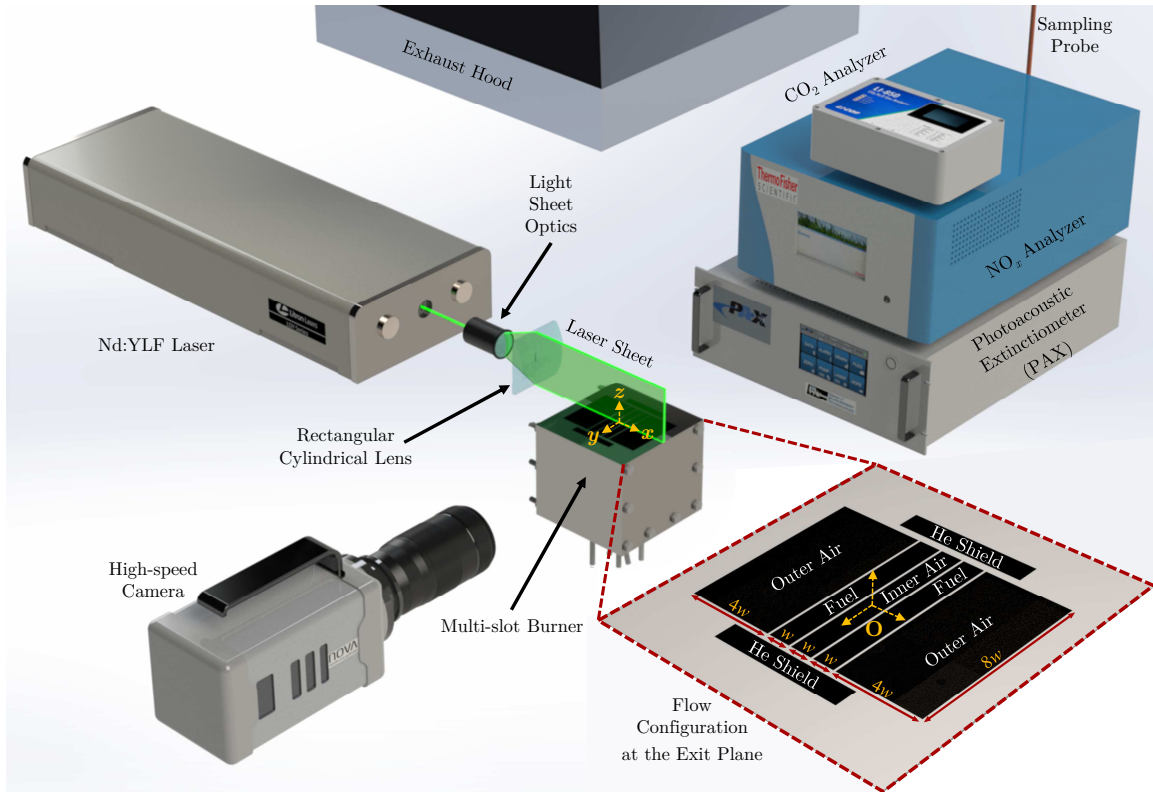


Figure 5.1: Schematic of the experimental setup (point "O" represents the origin of the coordinate system).

allow gases to be introduced from the bottom through steel tubes, and relatively thin wall elements to create the separate slots. In this design, the minimum thickness of the open-topped spacers for three central slots (*i.e.*, the width of fuel slots and inner air slot) was a constraint to accommodate inlet steel tubes. In this burner configuration, the fuel slots and inner air slot had widths of $w = 9.53$ mm, while the outer air slots were four times wider ($4w$). All five slots were $8w$ long. The walls separating the slots had a thickness of 0.91 mm. The other dimensions of the slots are given in Fig. 5.2. When viewed along the y -axis, this configuration provides optical access to the symmetric diffusion flames, where the effects of inner air on the stability and emissions of flames can be explored.

In these experiments, 3 standard liters per minute (SLPM) of propane (C_3H_8) were

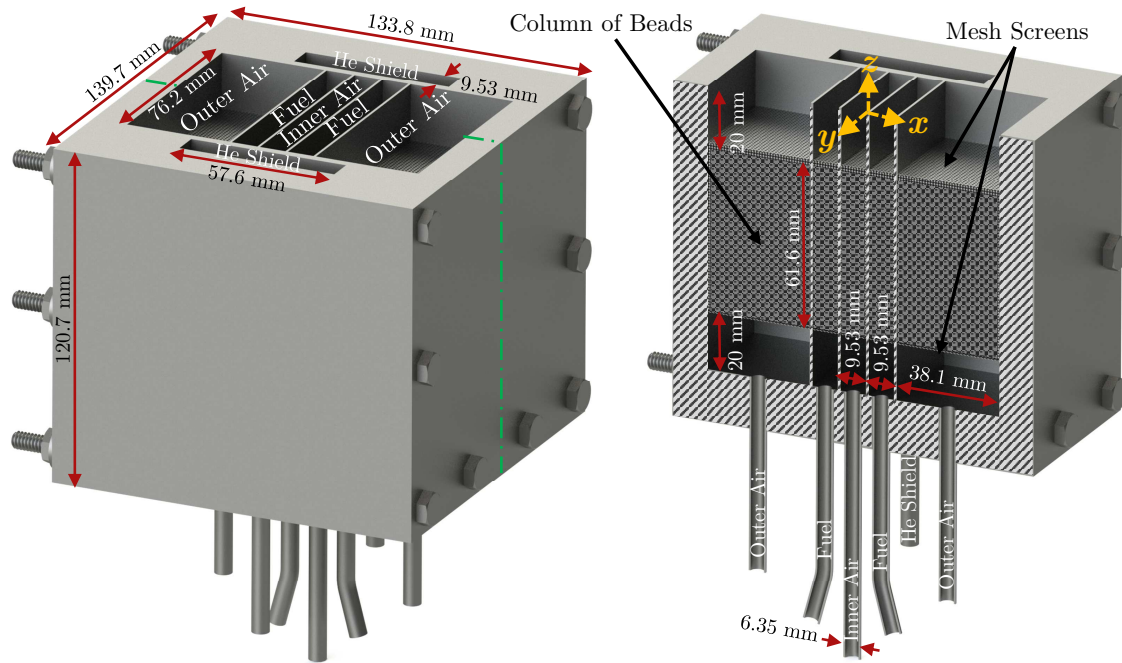


Figure 5.2: Multi-slot burner and its sectional view.

split into two equal streams feeding the two fuel slots, where standard conditions are 25 °C and 101.325 kPa. The flow rate of air through the outer slots (100 SLPM) was adjusted to be more than the required stoichiometric amount (*i.e.*, globally lean mixture). Accordingly, the width of the outer air slots was larger than that of the fuel to minimize the exit velocity difference between the air and fuel streams (*i.e.*, low shear stresses). The inner air flow rate was manipulated from zero to a point where it interfered with the inner flame’s stability (greater than 45 SLPM). In addition, 40 SLPM of He was divided into two equal streams feeding the two shield slots.

Satisfying the 2D assumption required having uniform upward velocity (v_z) along the long side (y -axis) of the slots and minimizing the effects of the end walls. To aid in creating this uniform flow, a packed bed of zirconium oxide beads (1 mm in diameter) and a layer of coarse metal mesh screens (mesh size 20×20 and opening size 0.76 mm) sandwiched between several layers of fine metal mesh screens (mesh size 250×250 and

opening size 0.061 mm) were placed below and above the column of beads inside each slot to straighten the flow, as schematically drawn in Fig. 5.2. Having a gap below the lower mesh screens makes a plenum, which proved to be essential for settling the momentum of the inlet jet before entering the column of beads.

5.2.2 Near-exit Velocity Field Measurements and Flame Visualization

The velocities were measured using two-dimensional two-component particle image velocimetry (2D-2C-PIV). The inner air was seeded with canola oil droplets ($\approx 0.9 \mu\text{m}$) using an oil seeder (PIVTEC PIVpart14), while the fuel and outer air streams were seeded with titanium dioxide (TiO_2) particles (150 – 250 nm when agglomerated) using separate solid seeders (LaVision Particle Blaster 110 and PIVTEC PivSolid3, respectively). The seeding particles were illuminated by a thin sheet of a dual cavity neodymium-doped yttrium lithium fluoride (Nd:YLF) laser at 527 nm wavelength (Litron LD30-527). The Mie scattered light from the particles was captured using a Photron FASTCAM NOVA S9 camera with a narrow bandpass filter (527/20 nm) mounted on the camera lens.

For the reacting flow cases, time-resolved PIV was done at an imaging rate of 3.124 kHz, an exposure time of 1.1 μs , a resolution of 1024 \times 768 pixels, and a pixel-to-mm ratio of 14.53. In order to calculate the velocity vector field within the imaged plane with a height of about 50 mm above the burner exit, captured images were post-processed using DaVis 10.2. The interrogation window size was 12 \times 12 pixels with window overlapping of 75 % resulting in a spatial resolution of 0.826 mm.

To address the quality of the 2D assumption for the flow produced by this burner design, Fig. 5.3 shows the non-reacting v_z 2 mm above the burner exit along the long side (parallel to y -axis) at mid- yz -plane of the inner air, outer air, and fuel slots. The top-hat velocity profiles illustrated in Fig. 5.3 show that the 2D flow field

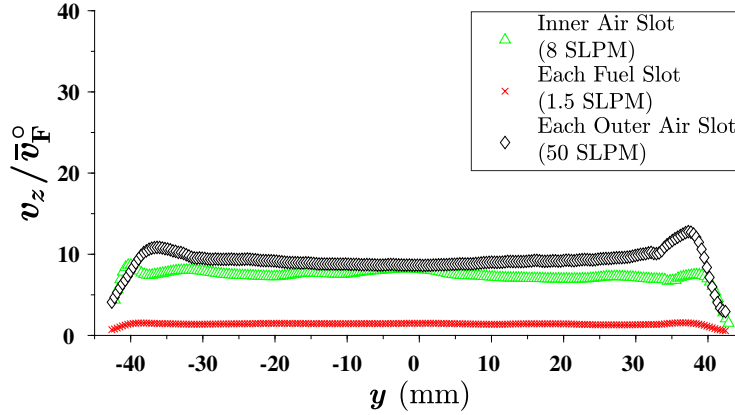


Figure 5.3: Upward exit velocity profiles at $z = 2$ mm and $x =$ mid plane of each slot.

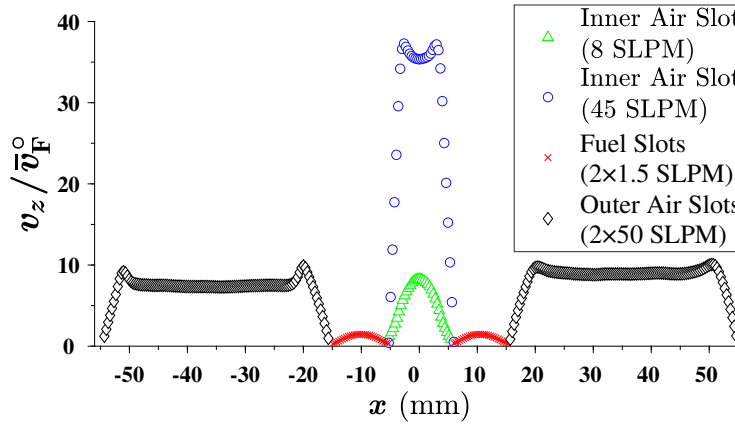


Figure 5.4: Upward exit velocity profiles at $z = 2$ mm and $y = 0$ mm.

assumption is sufficiently valid at the center of slots. Figure 5.4 shows the non-reacting upward velocity profiles for the five parallel slots 2 mm above the burner exit along the short side at the mid-plane (xz -plane). These velocity profiles justify the symmetry between the slots' exit velocity profiles. The presented velocities were normalized by the area-averaged fuel velocity, \bar{v}_F^o , where the superscript o represents that the data is calculated based on mass flow controller (MFC) readings.

Lastly, a single-lens reflex (SLR) camera was also used to image the whole flame for estimating the visible flame height, as well as to image the same field of view as the PIV images thereby allowing the visible flame to be mapped onto the PIV images and the velocity fields. Flame surface tracking methods (Abbasi-Atibeh and Bergthorson,

2019) were used to track the 2D projection of the flame surface in each frame within the planar laser sheet by tracking the regions of maximum intensity gradients at luminous flame regions. This data was used to determine a characteristic average overall flame height using 50 images.

5.2.3 Emission Measurements

For global emission measurements, all combustion products were collected using an exhaust hood. Samples of exhaust gases were extracted through a sampling probe for species measurement. More details of sample collection can be found elsewhere (Zamani et al., 2021). The extracted products were directed to a NO_x analyzer for NO_x measurements, a photoacoustic extinctionsmeter (PAX) for BC mass concentrations, and a CO_2 analyzer to monitor any changes in overall combustion efficiency, *i.e.*, conversion of fuel-based carbon to CO_2 , with further details in Section 5.3. The PAX used a laser with 870 nm wavelength; thus, a black carbon mass absorption cross-section of $4.74 \text{ m}^2/\text{g}$ was used (Bond and Bergstrom, 2006) to convert the absorption measurement to the equivalent BC mass concentration. The NO_x ($\text{NO} + \text{NO}_2$) concentration was measured with an uncertainty of 1% of the reading value.

5.2.4 Data Analysis and Presentation

The emission index (EI) of an exhaust product is calculated as the mass flow rate of an exhaust species produced by the flame ($\dot{m}_{j, \text{produced}}$) per mass flow rate of fuel (\dot{m}_{F}) (Corbin and Johnson, 2014),

$$\text{EI}_j = \frac{\dot{m}_{j, \text{produced}}}{\dot{m}_{\text{F}}}. \quad (5.1)$$

where j represents a specific species and F represents the fuel or flared gas, and $\dot{m}_{j, \text{produced}}$ is calculated based on the overall mass balance in a defined control volume.

The ratio of the area-averaged velocity of inner air ($\bar{v}_{A_I}^o$) to the area-averaged velocity of fuel (\bar{v}_F^o) is defined as the average velocity ratio (\bar{V}_r). This ratio of upward velocities was used to characterize different cases in this study. It should be emphasized that the emission measurements were done for unseeded flows. Therefore, emission measurements are not affected by oil seeding. However, the authors quantified the maximum oil consumption rate, occurring at the highest inner air flow rate (55 SLPM), through gravimetric analysis using polytetrafluoroethylene (PTFE) filters. The mass flow ratio of oil to fuel used in PIV measurements is 0.00016.

5.3 Results and discussion

Table 5.1 shows the area-averaged velocities for outer air, fuel, and inner air slots for all the cases investigated, where \bar{V}_r ranges between 0 and 37. The Reynolds numbers, calculated based on the characteristic velocity being the area-averaged velocity and the characteristic length being the hydraulic diameter of the rectangular slots, are $Re_F = 134$ and $Re_{A_O} = 968$ for the fuel and outer air slot, respectively. The values for the inner air (Re_{A_I}) are reported in the sixth column of Table. 5.1.

The visual appearance of the flames close to the burner exit is laminar and stationary, but as a result of increasing buoyancy over the flame height, they become weakly turbulent flames. Similar to candles, these flames develop noticeable natural periodic oscillations higher up in the flame. On the left side of Fig. 5.5, whole flame images are shown at four test conditions. In these images, the visible 2D projection of the flame surface was drawn (blue lines), which were used to determine a characteristic average overall flame height. The flame heights normalized by w are listed in the seventh column of Table. 5.1, and show the flame height decreases monotonically by increasing \bar{V}_r , *i.e.*, adding more inner air, as the required air for propane combustion is more readily available.

Table 5.1: Area-averaged velocities and measured characteristics at different \bar{V}_r .

$\bar{v}_{A_O}^o$ (m/s)	\bar{v}_F^o (m/s)	$\bar{v}_{A_I}^o$ (m/s)	$\frac{\bar{v}_{A_O}^o}{\bar{v}_F^o}$	\bar{V}_r $= \frac{\bar{v}_{A_I}^o}{\bar{v}_F^o}$	Re_{A_I}	heights normalized by w	
						overall flame	oil droplets isotherm
↑ 0.29 ↓	↑ 0.034 ↓	0.00	↑	0.00	0	36.1	0.0
		0.09		2.67	103	35.1	0.1
		0.18		5.33	207	33.7	0.8
		0.27		8.00	310	32.4	1.3
		0.34		10.00	387	32.1	1.9
		0.45		13.33	516	29.9	2.6
		0.57		16.67	645	27.7	3.5
		0.79		23.33	904	26.5	5.4
		1.02		30.00	1162	24.9	NA
		1.13		33.33	1291	24.4	NA
1.25	36.67	1420	23.3	NA			

As illustrated in Fig. 5.5, when no inner air was provided ($\bar{V}_r = 0$), only two flame bases existed and formed an NDF. These two flame bases are referred to as the outer flame because once the inner air was introduced, two more flame bases appeared inside these outer flames and formed an IDF (referred to as the inner flame). Based on the inner flame shape and its interaction with the outer flame, the cases in this study can be categorized as:

- (i) $0 < \bar{V}_r \leq 5.33$, a closed-tip inner flame visually separate from the outer flame
- (ii) $5.33 < \bar{V}_r \leq 13.33$, an open-tip inner flame, but at higher heights becoming indistinguishable from outer flame
- (iii) $13.33 < \bar{V}_r \leq 30$, an open-tip inner flame with an air jet essentially partitioning the right and left flames
- (iv) $\bar{V}_r > 30$, a lifted inner flame interacting with the outer flame.

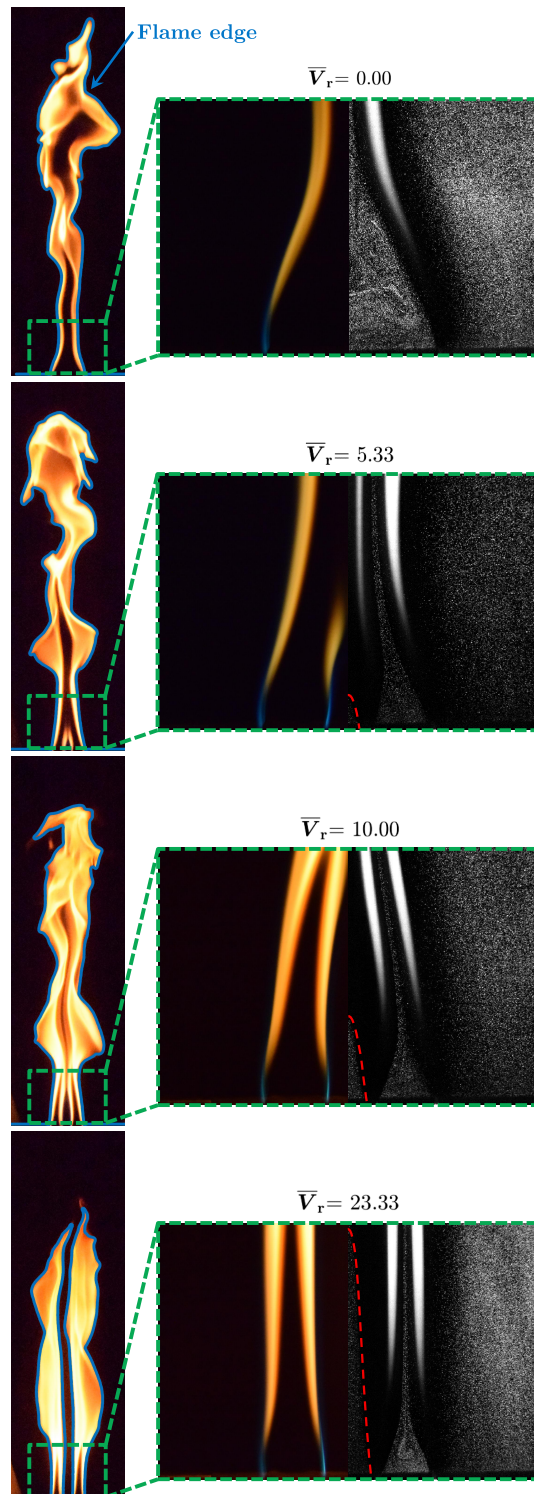


Figure 5.5: Far-field and near-field flame images by SLR and PIV cameras. Left side: whole flame images at four test conditions. The blue lines are 2D projection of the flame surface. Right side: PIV and corresponding SLR images.

As the readings of the CO₂ analyzer for cases with $\bar{V}_r > 0$ were almost equal to that of $\bar{V}_r = 0$, the overall combustion efficiency was essentially unchanged by adding inner air. The concentrations of CO₂, CO, and unburned hydrocarbons in the gaseous combustion products, which were also collected in sampling bags, were measured using a gas chromatograph to confirm the completeness of combustion with an efficiency greater than 98 % for all cases.

The right side of Fig. 5.5 displays a left-right split collage of the raw PIV field of view (right side) and the corresponding geometrically matched SLR flame image (left side). For all flames that were attached to the burner (*i.e.*, categories (i) to (iii)) the attaching flames were blue up to the height of approximately one w before transitioning into much brighter yellow-orange flames. In the raw PIV images, there are regions of the flame that remain bright despite using a narrow bandpass filter and setting a relatively short exposure time. These locations are associated with the high soot concentration within the laser sheet and are attributed to a combination of laser-induced incandescence and Mie scattering from soot particles. These bright regions are stationary features, which are incorrectly interpreted as regions of zero flow velocity by the PIV correlation. Therefore, those soot-generating regions are subtracted for post-processing and shown as blank regions. As illustrated in Fig. 5.6, these blank regions start at $-14 \leq x \leq -11.2$ mm and $17.5 \leq z \leq 22.2$ mm in the velocity field.

By focusing on the oil seeded inner air shown in Fig. 5.5, the raw PIV images also mark the isotherms at ≈ 600 K (red dashed curves) inside the inner flame, as the oil evaporated. For attached inner flames (*i.e.*, categories (i) to (iii)), the heights of these isotherms grow almost linearly by increasing \bar{V}_r as the inner air flow momentum increases. The normalized isotherm heights are reported in the last column of Table. 5.1. In each case, the region above this isotherm does not have any seeding

particles to calculate the velocity. Therefore, this region is also shown as blank in the velocity fields (Fig. 5.6). Also evident in the raw PIV images are the variations in the number density of the solid seed particles in the fuel and outer air streams. This diminished number density close to the flame fronts was due to the high heat release and lower density of products.

Figure 5.6 is a collage of the processed raw PIV images for the same four flow conditions shown in Fig. 5.5. Elements of importance in this set of figures are the magnitude of instantaneous velocities (left side), and the instantaneous streamlines (right side) selected to represent outer regions of the inner IDF (red dashed streamlines), inner regions of the outer NDF (green dash-dot streamlines), and outer regions of the outer NDF (blue dotted streamlines) within the shear-mixing layers.

With respect to the magnitude of instantaneous velocities, it is important to note that all the figures use the same color bar (dark blue to dark red is 0.0 to 1.8 m/s) so that quantitative comparisons between flow conditions can be made. The burner exit flows (or the flow field's inlet boundary conditions) for the fuel and outer air are the same for all conditions. Recall that the outer air flows extend to $x = -55$ mm and $x = +55$ mm, and it is used to help establish more consistent side (*i.e.*, x - z) boundary conditions.

When the inner air flow is non-existent ($\overline{V}_r = 0$), there is a large region extending over the fuel and inner air slots where the velocity is almost zero, as shown in Fig. 5.6 (left side), which can be seen to be a gently recirculating standing vortex pairs by viewing sequential PIV images. The upward acceleration in the flow was due to flame induced buoyancy almost immediately above the burner at the interface between the fuel and outer air (note the small black squares at $z = 0$ for wall locations at the bottom of Fig. 5.6 images). Typical of NDFs in normal gravity, despite the dilatation of gases associated with temperature rise, the flow acceleration was strong enough

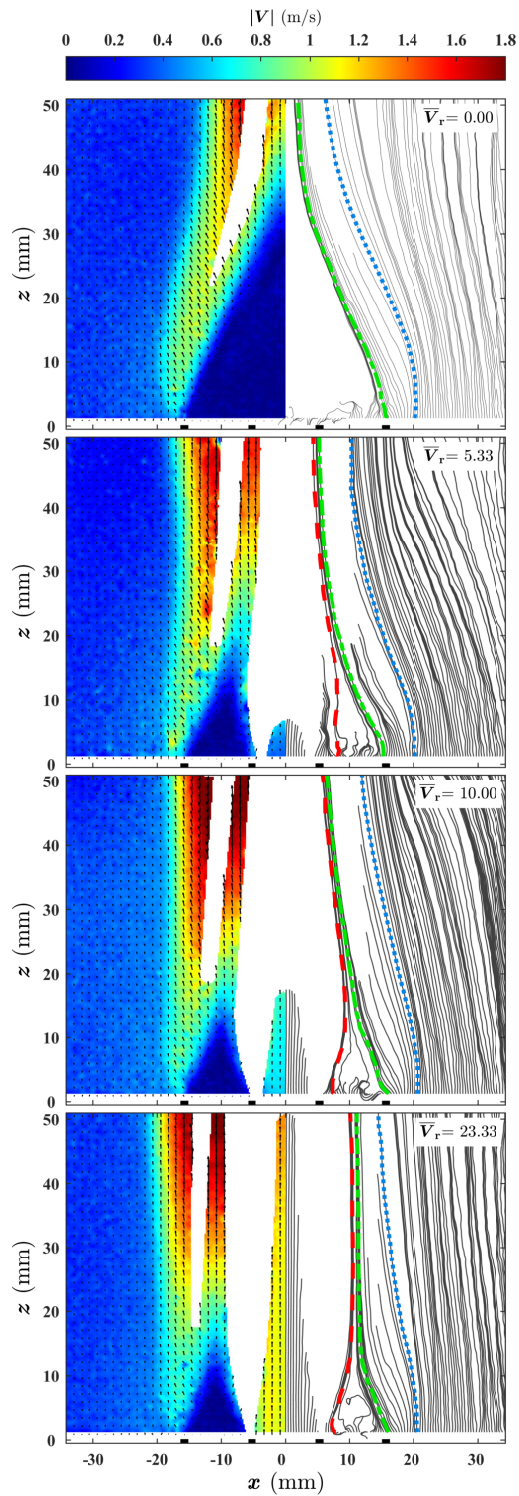


Figure 5.6: Instantaneous velocity field and streamlines at selected velocity ratios (note the description of bold streamlines in the text); the black blocks at $z = 0$ represent burner walls.

to induce the outer air to flow inward further downstream in support of combustion. The two streamlines depicted on the right side of Fig. 5.6 show the extent of this inward bending of the outer air. The first streamline (shown by a green dashed-dotted line) begins just on the air side of the wall separating the fuel and outer air (*i.e.*, $x = 15.1$ mm) and bends to end up on the inner side of the NDF's highly luminous zone (blacked out, as discussed previously) and leaves the field of view at $x = 1.9, 5.2, 6.3,$ and 11.1 mm, respectively for the four cases depicted in Fig. 5.6. The second streamline (shown by a blue dotted line) begins at $x = 21.3$ mm, and leaves the field of view on the outside of the NDF's highly luminous zone ($x = 6.2, 10.4, 11.9,$ and 14.5 mm, respectively).

Observations of the inner air flow field (seeded by canola oil) can be made up to the point where the oil reaches its evaporation temperature. Increasing the inner air velocity causes the outer air to bend less inward. Referring to Fig. 5.5, these flows formed four flame bases (two associated with NDF and two being IDF), so in that region, the rate of heat release, dilatation of gases, and subsequent upward acceleration of the flow would all be expected to be higher. This expectation for increased acceleration is supported through the appearance of higher velocity magnitudes occurring in that region, which is also a result of a higher momentum inner air jet.

For flames with the inner air, three streamlines were identified to be of interest, which are colored in Fig. 5.6 (right side). The first two (green dash-dot streamlines and blue dotted streamlines) have the same point of origin as the case of no inner air, and they end up going through a flow pattern of ending up either on the inside or the outside of the NDF. The third streamline (shown by a red dashed line) was selected from the fuel flow because its trajectory remained just on the fuel side of the IDF at the upper edge of the field of view. As a result, this third streamline invariably ends up very near and parallel to the green dash-dot streamline. As the inner air velocity

increased, the starting x -wise position of the third streamline moved progressively closer to the inner air flow. The conclusion being that as the inner air flow velocity increased a smaller portion of the fuel stream was consumed by the IDF in the field of view.

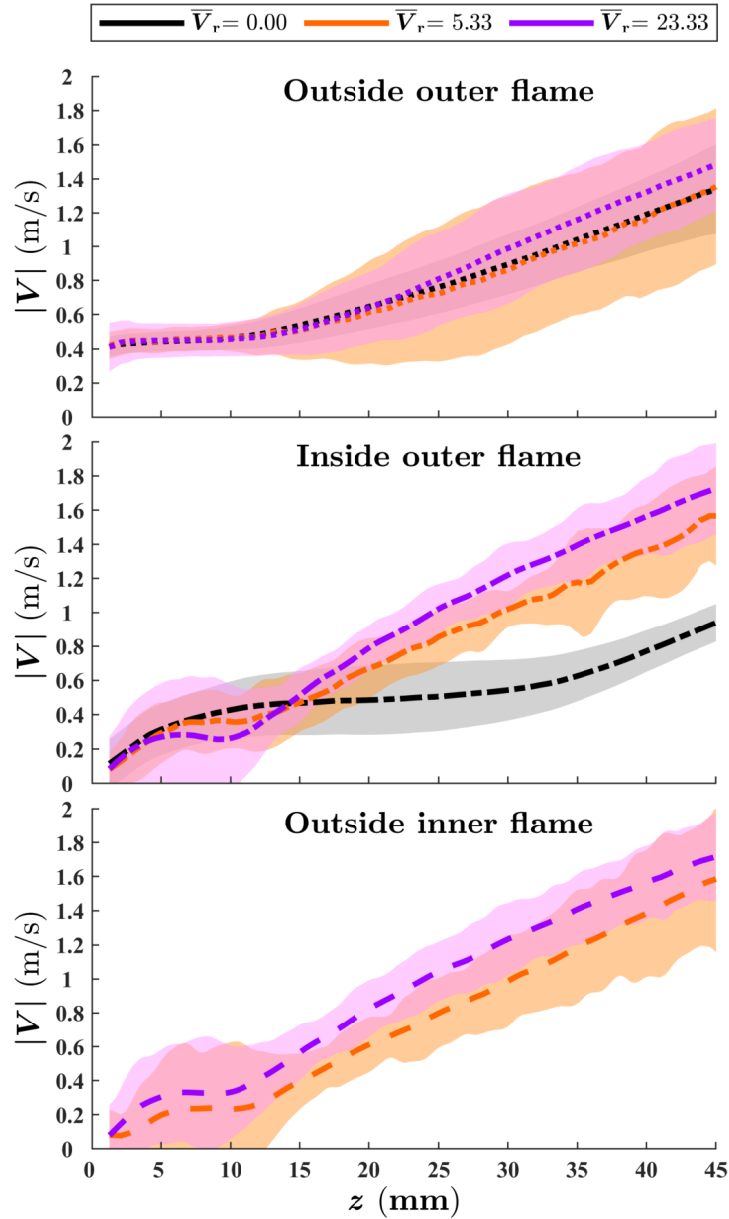


Figure 5.7: Average velocity magnitude of the streamlines indicated in Fig. 4 as a function of height above the burner with 95 % confidence bands

Figure 5.7 further explores the averaged velocity magnitudes along the representative streamlines (shown on the right side of Fig. 5.6), which start at the same location, as a function of height above the burner exit by considering 300 processed PIV image pairs for three of the inner air flow rates. The lines represent the averaged velocity magnitudes along the streamlines, while the shaded areas show the 95% confidence interval of all the velocity magnitudes. Starting with the outermost streamline (*i.e.*, furthest from the inner air flow), on the outer side of the outer flame, there is only modest impact as the inner air is increased. There is essentially no difference between the case of no inner air and the case of $\bar{V}_r = 5.33$. The impact of the $\bar{V}_r = 23.33$ is almost undetectable up to $z \approx 25$ mm, and at higher heights the difference in the magnitude of velocity is limited to 0.2 m/s.

Turning our attention to the streamline on the inner side of the outer flame, there is a modest difference in the velocities after $z \approx 5$ mm, but the velocities diverge considerably after $z \approx 15$ mm. When the inner flame exists, this portion of the flow ($z > 15$ mm) appears to experience an increased acceleration due to inner air momentum and the buoyancy associated with the inner flame. Despite the higher inner jet flow velocity being more than four times greater than the lower one (*i.e.*, $\bar{V}_r = 23.33$ compared to $\bar{V}_r = 5.33$), their velocities remain mostly parallel and separated by around 0.25 m/s. Lastly, the innermost streamline that is on the outside of the inner flame (this region does not exist for the zero inner air flow case) has similar trends but the averaged velocity magnitudes along the streamlines in the case of $\bar{V}_r = 23.33$ are always larger over their measured range. It is also worth mentioning that the velocity magnitude over streamlines inside the outer flame and outside the inner flame for $\bar{V}_r = 23.33$ are almost identical, which is in agreement with partitioning to two symmetric left and right flames in category (iii) with minimal inward bending.

Figure 5.8 shows the trends of EI_{BC} and EI_{NO_x} at different inner air-to-fuel velocity ratios, while the ranges of \bar{V}_r associated with the previously defined flame categories are drawn above it. While the EI_{NO_x} showed only modest trends of increasing and decreasing magnitude with increasing amounts of inner air, BC emissions underwent a dramatic non-monotonic change. With no inner air flow, the NDF emits BC with an emission index of approximately 3 g/kg-fuel. By adding ever-increasing amounts of inner air, there was an unexpected order of magnitude increase in EI_{BC} while progressing through the previously defined category (i) and (ii) cases. Then, for all of the category (iii) cases, the EI_{BC} remained constant at approximately 30 g/kg-fuel, which shows an order of magnitude higher BC emissions compared to the NFD case with no internal air flow. Similar trends in BC emissions were observed in a previous work (Zamani et al., 2021) where air flow was increased in air-assisted diffusion flames in a co-annular burner. Once the inner flame became lifted (category (iv)), which resulted in either one or two vertically unstable blue-colored edge-flame(s), the EI_{BC} dropped below the detection limit of the PAX.

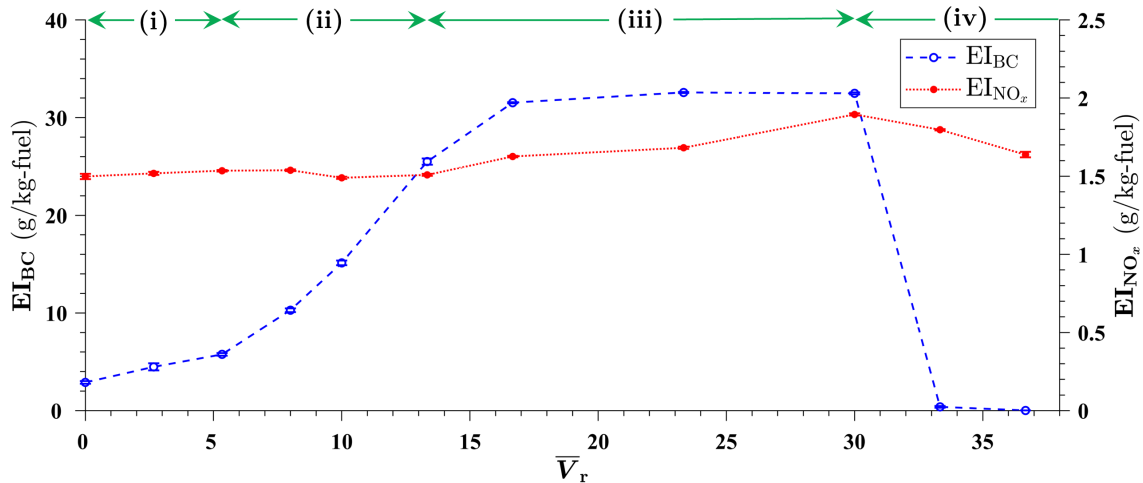


Figure 5.8: Emission indices at different velocity ratios annotated by the defined flame categories (i) to (iv).

An important conclusion is that adding more air into a diffusion flame does not necessarily have a positive effect on BC emissions. Initial thoughts have qualitatively focused on the role of products of combustion from the inner flame becoming part of the fuel flow to explain why the emission of BC responds so negatively to the introduction of air into the fuel. It is proposed that, in categories (i) and (ii), flames produce increasing amounts of hot products, intermediate species, and soot particles with increasing amounts of inner air. These intermediate species and particles, which do not have enough locally available oxygen to fully react to form CO_2 , are then entirely surrounded by a carbon-based fuel and thereby produce considerable more soot. Higher soot formation in the case of a closed-tip IDF inside an NDF (category (i)) compared to the case of zero inner air ($\bar{V}_r = 0$) is aligned with the findings in the literature Lim et al. (2017). Currently, no conceptual models are proposed for why the category (iii) cases remain high. The conjectural proposal for why lifting the IDF through increased inner air flow rates causes a near-zero emission of BC is associated with the partial premixing of fuel and air prior to combustion.

5.4 Concluding Remarks

In this study, the emissions of black carbon (BC) and oxides of nitrogen (NO_x), as well as detailed flow fields, were quantified in unconfined jet diffusion flames that had elements similar to both normal and inverse diffusion flames. A relatively novel multi-slot burner was designed to produce two-dimensional planar flames. Its geometry was a symmetric arrangement of five slots, with the outer two acting mainly as a well-defined outer boundary of air flow. Progressing inward, the next pair of slots carried the fuel while the central slot carried a flow of inner air. Reflecting upon the internally air-assisted flames, where a normal jet diffusion flame (NDF) and an inverse jet diffusion flame (IDF) coexist in close proximity, the main goal was to understand

how changes in the central air flow rate impacted the overall flow field in the vicinity of the flames and the subsequent impacts on the emissions and flame stability.

Experiments were conducted with constant fuel and outer air flow rates, while the central air flow rate was increased from zero to a magnitude that caused instabilities and flame lift-off. In all cases, two flame bases were attached to the wall in the mixing layer between the fuel stream and the outer air flow. These flames had the characteristic of an NDF and were referred to as the outer flames. With the introduction of inner air flow, two more flame bases appeared with the characteristics of an IDF and were referred to as inner flames. As the inner air flow rate was increased, the inner flame transitioned from being closed-tip, to open-tip, to partitioning the flames from the two fuel slots, to the inner flame being lifted. These transitions in the shape of the inner flame and its interactions with the outer flame were closely correlated with the emission of BC, while NO_x emissions were insensitive to the interaction of the flames caused by the inner air addition. The flame shape and inner air effects were identified in terms of the burner exit velocity ratio between the inner air and the fuel.

The BC emissions significantly changed non-monotonically from the case of no inner air to the case of inner flame lift-off. Using zero inner air as a starting point, the addition of a small amount of inner air caused a modest increase in BC emissions while being a closed tip IDF. Adding more inner air to create an open tip IDF caused the BC emissions to increase and eventually become an order of magnitude greater than the case of no inner air case. Adding more inner air to partition the inner and outer flame structure into two NDFs had no impact on the BC emission, which remained at their maximum. Finally, with yet more inner air flow, one or both of the inner flames would lift off, allowing the fuel and inner air to be partially premixed, and the BC emission dropped to values close to zero. Therefore, air addition can dramatically reduce BC emissions in an internally air-assisted flare only when partial

premixing occurs due to the inner flame lift-off. All in all, in order to reduce the overall BC emissions, the inner air flow rate needs to be high enough to lift off the inner flame and allow for fuel and air premixing. In the case of having a flame inside of a fuel stream (*i.e.* preheating fuel by the inner flame products), it is valid in general that the BC emissions represent an increasing trend at low flow rates of internal assisting air, and that the BC emissions drop significantly at higher assisting air flow rates. However, the onset of reduction in BC emissions depends on the burner geometry and test conditions.

CHAPTER 6

Conclusion and Future Work

6.1 Concluding Remarks

The scientific discussions and experimental results presented in this thesis focus on improving and deepening the current understanding of assisted flares and co-flow diffusion flames. Three connected investigations used three experimental setups with two co-annular burners and one multi-slot burner to quantify the key emissions, mainly the emission index (EI) of black carbon (BC) and oxides of nitrogen (NO_x), and the carbon conversion efficiency (CCE) of lab-scale flares and relate them to the flow field. A summary of the main concluding remarks is listed as follows.

- In co-annular burners, setting the controllable variables so that they supposedly result in a higher characteristic flame temperature, namely, introducing more oxygen in the assisting fluid, reducing the amount of steam or other diluents with lower specific heat capacities, substituting atomized water with steam, and having less radiation heat loss, increased the production of NO_x . Thus, it was concluded that a thermal mechanism adequately described the EI_{NO_x} results.

- For the cases with assisting fluid flow rate ranges from zero to that which caused flame blow-off, there was a significant disconnect between the mass flow ratio (MFR) at which the early BC suppression occurs and the one at which the CCE collapses, linked to the flame blow-off. As a result, there was a broad range of assisting fluid flow rates, where the CCE was almost 100%, while the flame luminosity and BC emissions were monotonically and ultimately being severely suppressed with increasing assisting fluid flow rates. The diminished flame luminosity was related to the flames becoming bluer for air-assisted flames and redder for steam-assisted flames; at the same time, at least an order of magnitude reduced the EI_{BC} .
- The fuel composition (*i.e.*, its heating value) has a great impact on the BC emissions at MFR=0 (no assisting fluid) and the rate at which they decreased due to co-flow addition. By increasing the MFR, EI_{BC} dropped orders of magnitude for all fuel compositions. At the same MFR, it was demonstrated that BC emissions were reduced by an order of magnitude more in water-assisted cases than in steam-assisted ones.
- As a result of the same chemical composition of steam and water, this study focused on the hydrodynamics and thermodynamics of assisting fluid addition. The results were that the overall hydrodynamics of the flame were essentially the same at low flow rates of these two assisting fluid co-flows and are governed by the buoyancy of combustion products. The buoyancy is a function of flame temperature, and the characteristic temperature of the flames was quite different. On the one hand, the fuel composition was a primary determinant of radiation heat losses, which impacted the actual peak temperature. On the other hand, due to the difference in the heat required to evaporate the liquid water and the initial feeding temperatures of water and steam, the actual peak

temperature at the same MFR was lower in the case of water addition.

- The multi-slot burner's design demonstrates a promising capacity for flame stabilization of both normal and inverse diffusion flames and their coexistence in various configurations. The slot width (length scale linked to reacting layers) and wall thickness (length scale related to initial mixing/shear layers) can be independently changed thanks to geometric flexibility.
- In the multi-slot burner, two flame bases were anchored to the wall in the mixing layer between the fuel stream and the outer air flow. The term *outer flames* was used to describe these flames, which had the characteristics of a normal diffusion flame (NDF). Two more flame bases with features of an inverse diffusion flame (IDF) formed with the addition of inner air flow and were referred to as *inner flames*. By adding more inner air, the inner flame changed from being closed-tip, to being open-tip, to partitioning the flames from the two fuel slots, to being a lifted flame. The BC emissions were closely connected to these changes in the inner flame's shape and its interaction with the outer flame. However, NO_x emissions were unaffected by the interaction of the flames brought on by the injection of inner air.
- To explain the non-monotonic trend in BC emissions in the cases of no inner air to inner flame lift-off, adding a small amount of inner air resulted in a moderate rise in BC emissions while being a closed tip IDF. More inner air made the IDF open tip, causing the BC emissions to increase and eventually exceed an order of magnitude compared to no the inner air case. Adding more inner air split the inner and outer flame structure into two NDFs, by which the BC emission remained unchanged and at its maximum. Once even more inner air was added, one or both of the inner flames lifted off, enabling the fuel and inner

air to be partially premixed, and the BC emission dropped to values below the detection limit. Therefore, air addition can dramatically reduce BC emissions in an internally air-assisted flare only when partial premixing happens as a result of the inner flame lift-off. In the case of having a flame inside a fuel stream (*i.e.* preheating fuel by inner flame products), it is generally true that BC emissions increase at low internal assisting air flow rates and decrease significantly at higher assisting air flow rates. The burner geometry and test conditions do, however, affect when BC emissions start to decline.

6.2 Future Work

Based on the investigations included in this thesis, the following is a selection of potential possibilities for future work.

- Geometry and scale play essential roles in BC and NO_x emissions; therefore, a comprehensive set of experiments needs to be conducted to extend the results of this study to full-scale industrial applications.
- By particle extraction sampling from the 2D flames on the multi-slot burner, a 2D field of particle evolution can be mapped in laminar flame sheets. Two of the extraction sampling techniques, namely probe sampling and jet-entrainment sampling, and their implications are described thoroughly in (Kazemimanesh et al., 2017; Michelsen et al., 2022), respectively. This can be achieved by taking measurements of the size distributions of the soot particles at various points on the fuel side of the flame sheets at different heights above the burner. The 2D map of soot particles, along with the 2D mean velocity field measured by particle image velocimetry (PIV), will help understand the transport of soot particles.

- Another possibility would be a non-intrusive measurement of soot volume fractions and primary particle diameters using the laser-induced incandescence (LII) diagnostic technique, which needs extra excitation and detection devices. LII is a widely-used and robust measurement technique in soot generating diffusion (non-premixed) flames (Chatterjee and Gülder, 2018; Zhang et al., 2019). If PIV and LII measurements are done simultaneously, soot volume fraction and velocity fields will be obtained.
- The geometrically flexible multi-slot burner can stabilize one to four 2D diffusion flames, which can be used to study the opacity of one to four parallel flames attached to the divider plates along the long side. This can determine if the flames are optically thin or thick as well as the contribution of each flame.
- Adding steam instead of the inner air in the multi-slot burner, while the whole burner needs to be preheated to avoid steam condensation in the slot. In this case, only fuel and outer air can be seeded, preferably with solid particles, to perform PIV measurements to study steam and fuel mixing layers. This will mimic the flow configuration of internally steam-assisted flames.

REFERENCE

- Abbasi-Atibeh, E. and Bergthorson, J. M. (2019). The effects of differential diffusion in counter-flow premixed flames with dilution and hydrogen enrichment. *Combust. Flame*, 209:337–352. <https://doi.org/10.1016/j.combustflame.2019.07.035>.
- Abernethy, R. B., Benedict, R. P., and Dowdell, R. B. (1985). ASME Measurement Uncertainty. *J. Fluids Eng.*, 107(2):161–164. <https://doi.org/10.1115/1.3242450>.
- AER (2016). Directive 060: Upstream petroleum industry flaring, incinerating, and venting. Technical report, Alberta Energy Regulator.
- Ahsan, A., Ahsan, H., Olfert, J. S., and Kostiuik, L. W. (2019). Quantifying the carbon conversion efficiency and emission indices of a lab-scale natural gas flare with internal coflows of air or steam. *Exp. Therm. Fluid. Sci.*, 103:133–142. <https://doi.org/10.1016/j.expthermflusci.2019.01.013>.
- Alhameedi, H. A., Hassan, A. A., and Smith, J. D. (2022). Towards a better air assisted flare design for low flow conditions: Analysis of radial slot and flow effects. *Process Saf. Environ. Prot.*, 157:484–492. <https://doi.org/10.1016/j.psep.2021.11.007>.
- ANSI/API (2008). Petroleum, petrochemical and natural gas industries—Flare de-

- tails for general refinery and petrochemical service. Technical Report ANSI/API STANDARD 537, American Petroleum Institute (API), Washington, D.C., USA.
- Anufriev, I. and Kopyev, E. (2019). Diesel fuel combustion by spraying in a superheated steam jet. *Fuel Process. Technol.*, 192:154–169. <https://doi.org/10.1016/j.fuproc.2019.04.027>.
- API (2014). Pressure-relieving and depressuring systems. Technical Report API STANDARD 521, American Petroleum Institute (API), Washington, D.C., USA.
- Aye, I. and Wingate, E. O. (2019). Nigeria’s flare gas (prevention of waste & pollution) regulations 2018. *Environ. Law Rev.*, 21(2):119–127. <https://doi.org/10.1177/1461452919838264>.
- Baukal, C. (2005). Everything you need to know about NO_x: Controlling and minimizing pollutant emissions is critical for meeting air quality regulations. *Met. Finish.*, 103(11):18–24. [https://doi.org/10.1016/S0026-0576\(05\)80816-5](https://doi.org/10.1016/S0026-0576(05)80816-5).
- Baukal Jr, C. E. (2001). *The john zink combustion handbook*. CRC Press, New York, USA.
- Baukal Jr, C. E. (2013). *The John Zink Hamworthy Combustion Handbook: Volume 2 Design and Operations (2nd ed.)*. CRC Press, New York, USA. <https://doi.org/10.1201/b13893>.
- Blevins, L. G., Fletcher, R. A., Benner Jr, B. A., Steel, E. B., and Mulholland, G. W. (2002). The existence of young soot in the exhaust of inverse diffusion flames. *Proc. Combust. Inst.*, 29(2):2325–2333. [https://doi.org/10.1016/S1540-7489\(02\)80283-8](https://doi.org/10.1016/S1540-7489(02)80283-8).
- Bond, T. C. and Bergstrom, R. W. (2006). Light absorption by carbonaceous particles:

- An investigative review. *Aerosol Sci. Technol.*, 40(1):27–67. <https://doi.org/10.1080/02786820500421521>.
- Bond, T. C., Doherty, S. J., Fahey, D. W., Forster, P. M., Berntsen, T., DeAngelo, B. J., Flanner, M. G., Ghan, S., Kärcher, B., Koch, D., et al. (2013). Bounding the role of black carbon in the climate system: A scientific assessment. *J. Geophys. Res. Atmos.*, 118(11):5380–5552. <https://doi.org/10.1002/jgrd.50171>.
- Brzustowski, T. A. (1976). Flaring in the energy industry. *Prog. Energy Combust. Sci.*, 2(3):129–141. [https://doi.org/10.1016/0360-1285\(76\)90009-5](https://doi.org/10.1016/0360-1285(76)90009-5).
- Bussman, W. and Knott, D. (2000). Unique concept for noise and radiation reduction in high-pressure flaring. In *Offshore Technology Conference*. OnePetro. <https://doi.org/10.4043/12160-MS>.
- Castiñeira, D. and Edgar, T. F. (2006). CFD for simulation of steam-assisted and air-assisted flare combustion systems. *Energ. Fuel*, 20(3):1044–1056. <https://doi.org/10.1021/ef050332v>.
- Chatterjee, S. and Gülder, Ö. L. (2018). Soot concentration and primary particle size in swirl-stabilized non-premixed turbulent flames of ethylene and air. *Experimental Thermal and Fluid Science*, 95:73–80. <https://doi.org/10.1016/j.expthermflusci.2018.01.035>.
- Chelliah, H., Law, C. K., Ueda, T., Smooke, M., and Williams, F. (1991). An experimental and theoretical investigation of the dilution, pressure and flow-field effects on the extinction condition of methane-air-nitrogen diffusion flames. In *Symposium (International) on Combustion*, volume 23, pages 503–511. Elsevier. [https://doi.org/10.1016/S0082-0784\(06\)80297-3](https://doi.org/10.1016/S0082-0784(06)80297-3).

- Cheremisinoff, N. P. (2013). *Industrial gas flaring practices*. John Wiley & Sons, NJ, USA.
- Chomiak, J. (1990). *Combustion a study in theory, fact and application*. Philadelphia, PA (USA); Abacus Press.
- Cloy, J. M., Smith, K. A., DellaSala, D. A., and Goldstein, M. I. (2017). Greenhouse gas sources and sinks. In *Encyclopedia of the Anthropocene*, pages 391–400. Elsevier Academic Press. <https://doi.org/10.1016/B978-0-12-409548-9.09961-9>.
- Cohen, E. R. (1998). An introduction to error analysis: The study of uncertainties in physical measurements. <https://doi.org/10.1088/0957-0233/9/6/022>.
- Corbin, D. J. and Johnson, M. R. (2014). Detailed expressions and methodologies for measuring flare combustion efficiency, species emission rates, and associated uncertainties. *Ind. Eng. Chem. Res.*, 53(49):19359–19369. <https://doi.org/10.1021/ie502914k>.
- Devesh Singh, K., Gangadharan, P., Dabade, T., Shinde, V., Chen, D., Lou, H. H., Richmond, P. C., and Li, X. (2014). Parametric study of ethylene flare operations using numerical simulation. *Eng. Appl. Comput. Fluid Mech.*, 8(2):211–228. <https://doi.org/10.1080/19942060.2014.11015508>.
- Dong, L., Cheung, C. S., and Leung, C. W. (2007). Heat transfer characteristics of an impinging inverse diffusion flame jet – Part I: Free flame structure. *Int. J. Heat Mass Transf.*, 50(25-26):5108–5123. <https://doi.org/10.1016/j.ijheatmasstransfer.2007.07.018>.
- Driscoll, J. F., Sutkus, D., Roberts, W. L., Post, M., and R GOSS, L. (1994). The strain exerted by a vortex on a flame—determined from velocity field im-

- ages. *Combust. Sci. Technol.*, 96(4-6):213–229. <https://doi.org/10.1080/00102209408935356>.
- Dryer, F. (1977). Water addition to practical combustion systems—concepts and applications. *Symp. (Int.) Combust.*, 16(1):279–295. [https://doi.org/10.1016/S0082-0784\(77\)80332-9](https://doi.org/10.1016/S0082-0784(77)80332-9).
- Duck, B. (2011). Reducing emissions in plant flaring operations. *Hydrocarbon World*, 6(1)(1):42–45.
- Elbaz, A. M. and Roberts, W. L. (2014). Experimental characterization of methane inverse diffusion flame. *Combust. Sci. Technol.*, 186(9):1249–1272. <https://doi.org/10.1080/00102202.2014.920835>.
- Elbaz, A. M. and Roberts, W. L. (2016). Experimental study of the inverse diffusion flame using high repetition rate OH/acetone PLIF and PIV. *Fuel*, 165:447–461. <https://doi.org/10.1016/j.fuel.2015.10.096>.
- Elvidge, C. D., Bazilian, M. D., Zhizhin, M., Ghosh, T., Baugh, K., and Hsu, F.-C. (2018). The potential role of natural gas flaring in meeting greenhouse gas mitigation targets. *Energy strateg. Rev.*, 20:156–162. <https://doi.org/10.1016/j.esr.2017.12.012>.
- Elvidge, C. D., Zhizhin, M., Baugh, K., Hsu, F.-C., and Ghosh, T. (2016). Methods for global survey of natural gas flaring from visible infrared imaging radiometer suite data. *Energies*, 9(1):14. <https://doi.org/10.3390/en9010014>.
- EPA (2012). Parameters for properly designed and operated flares. Technical report, US Environmental Protection Agency (EPA) Office of Air Quality Planning and Standards (OAQPS), Washington, D.C., USA.

- Ergun, S. (1952). Fluid flow through packed columns. *Chem. Eng. Prog.*, 48:89–94.
- Escudero, A. I., Aznar, M., Díez, L. I., Mayoral, M. C., and Andrés, J. M. (2020). From O₂/CO₂ to O₂/H₂O combustion: The effect of large steam addition on anthracite ignition, burnout and NO_x formation. *Fuel Process. Technol.*, 206:106432. <https://doi.org/10.1016/j.fuproc.2020.106432>.
- Fawole, O. G., Cai, X.-M., and MacKenzie, A. R. (2016). Gas flaring and resultant air pollution: A review focusing on black carbon. *Environ. Pollut.*, 216:182–197. <https://doi.org/10.1016/j.envpol.2016.05.075>.
- GGFRI (2004). Regulation of associated gas flaring and venting—a global overview and lessons from international experience: Report no. 3. Technical report, Global Gas Flaring Reduction Initiative, World Bank. https://www.esmap.org/sites/default/files/esmap-files/Rpt_GBL_RegOfGasFlaringandVenting.pdf (accessed May 01, 2020).
- GGFRP (2022). 2022 global gas flaring tracker report. Technical report, Global Gas Flaring Reduction Partnership (GGFRP), World Bank, Washington, DC, USA. <https://thedocs.worldbank.org/en/doc/1692f2ba2bd6408db82db9eb3894a789-0400072022/original/2022-Global-Gas-Flaring-Tracker-Report.pdf> (accessed July 01, 2022).
- Glaude, P.-A., Fournet, R., Bounaceur, R., and Molière, M. (2010). Adiabatic flame temperature from biofuels and fossil fuels and derived effect on NO_x emissions. *Fuel Process. Technol.*, 91(2):229–235. <https://doi.org/10.1016/j.fuproc.2009.10.002>.
- Guojiang, W. and Song, T. (2005). Cfd simulation of the effect of upstream flow distribution on the light-off performance of a catalytic converter. *Energy Convers.*

- Manag.*, 46(13-14):2010–2031. <https://doi.org/10.1016/j.enconman.2004.11.001>.
- Gvakharia, A., Kort, E. A., Brandt, A., Peischl, J., Ryerson, T. B., Schwarz, J. P., Smith, M. L., and Sweeney, C. (2017). Methane, black carbon, and ethane emissions from natural gas flares in the Bakken Shale, North Dakota. *Environ. Sci. Technol.*, 51(9):5317–5325. <https://doi.org/10.1021/acs.est.6b05183>.
- Hargrave, G., Jarvis, S., and Williams, T. (2002). A study of transient flow turbulence generation during flame/wall interactions in explosions. *Measurement Science and Technology*, 13(7):1036. <https://doi.org/10.1088/0957-0233/13/7/310>.
- Hinvest, W. C. A. (1964). Apparatus for reducing smoke emission from elevated flare stacks. US Patent 3,162,236, <https://patentimages.storage.googleapis.com/7d/72/8d/ebbf8b93a8bfee/US3162236.pdf>.
- Hong, J., Wilkins, J., White, J. W., and Poe, R. L. (2006). Flare apparatus. US7967600B2, <https://patents.google.com/patent/US7967600B2/en>.
- IEA (2019). *World Energy Outlook 2019*. International Energy Agency (IEA), World Energy Outlook Series. OECD. <https://iea.blob.core.windows.net/assets/98909c1b-aabc-4797-9926-35307b418cdb/WE02019-free.pdf>.
- Ismail, O. S. and Umukoro, G. E. (2016). Modelling combustion reactions for gas flaring and its resulting emissions. *J. King Saud Univ., Eng. Sci.*, 28(2):130–140. <https://doi.org/10.1016/j.jksues.2014.02.003>.
- Jacobson, M. Z. (2007). Testimony for the hearing on black carbon and global warming, House Committee on Oversight and Government Reform, United States House of Representatives. Technical report, Stanford University, CA, USA.

- Jefferson, A. M. (2017). Exploratory experiments to determine effects of injected aerosolized water, hydrochloric acid, and sodium chloride solutions on lab-scale flare emissions. Master's thesis, Carleton University.
- Johnson, M. R., Devillers, R. W., and Thomson, K. A. (2011). Quantitative field measurement of soot emission from a large gas flare using Sky-LOSA. *Environ. Sci. Technol.*, 45(1):345–350. <https://doi.org/10.1021/es102230y>.
- Johnson, M. R. and Kostiuik, L. W. (2000). Efficiencies of low-momentum jet diffusion flames in crosswinds. *Combust. Flame*, 123(1-2):189–200. [https://doi.org/10.1016/S0010-2180\(00\)00151-6](https://doi.org/10.1016/S0010-2180(00)00151-6).
- Johnson, M. R., Wilson, D. J., and Kostiuik, L. W. (2001). A fuel stripping mechanism for wake-stabilized jet diffusion flames in crossflow. *Combust. Sci. Technol.*, 169(1):155–174. <https://doi.org/10.1080/00102200108907844>.
- Kapusta, Ł. J., Shuang, C., Aldén, M., and Li, Z. (2020). Structures of inverse jet flames stabilized on a coaxial burner. *Energy*, 193:116757. <https://doi.org/10.1016/j.energy.2019.116757>.
- Karnani, S. and Dunn-Rankin, D. (2013). Visualizing CH* chemiluminescence in sooting flames. *Combust. Flame*, 160(10):2275–2278. <https://doi.org/10.1016/j.combustflame.2013.05.002>.
- Kazemimanesh, M., Moallemi, A., Olfert, J. S., and Kostiuik, L. W. (2017). Probe sampling to map and characterize nanoparticles along the axis of a laminar methane jet diffusion flame. *Proceedings of the Combustion Institute*, 36(1):881–888. <https://doi.org/10.1016/j.proci.2016.06.169>.
- Kent, J., Jander, H., and Wagner, H. G. (1981). Soot formation in a laminar diffu-

- sion flame. *Symp. (Int.) Combust.*, 18(1):1117–1126. [https://doi.org/10.1016/S0082-0784\(81\)80116-6](https://doi.org/10.1016/S0082-0784(81)80116-6).
- Kleinstreuer, C. (2018). *Modern fluid dynamics*. Springer.
- Kohketsu, S., Mori, K., Sakai, K., and Nakagawa, H. (1996). Reduction of exhaust emission with new water injection system in a diesel engine. *SAE trans.*, pages 74–81. <https://doi.org/10.4271/960033>.
- Landrigan, P. J., Fuller, R., Acosta, N. J., Adeyi, O., Arnold, R., Baldé, A. B., Bertollini, R., Bose-O’Reilly, S., Boufford, J. I., Breyse, P. N., et al. (2018). The lancet commission on pollution and health. *The lancet*, 391(10119):462–512. [https://doi.org/10.1016/S0140-6736\(17\)32345-0](https://doi.org/10.1016/S0140-6736(17)32345-0).
- Leary, K., Knott, D., and Thompson, R. (2002). Water-injected flare tips reduce radiated heat, noise. *Oil & gas journal*, 100(18):76–85.
- Lelieveld, J., Crutzen, P. J., and Brühl, Ch. (1993). Climate effects of atmospheric methane. *Chemosphere*, 26(1-4):739–768. [https://doi.org/10.1016/0045-6535\(93\)90458-H](https://doi.org/10.1016/0045-6535(93)90458-H).
- Lewis, G., Cantwell, B., and Lecuona, A. (1987). The use of particle tracking to obtain planar velocity measurements in an unsteady laminar diffusion flame. Technical report, Combustion Institute, Northridge, CA.
- Lim, S., Ahn, T., Lee, S., and Park, S. (2017). Optical measurement of volume fraction and organic mass fraction of ultra-fine soot particles emitted from inverse diffusion flames. *Fuel*, 210:455–462. <https://doi.org/10.1016/j.fuel.2017.08.113>.
- Mansour, M. S. (2000). A concentric flow conical nozzle burner for highly stabilized partially premixed flames. *Combust. Sci. Technol.*, 152(1):115–145. <https://doi.org/10.1080/00102200008952130>.

- McBride, B. J. (1996). *Computer program for calculation of complex chemical equilibrium compositions and applications*, volume 2. NASA Lewis Research Center.
- McDaniel, M. and Tichenor, B. A. (1983). Flare efficiency study. Technical Report EPA-600/2-83-052, US Environmental Protection Agency (EPA) Office of Research and Development, Washington, D.C., USA.
- Michelsen, H. A., Boigné, E., Schrader, P. E., Johansson, K. O., Campbell, M. F., Bambha, R. P., and Ihme, M. (2022). Jet-entrainment sampling: A new method for extracting particles from flames. *Proceedings of the Combustion Institute*. <https://doi.org/10.1016/j.proci.2022.07.140>.
- Miguel, R., Talebi-Moghaddam, S., Zamani, M., Turcotte, C., and Daun, K. (2021). Assessing flare combustion efficiency using imaging fourier transform spectroscopy. *J. Quant. Spectrosc. Radiat. Transf.*, 273:107835. <https://doi.org/10.1016/j.jqsrt.2021.107835>.
- Mobaseri, S. (2021). Quantifying emissions and flame geometry of lab-scale air-assisted flares. Master's thesis, University of Alberta.
- Moosmüller, H., Chakrabarty, R. K., and Arnott, W. P. (2009). Aerosol light absorption and its measurement: A review. *J. Quant. Spectrosc. Radiat. Transfer*, 110(11):844–878. <https://doi.org/10.1016/j.jqsrt.2009.02.035>.
- Müller, A. and Wittig, S. (1994). Experimental study on the influence of pressure on soot formation in a shock tube. In *Soot Formation in Combustion*, pages 350–370. Springer. https://doi.org/10.1007/978-3-642-85167-4_20.
- Muntean, V. and Higuera, F. (2016). Lean methane-air flames propagating upward in vertical tubes. *Combustion Science and Technology*, 188(4-5):818–830. <https://doi.org/10.1080/00102202.2016.1139411>.

- Oh, K. C., Do Lee, U., Shin, H. D., and Lee, E. J. (2005). The evolution of incipient soot particles in an inverse diffusion flame of ethene. *Combust. Flame*, 140(3):249–254. <https://doi.org/10.1016/j.combustflame.2004.12.002>.
- Om Ariara Guhan, C., Arthanareeswaran, G., Varadarajan, K., and Krishnan, S. (2016). Numerical optimization of flow uniformity inside an under body-oval substrate to improve emissions of ic engines. *J. Comput. Des. Eng.*, 3(3):198–214. <https://doi.org/10.1016/j.jcde.2016.02.001>.
- Ouf, F.-X., Vendel, J., Coppalle, A., Weill, M., and Yon, J. (2008). Characterization of soot particles in the plumes of over-ventilated diffusion flames. *Combust. Sci. Technol.*, 180(4):674–698. <https://doi.org/10.1080/00102200701839154>.
- Pešić, R., Kaluđerović-Radoičić, T., Bošković-Vragolović, N., Arsenijević, Z., and Grbavčić, Ž. (2015). Pressure drop in packed beds of spherical particles at ambient and elevated air temperatures. *Chem. Ind. Chem. Eng. Q.*, 21(3):419–427. <https://doi.org/10.2298/CICEQ140618044P>.
- Pitts, W. M. (1995). The global equivalence ratio concept and the formation mechanisms of carbon monoxide in enclosure fires. *Prog. Energy Combust. Sci.*, 21(3):197–237. https://tsapps.nist.gov/publication/get_pdf.cfm?pub_id=911660.
- Pohl, J. H., Tichenor, B. A., Lee, J., and Payne, R. (1986). Combustion efficiency of flares. *Combust. Sci. Technol.*, 50(4-6):217–231. <https://doi.org/10.1080/00102208608923934>.
- Ramanathan, V. and Carmichael, G. (2008). Global and regional climate changes due to black carbon. *Nat. Geosci.*, 1(4):221–227. <https://doi.org/10.1038/ngeo156>.
- Roberts, C. E., Naegeli, D., and Chadwell, C. (2005). The effect of water on soot

- formation chemistry. *SAE trans.*, pages 1656–1672. <https://doi.org/10.4271/2005-01-3850>.
- Scharnowski, S. and Kähler, C. J. (2020). Particle image velocimetry-classical operating rules from today’s perspective. *Optics and Lasers in Engineering*, 135:106185. <https://doi.org/10.1016/j.optlaseng.2020.106185>.
- Schnelle Jr, K. B., Dunn, R. F., and Ternes, M. E. (2015). *Air pollution control technology handbook*. CRC press, New York, USA. <https://doi.org/10.1201/b19286>.
- Serrano, J., Jiménez-Espadafor, F., Lora, A., Modesto-López, L., Gañán-Calvo, A., and López-Serrano, J. (2019). Experimental analysis of NO_x reduction through water addition and comparison with exhaust gas recycling. *Energy*, 168:737–752. <https://doi.org/10.1016/j.energy.2018.11.136>.
- Shi, Y., Ji, Y., Sun, H., Hui, F., Hu, J., Wu, Y., Fang, J., Lin, H., Wang, J., Duan, H., et al. (2015). Nanoscale characterization of pm 2.5 airborne pollutants reveals high adhesiveness and aggregation capability of soot particles. *Sci. Rep.*, 5:11232. <https://doi.org/10.1038/srep11232>.
- Sidebotham, G. W. and Glassman, I. (1992). Flame temperature, fuel structure, and fuel concentration effects on soot formation in inverse diffusion flames. *Combust. Flame*, 90(3-4):269–283. [https://doi.org/10.1016/0010-2180\(92\)90088-7](https://doi.org/10.1016/0010-2180(92)90088-7).
- Smyth, K. C., Miller, J. H., Dorfman, R. C., Mallard, W. G., and Santoro, R. J. (1985). Soot inception in a methane/air diffusion flame as characterized by detailed species profiles. *Combust. Flame*, 62(2):157–181. [https://doi.org/10.1016/0010-2180\(85\)90143-9](https://doi.org/10.1016/0010-2180(85)90143-9).

- Sobiesiak, A. and Wenzell, J. C. (2005). Characteristics and structure of inverse flames of natural gas. *Proc. Combust. Inst.*, 30(1):743–749. <https://doi.org/10.1016/j.proci.2004.08.173>.
- Solomon, S., Plattner, G. K., Knutti, R., and Friedlingstein, P. (2009). Irreversible climate change due to carbon dioxide emissions. *Proc. Natl. Acad. Sci.*, 106(6):1704–1709. <https://doi.org/10.1073/pnas.0812721106>.
- Stella, A., Guj, G., Kompenhans, J., Raffel, M., and Richard, H. (2001). Application of particle image velocimetry to combusting flows: design considerations and uncertainty assessment. *Exp. Fluids*, 30(2):167–180. <https://doi.org/10.1007/s003480000151>.
- Stohl, A., Klimont, Z., Eckhardt, S., Kupiainen, K., Shevchenko, V. P., Kopeikin, V., and Novigatsky, A. (2013). Black carbon in the arctic: the underestimated role of gas flaring and residential combustion emissions. *Atmospheric Chemistry and Physics*, 13(17):8833–8855. <https://doi.org/10.5194/acp-13-8833-2013>.
- Stone, D. K., Lynch, S. K., Pandullo, R. F., Evans, L. B., and Vatauvuk, W. M. (1992a). Flares. part i: Flaring technologies for controlling voc-containing waste streams. *J. Air Waste Manage. Assoc.*, 42(3):333–340. <https://doi.org/10.1080/10473289.1992.10466996>.
- Stone, D. K., Lynch, S. K., Pandullo, R. F., Evans, L. B., and Vatauvuk, W. M. (1992b). Flares. part ii. capital and annual costs. *J. Air Waste Manage. Assoc.*, 42(4):488–493. <https://doi.org/10.1080/10473289.1992.10467008>.
- Stroscher, M. T. (2000). Characterization of emissions from diffusion flare systems. *J. Air Waste Manage. Assoc.*, 50(10):1723–1733. <https://doi.org/10.1080/10473289.2000.10464218>.

- Sunderland, P., Mendelson, B., Yuan, Z.-G., and Urban, D. (1999). Shapes of buoyant and nonbuoyant laminar jet diffusion flames. *Combust. Flame*, 116(3):376–386. [https://doi.org/10.1016/S0010-2180\(98\)00045-5](https://doi.org/10.1016/S0010-2180(98)00045-5).
- Sussman (2017). *MBA 3-20 kW, 15 & 100 PSIG*. Sussman Electric Boilers, A Division of Sussman-Automatic Corporation. <http://http://sussmanboilers.com/downloads> (accessed Aug 29, 2020).
- Sze, L. K., Cheung, C. S., and Leung, C. W. (2006). Appearance, temperature, and NO_x emission of two inverse diffusion flames with different port design. *Combust. Flame*, 144(1-2):237–248. <https://doi.org/10.1016/j.combustflame.2005.07.008>.
- Tolocka, M. P., Richardson, P. B., and Miller, J. H. (1999). The effect of global equivalence ratio and postflame temperature on the composition of emissions from laminar ethylene/air diffusion flames. *Combust. Flame*, 118(4):521–536. [https://doi.org/10.1016/S0010-2180\(99\)00025-5](https://doi.org/10.1016/S0010-2180(99)00025-5).
- Torres, V. M., Herndon, S., and Allen, D. T. (2012). Industrial flare performance at low flow conditions: Part 2. steam- and air-assisted flares. *Ind. Eng. Chem. Res.*, 51(39):12569–12576. <https://doi.org/10.1021/ie202675f>.
- Trivanovic, U., Sipkens, T. A., Kazemimanesh, M., Baldelli, A., Jefferson, A. M., Conrad, B. M., Johnson, M. R., Corbin, J. C., Olfert, J. S., and Rogak, S. N. (2020). Morphology and size of soot from gas flares as a function of fuel and water addition. *Fuel*, 279:118478. <https://doi.org/10.1016/j.fuel.2020.118478>.
- Tropea, C., Yarin, A. L., Foss, J. F., et al. (2007). *Springer handbook of experimental fluid mechanics*, volume 1. Springer. <https://doi.org/10.1007/978-3-540-30299-5>.

- Turns, S. R. et al. (2000). *An introduction to combustion: concepts and applications*. McGraw-Hill Companies New York, NY, USA.
- US Government Publishing Office (2018). Requirements for flare control devices. Technical report, US Government Publishing Office. <https://www.govinfo.gov/content/pkg/CFR-2018-title40-vol112/xml/CFR-2018-title40-vol112-sec63-670.xml> (accessed July 31, 2020).
- Wagner, S., Fisher, B. T., Fleming, J. W., and Ebert, V. (2009). TDLAS-based in situ measurement of absolute acetylene concentrations in laminar 2D diffusion flames. *Proc. Combust. Inst.*, 32(1):839–846. <https://doi.org/10.1016/j.proci.2008.05.087>.
- Walsh, K. T., Long, M. B., Tanoff, M. A., and Smooke, M. D. (1998). Experimental and computational study of CH, CH*, and OH* in an axisymmetric laminar diffusion flame. *Symp. (Int.) Combust.*, 27(1):615–623. [https://doi.org/10.1016/S0082-0784\(98\)80453-0](https://doi.org/10.1016/S0082-0784(98)80453-0).
- Wang, Q., Darabkhani, H. G., Chen, L., and Zhang, Y. (2012). Vortex dynamics and structures of methane/air jet diffusion flames with air coflow. *Exp. Therm. Fluid Sci.*, 37:84–90. <https://doi.org/10.1016/j.expthermflusci.2011.10.006>.
- Weyant, C. L., Shepson, P. B., Subramanian, R., Cambaliza, M. O., Heimbürger, A., McCabe, D., Baum, E., Stirm, B. H., and Bond, T. C. (2016). Black carbon emissions from associated natural gas flaring. *Environ. Sci. Technol.*, 50(4):2075–2081. <https://doi.org/10.1021/acs.est.5b04712>.
- Wolfhard, H. and Parker, W. (1949). A new technique for the spectroscopic examination of flames at normal pressures. *Proc. Phys. Soc., A*, 62(11):722. <https://doi.org/10.1088/0370-1298/62/11/305>.

- Ying, Y. and Liu, D. (2018). Nanostructure evolution and reactivity of nascent soot from inverse diffusion flames in CO₂, N₂, and He atmospheres. *Carbon*, 139:172–180. <https://doi.org/10.1016/j.carbon.2018.06.047>.
- Zamani, M., Abbasi-Atibeh, E., Mobaseri, S., Ahsan, H., Ahsan, A., Olfert, J., and Kostiuk, L. (2021). An experimental study on the carbon conversion efficiency and emission indices of air and steam co-flow diffusion jet flames. *Fuel*, 287:119534. <https://doi.org/10.1016/j.fuel.2020.119534>.
- Zeng, Y., Morris, J., and Dombrowski, M. (2016). Validation of a new method for measuring and continuously monitoring the efficiency of industrial flares. *J. Air Waste Manage. Assoc.*, 66(1):76–86. <https://doi.org/10.1080/10962247.2015.1114045>.
- Zhang, T., Guo, Q., Song, X., Zhou, Z., and Yu, G. (2012). The chemiluminescence and structure properties of normal/inverse diffusion flames. *J. Spectrosc.*, 2013. <https://doi.org/10.1155/2013/304717>.
- Zhang, W., Thompson, K. E., Reed, A. H., and Beenken, L. (2006). Relationship between packing structure and porosity in fixed beds of equilateral cylindrical particles. *Chem. Eng. Sci.*, 61(24):8060–8074. <https://doi.org/10.1016/j.ces.2006.09.036>.
- Zhang, Y., Liu, F., Clavel, D., Smallwood, G. J., and Lou, C. (2019). Measurement of soot volume fraction and primary particle diameter in oxygen enriched ethylene diffusion flames using the laser-induced incandescence technique. *Energy*, 177:421–432. <https://doi.org/10.1016/j.energy.2019.04.062>.
- Zhao, D., Yamashita, H., Kitagawa, K., Arai, N., and Furuhashi, T. (2002). Behavior and effect on NO_x formation of OH radical in methane-air diffusion flame with

steam addition. *Combust. Flame*, 130(4):352–360. [https://doi.org/10.1016/S0010-2180\(02\)00385-1](https://doi.org/10.1016/S0010-2180(02)00385-1).

Zhen, H., Wei, Z., Liu, X., Liu, Z., Wang, X., Huang, Z., and Leung, C. (2021). A state-of-the-art review of lab-scale inverse diffusion burners & flames: From laminar to turbulent. *Fuel Process. Technol.*, 222:106940. <https://doi.org/10.1016/j.fuproc.2021.106940>.

Zhen, H. S., Choy, Y. S., Leung, C. W., and Cheung, C. S. (2011). Effects of nozzle length on flame and emission behaviors of multi-fuel-jet inverse diffusion flame burner. *Appl. Energy*, 88(9):2917–2924. <https://doi.org/10.1016/j.apenergy.2011.02.040>.

APPENDIX A

Uncertainty Calculation

A.1 Definition

This appendix will describe how to calculate the uncertainty in an experimental measurement based on ASME measurement uncertainty (Abernethy et al., 1985), but first a few terms must be defined. The difference between the true and measured values is defined as the *error*. Knowing the true value of a quantity is not possible, so its measurement error cannot be known. Instead, the goal is to determine the *uncertainty* in a measured value estimating the true value. The uncertainty refers to the error estimate with a specific confidence interval (Cohen, 1998) expressed as a probability. Two types of uncertainty are defined by the International Standards Organization (ISO):

- (1) Precision uncertainty (P_x): the uncertainty estimated from the data, associated with the repeatability of the recorded quantity, is known as *precision* or *repeatability* uncertainty.
- (2) Bias uncertainty (B_x): the uncertainty that can't be inferred from the data

and is inherent to the measurement device or technique, which is known as *systematic* or *bias* uncertainty.

The total uncertainty (U_x) in a measurement is calculated from:

$$U_x = \sqrt{P_x^2 + B_x^2} \quad (\text{A.1})$$

A.1.1 Precision Uncertainty (P_x)

By doing multiple repetitions of the same measurement and using statistical analysis, precision uncertainty can be calculated. For instance, in this study, the output data from emission measurement devices was recorded for 2 to 3 min with a logging frequency of 1 Hz, generating 120 to 180 data points for each measured quantity in each test case. Given the sample size in this study, precision uncertainty can be calculated based on the central limit theorem (Abernethy et al., 1985) as follows:

$$P_x = z_{c/2} \frac{\sigma}{\sqrt{n}} \quad (\text{A.2})$$

where $z_{c/2}$ is the z -score of the normal distribution with $c\%$ confidence, σ is the standard deviation of the measurements, and n is the number of data points. A confidence interval of 95% is used throughout this study, as it is almost a universal convention. The standard deviation (σ) is calculated from:

$$\sigma = \sqrt{\frac{\sum_{i=1}^n (x_i - \bar{x})^2}{n - 1}} \quad (\text{A.3})$$

where x_i is the result of the i th measurement, and \bar{x} is the arithmetic mean of the n data points considered.

A.1.2 Bias Uncertainty (B_x)

Bias uncertainty will continually add error to the measurements, and due to being systematic, it is impossible to be determined by doing multiple repetitions. As a result, it is commonly estimated by using the accuracy found in the manufacturer's specification or the accuracy obtained by the instrument's calibration. Regardless of the estimation source, the estimated bias uncertainty must have the same confidence interval as the precision uncertainty, which is mostly unattainable.

A.1.3 Uncertainty Propagation

Once the total uncertainty for individually measured quantities is known using the mentioned methods, the uncertainty in the parameters, which are a function of those measured quantities, can be calculated by considering the propagation of uncertainty. In other words, the uncertainty in that parameter is estimated from the known uncertainties in other quantities. If parameter y is a function of m measured quantities, namely, x_1, x_2, \dots, x_m , *i.e.* $y = y(x_1, x_2, \dots, x_m)$, the derivative of the function based on the chain rule is:

$$dy = \frac{\partial y}{\partial x_1} dx_1 + \frac{\partial y}{\partial x_2} dx_2 + \dots + \frac{\partial y}{\partial x_m} dx_m \quad (\text{A.4})$$

where $\partial y / \partial x_i$ is partial derivative of the functional form of parameter y with respect to the i th variable (x_i). By substituting the variation in y (dy) and variation in x_i (dx_i) with Δy and Δx_i , associated with uncertainty in y and x_i , respectively, Equation A.4 gets the following form:

$$\Delta y = \frac{\partial y}{\partial x_1} \Delta x_1 + \frac{\partial y}{\partial x_2} \Delta x_2 + \dots + \frac{\partial y}{\partial x_m} \Delta x_m \quad (\text{A.5})$$

By squaring both sides and neglecting the higher order term, in case that the measured

quantities (x_i) are statistically independent of each other, Equation A.5 becomes:

$$\Delta y^2 = \sum_{i=1}^m \left(\frac{\partial y}{\partial x_m} \Delta x_m \right)^2 \quad (\text{A.6})$$

$$\Delta y = \sqrt{\sum_{i=1}^m \left(\frac{\partial y}{\partial x_m} \Delta x_m \right)^2} \quad (\text{A.7})$$

In case that the functional form of parameter y in terms of the independent variables (x_i) is purely multiplicative, *i.e.*, $y = cx_1^{\alpha_1} x_2^{\alpha_2} \dots x_m^{\alpha_m}$, where c and α_i are arbitrary constants, the relative uncertainty ($\Delta y/y$) can be calculated in a more straightforward way by following four steps: take natural logarithm (\ln) of the function, differentiate, replace differentials as uncertainties, then square each term to get:

$$\left(\frac{\Delta y}{y} \right)^2 = \alpha_1^2 \left(\frac{\Delta x_1}{x_1} \right)^2 + \alpha_2^2 \left(\frac{\Delta x_2}{x_2} \right)^2 + \dots + \alpha_m^2 \left(\frac{\Delta x_m}{x_m} \right)^2 \quad (\text{A.8})$$

$$\left| \frac{\Delta y}{y} \right| = \sqrt{\alpha_1^2 \left(\frac{\Delta x_1}{x_1} \right)^2 + \alpha_2^2 \left(\frac{\Delta x_2}{x_2} \right)^2 + \dots + \alpha_m^2 \left(\frac{\Delta x_m}{x_m} \right)^2} \quad (\text{A.9})$$

$$\left| \frac{\Delta y}{y} \right| = \sqrt{\sum_{i=1}^m \left(\alpha_m \frac{\Delta x_m}{x_m} \right)^2} \quad (\text{A.10})$$

which shows that the square of relative uncertainty in each variable is weighted by the square of its exponent. By implementing the mentioned method for the dependent variables such as carbon conversion efficiency (CCE) and emission index (EI), their uncertainties can be calculated, the derivation of the latter one is explained in the following Section.

A.2 Uncertainty Analysis (Emission Index)

Based on Equation 1.1, emission index of gaseous or particulate species (*i.e.*, CO, CO₂, Unburned HC, NO_x, and BC) was calculated in this study. The mass production rate of the gaseous species was:

$$\dot{m}_{j,\text{produced}} = M_j \left((X_{j,\text{plume}} - X_{j,\infty}) \dot{n}_{\text{plume}} - (X_{j,\text{F}} \dot{n}_{\text{F}})_{\text{inert}} + X_{j,\infty} \dot{n}_{\text{F}} \frac{M_{\text{F}}}{M_{\infty}} \right), \quad (\text{A.11})$$

where M_j , M_{F} , and M_{∞} are molecular mass of species j , fuel gas, and ambient air, respectively. X_j and \dot{n} are mole fraction of species j , and the molar flow rate, respectively. By substituting Equation A.11 into Equation 1.1, the uncertainty of emission index of gaseous species (ΔEI_j) was calculated as follows by using propagation of uncertainties for all measured quantities, assuming that these quantities were independent of one another:

$$\begin{aligned} (\Delta \text{EI}_j)^2 = & \left(\frac{\partial \text{EI}_j}{\partial X_{j,\text{plume}}} \Delta X_{j,\text{plume}} \right)^2 + \left(\frac{\partial \text{EI}_j}{\partial X_{j,\infty}} \Delta X_{j,\infty} \right)^2 + \left(\frac{\partial \text{EI}_j}{\partial \dot{n}_{\text{F}}} \Delta \dot{n}_{\text{F}} \right)^2 + \\ & \left(\frac{\partial \text{EI}_j}{\partial \dot{n}_{\text{plume}}} \right)^2 \left[\sum_k \left(\frac{\partial \dot{n}_{\text{plume}}}{\partial X_{k,\infty}} \Delta X_{k,\infty} \right)^2 + \sum_k \left(\frac{\partial \dot{n}_{\text{plume}}}{\partial X_{k,\text{plume}}} \Delta X_{k,\text{plume}} \right)^2 + \left(\frac{\partial \dot{n}_{\text{plume}}}{\partial \dot{n}_{\text{F}}} \Delta \dot{n}_{\text{F}} \right)^2 \right] \end{aligned} \quad (\text{A.12})$$

Considering the fact that BC concentration was negligible in the ambient, and PAX measured mass fraction of BC (Y_{measured}) at its cell temperature (T_{cell}), the mass production rate of the particulate species (BC), corrected for the temperature, was:

$$\dot{m}_{\text{BC,produced}} = Y_{\text{measured}} \frac{R_{\text{u}} T_{\text{cell}}}{p_{\text{plume}}} \dot{n}_{\text{plume}}. \quad (\text{A.13})$$

where R_{u} is the universal gas constant, and p_{plume} is the static pressure in the duct

recorded by a pressure transducer. Therefore, the uncertainty of emission index of BC (ΔEI_{BC}) was calculated as follows:

$$\begin{aligned}
 (\Delta EI_{BC})^2 = & \left(\frac{\partial EI_{BC}}{\partial Y_{\text{measured}}} \Delta Y_{\text{measured}} \right)^2 + \left(\frac{\partial EI_{BC}}{\partial T_{\text{cell}}} \Delta T_{\text{cell}} \right)^2 + \left(\frac{\partial EI_{BC}}{\partial p_{\text{plume}}} \Delta p_{\text{plume}} \right)^2 + \\
 & \left(\frac{\partial EI_{BC}}{\partial \dot{n}_{\text{plume}}} \right)^2 \left[\sum_k \left(\frac{\partial \dot{n}_{\text{plume}}}{\partial X_{k,\infty}} \Delta X_{k,\infty} \right)^2 + \sum_k \left(\frac{\partial \dot{n}_{\text{plume}}}{\partial X_{k,\text{plume}}} \Delta X_{k,\text{plume}} \right)^2 + \left(\frac{\partial \dot{n}_{\text{plume}}}{\partial \dot{n}_F} \Delta \dot{n}_F \right)^2 \right]
 \end{aligned}
 \tag{A.14}$$

APPENDIX B

Steam Supply System

B.1 Steam Generator

For the experiments discussed in Chapter 2 and 3, steam was supplied by an 18-kW electric steam generator (Sussman, MBA18) with a maximum steam supply of 408 g/min, which is shown in Fig. B.1. To control the total flow rate of steam, the steam generator's outlet was directly attached to a manually adjustable pressure reg-

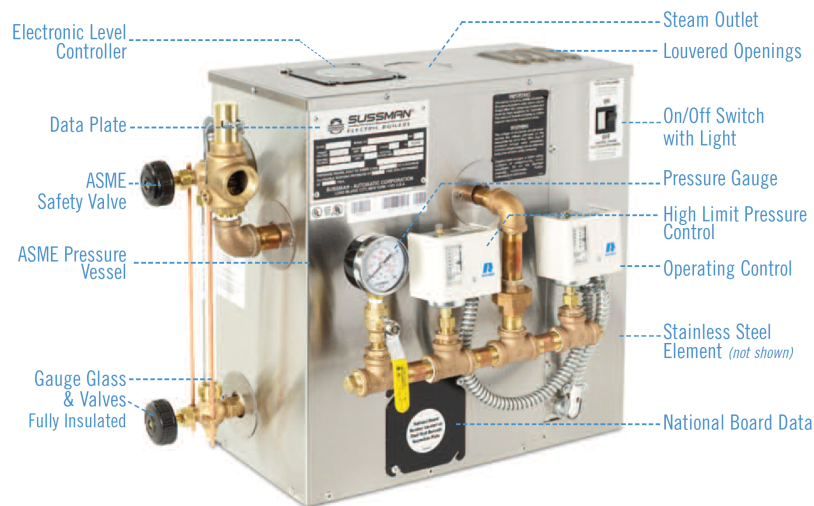


Figure B.1: Electric steam generator and its components (Sussman, 2017)

ulator. The flow was measured by a calibrated cone flow meter (Cameron NUFLO cone Series 3000), designed specifically to measure steam flow rates, which consists of a pipe with an interior cone obstructing the flow of steam and creating a differential pressure across the high- and low-pressure ports. The flow meter was coupled with a differential pressure transmitter (ABB, 2600 T) with a full scale of 16 kPa. Additionally, an absolute pressure transducer (Omega, PX409-100AI) with a full scale of 689 kPa was attached to the flow meter's high-pressure port. The temperature of the steam entering the flow meter was determined by a resistance temperature detector (RTD) probe (Spirax Sarco, EL2270) with a full scale of 500 °C.

The steam temperature, absolute pressure, and differential pressure measurements were recorded by the data acquisition modules (National Instruments, NI-9216 and NI-9203), and steam mass flow rate was calculated using LabVIEW virtual instrument (VI) file. The equation to calculate the steam flow rate and further information are outlined in the study by Ahsan et al. (2019). For a range of 20–200 g/min, the cone flow meter was calibrated. The higher limit was found to be sufficient for this study, whereas the lower limit was connected to the instability and unsteady effects at low flow rates. That being said, this steam generator and flow meter do not have large dynamic ranges for steady and low uncertainty operation; as a result, two flow systems were used, depending on whether the flow rates were high or low.

B.2 High Flow Rates to Burner

A further series of experiments using a heat exchanger for condensing and measuring the steam condensate were carried out to calibrate the cone flow metre, which produced a calibration range of 20–100 g/min and validated the calculated steam mass flow rates. A piping and instrumentation diagram (P&ID) of the setup to deliver high flow rates of steam is schematically shown in Fig. B.2.

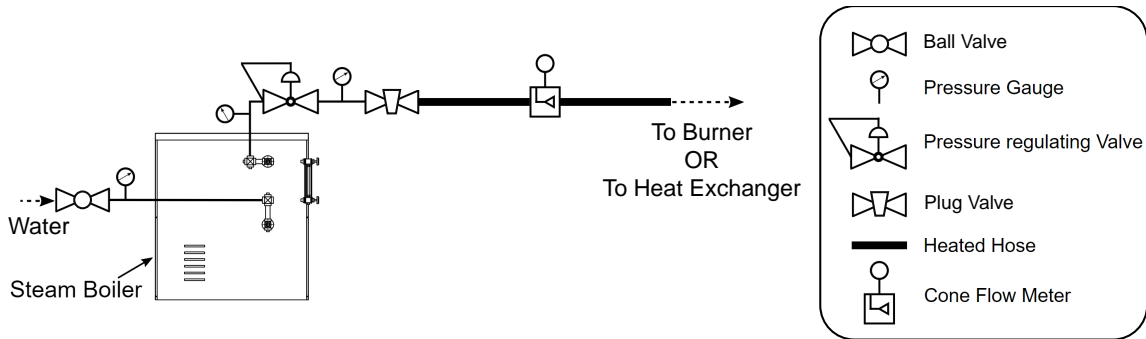


Figure B.2: P&ID of the system supplying high flow rates of steam

B.3 Low Flow Rates to Burner

To supply low flow rates of steam, the steam line was divided into two lines by a tee, as depicted in Fig. B.3. One line had a plug valve and a precision valve to control the low flow rates of steam to the burner through a 6-m heated hose (Dekoron Unitherm, Series 200) with a temperature set point of 150 °C. The other line carried the excess steam through an identical heated hose with a temperature set point of 115 °C and was directed to a heat exchanger to condense the steam; where that water flow rate was measured with the electronic balance and a stopwatch. The steam flow rate to the burner was determined to be the difference between the total flow rate out of the electric steam generator (measured by the cone flow meter) and the measured flow rates of the excess steam line (measured by the electronic balance). The flow rate

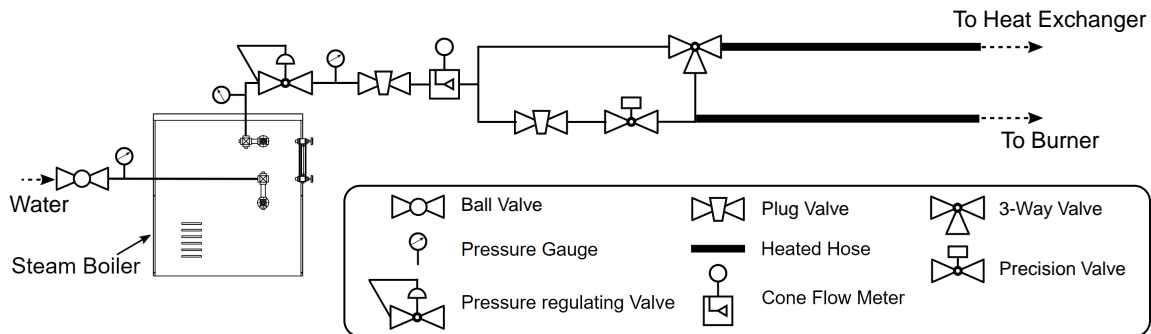


Figure B.3: P&ID of the system supplying low flow rates of steam

of steam used in this study varied from 3.5 to 32 g/min. Due to the limited range of the precision valve, for the flow rates below 20 g/min, the total flow rate was set at 100 g/min, and for the flow rates between 20 to 35 g/min, the total flow rate was set at 200 g/min. The steam supply system was able to bypass the precision valve to calibrate the total flow rate out of the electric steam generator. The steam flow rate uncertainty was less than 10 % of the reading.

APPENDIX C

Particle Image Velocimetry in Combustion Systems

Particle Image Velocimetry (PIV) has been established as a standard measurement tool in the 2C-2D approaches, also used in this study. PIV effectively identifies flow structures in the measurement plane and estimates local gas velocity through correlating particle displacement over a predetermined time interval. Although there are always challenges in capturing and converting images into velocity fields for non-combusting systems, there are some special considerations for reacting flows, especially close to flames. The implications of particle image velocimetry (PIV) in reacting flows are as follows:

- A significant increase in fluid temperature results from heat release due to combustion. For the combustion of hydrocarbons, the highest temperature can exceed 2000 K and is attained at the reaction front (Turns et al., 2000).
- Flame radiation takes place due to the high temperature, and a wide range of wavelengths of light are emitted, particularly soot radiation in diffusion

flames (Chomiak, 1990). Since soot has similar radiative characteristics to a black body, the flame appears yellow and the light it emits can be quite intense.

- Temperature, density, and velocity have a high spatial gradient in the vicinity of the flame front, while pressure is considered to be constant in free flames (Turns et al., 2000).
- The refractive index, an optical property of the fluid medium, locally changes because of the spatial variations in the density and composition of the gaseous mixture (Stella et al., 2001).
- In reacting flows with a non-uniform temperature field, small particles (micron-size solid seed particles) suspended in the gas are subjected to thermophoretic forces that drive them to drift away from hot regions of the gas (flame zone) with a velocity proportional to the local temperature gradient (Chelliah et al., 1991; Muntean and Higuera, 2016).

The basic assumption in PIV is that the seeding particles follow the flow. The Stokes number, characterized as the ratio of particle relaxation time over characteristic flow time, is a measure of particles' capability to follow the flow. According to the literature (Tropea et al., 2007), the particle response time is found to be sufficient for Stokes numbers less than 0.1, which was much less than this for the PIV tests in this study.

Despite the limitations of PIV in laminar and turbulent reacting flows in the past, PIV first proved to be a successful measurement tool in diffusion flames in the study conducted by Driscoll et al. (1994). 2D-PIV is capable of quantifying the structures in the flow through measurements of planar velocity fields and also provides some information about the flame topology by observing the seeding density distribution (Stella et al., 2001). These features allow researchers to study the interaction between flow

and combustion.

Solid refractory particles, such as titanium dioxide (TiO_2), which was first used in diffusion flames by Lewis et al. (1987), are commonly used because of their high melting temperature ($\approx 2120 \text{ K}$) and less tendency to agglomerate.

Oil droplets can also be used to seed the reacting flows with the aim to mark a specific isotherm in proximity of the flame showing the evaporation temperature of the oil. Canola oil with evaporation temperature of about 600 K was used in this study. Oil seeding (*i.e.*, olive or canola) is commonly employed in PIV studies on different combustion systems (Hargrave et al., 2002; Abbasi-Atibeh and Bergthorson, 2019).

APPENDIX D

Multi-slot Burner Drawings

The technical drawings of the assembled multi-slot burner is illustrated in Fig. D.1. Additionally, its individual parts, which are sandwiched together in make this burner, are shown in the following figures (Fig. D.2 to D.8), from the outermost part to the innermost one, skipping the duplicates. The plates that divide the slots are called the dividers, and the the ones that make the space within the slots are called the spacers.

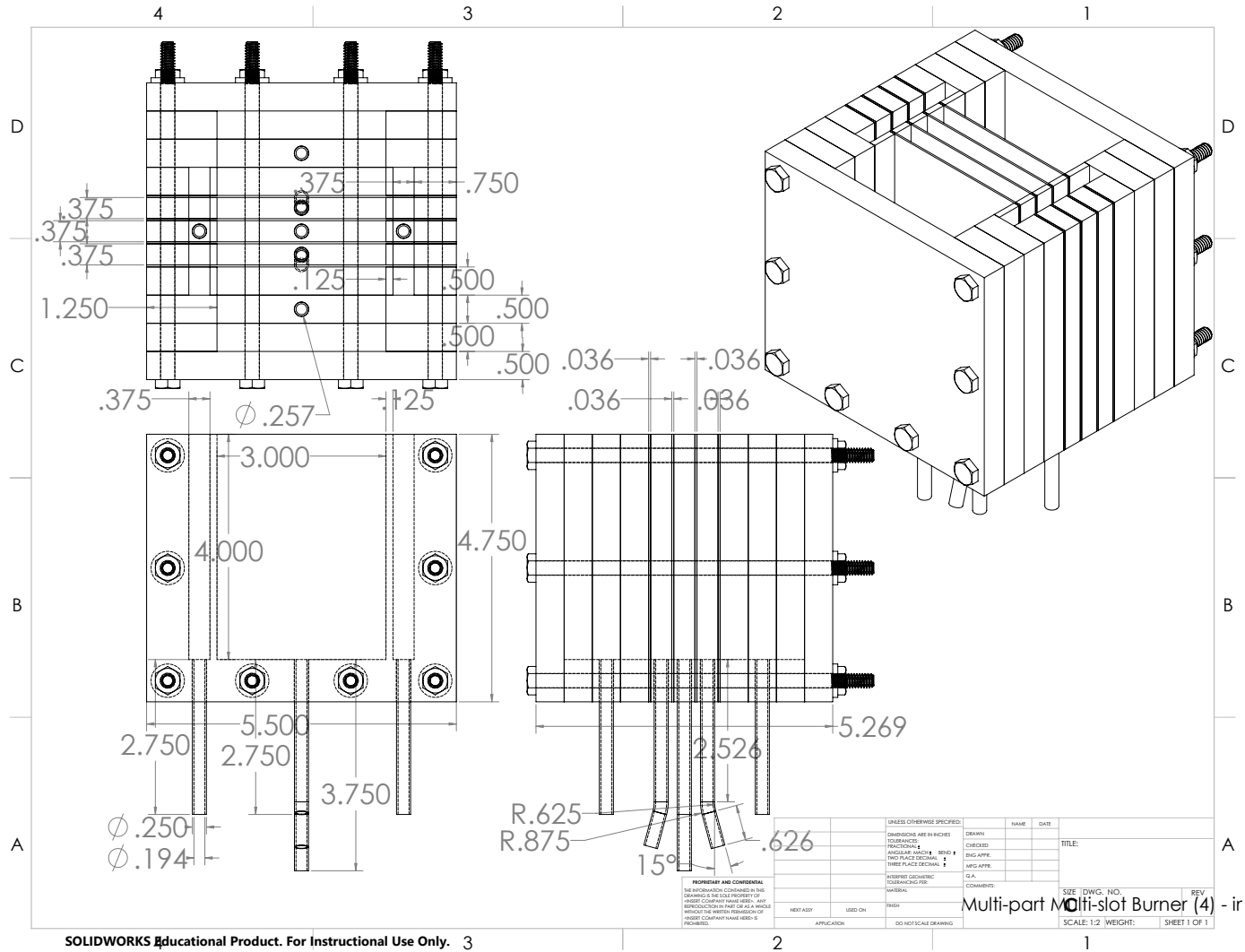


Figure D.1: Assembled multi-slot burner with detailed dimensions (in inches).

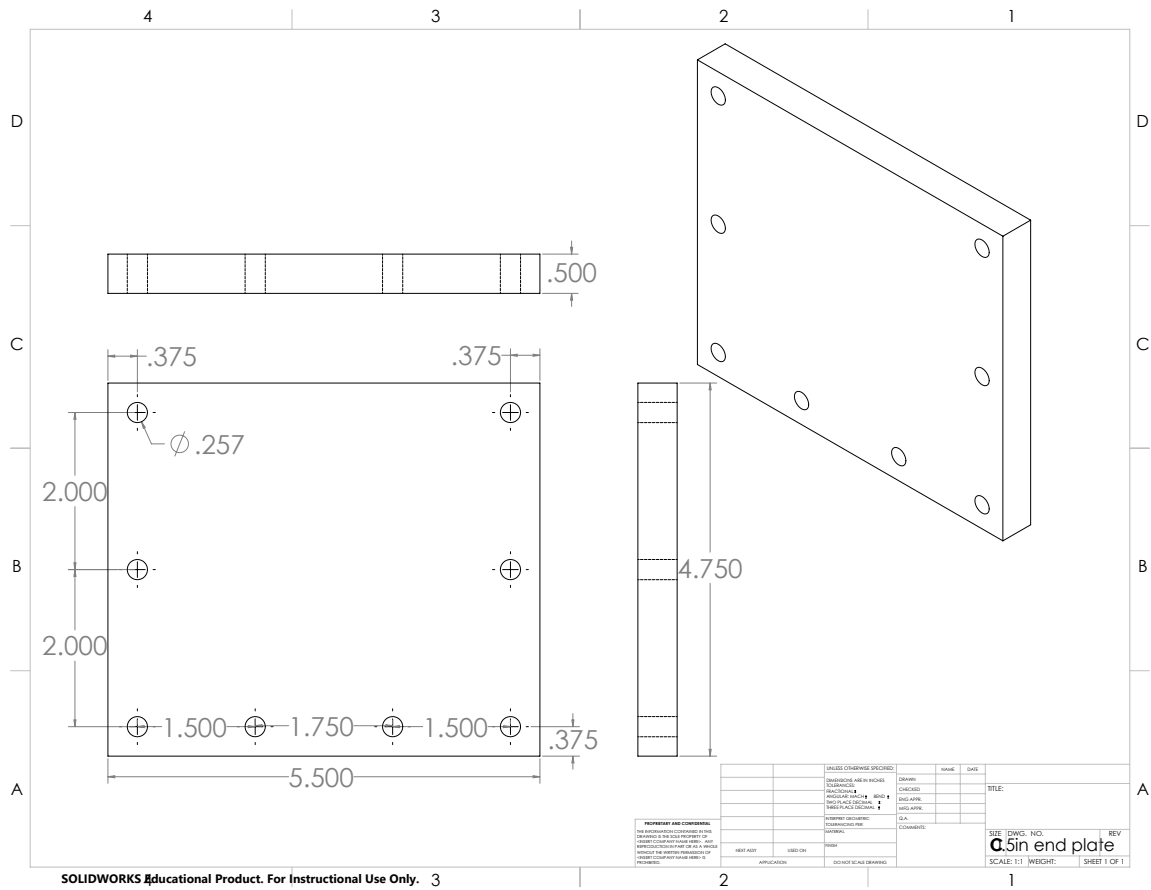


Figure D.2: End plates (dimensions in inches).

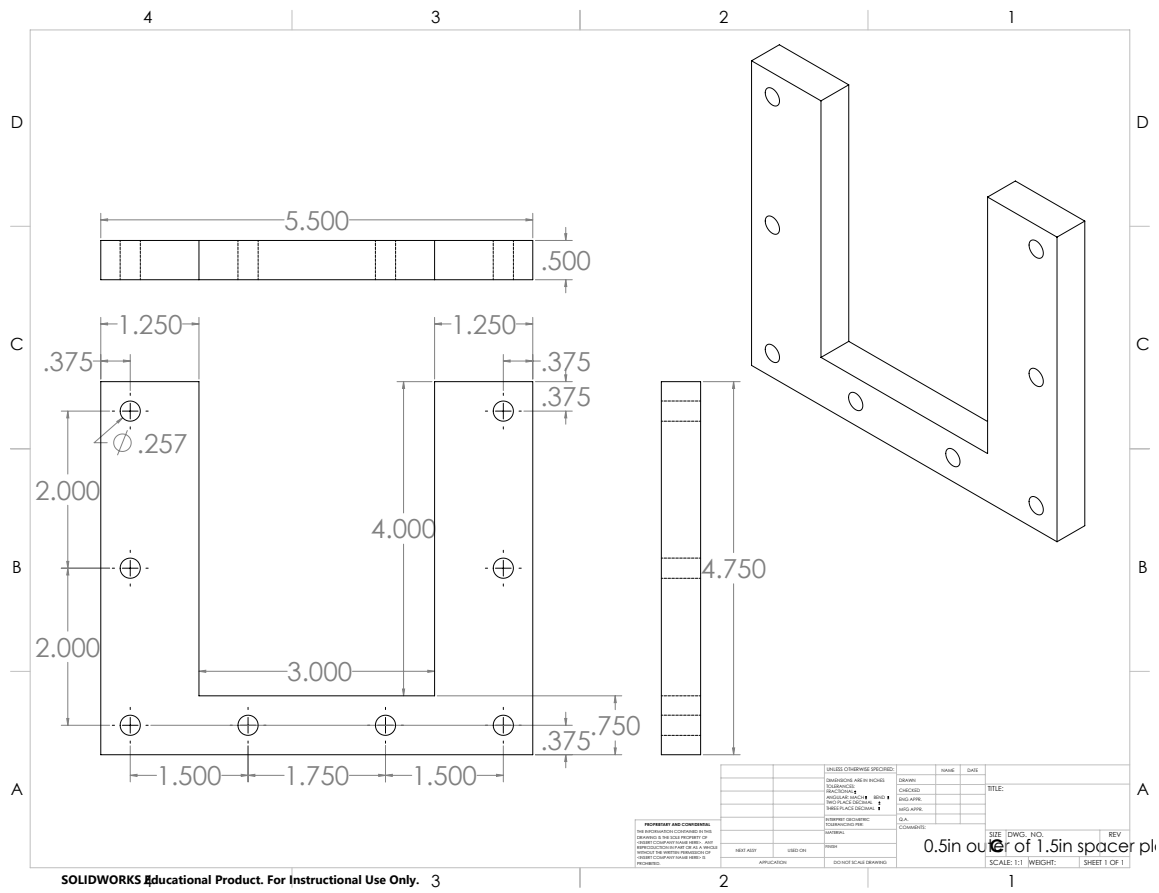


Figure D.3: Outer part of the 1.5-in spacer (dimensions in inches).

